Rational Design of Cu-based Nanocatalysts for the Production of Methanol

A Dissertation Presented

by

Yixiong Yang

to

The Graduate School

in Partial Fulfillment of the

Requirements

for the Degree of

Doctor of Philosophy

in

Chemistry

Stony Brook University

August 2013

Stony Brook University

The Graduate School

Yixiong Yang

We, the dissertation committee for the above candidate for the

Doctor of Philosophy degree, hereby recommend

acceptance of this dissertation.

Michael G. White-Ph. D., Dissertation Advisor
Professor, Department of Chemistry

Jose Rodriguez-Ph. D., Chairperson of Defense
Senior Chemist, Brookhaven National Laboratory

Philip M. Johnson-Ph. D., Third Member
Professor, Department of Chemistry

Ping Liu-Ph. D., Additional Inside Member
Chemist, Brookhaven National Laboratory

Yan Li- Ph. D., Outside Member
Assistant Computational Scientist, Brookhaven National Laboratory

This dissertation is accepted by the Graduate School

Charles Taber
Interim Dean of the Graduate School

Abstract of the Dissertation

Rational Design of Novel Catalysts for the Production of Methanol from CO_2 Hydrogenation

by

Yixiong Yang

Doctor of Philosophy

in

Chemistry

Stony Brook University

2013

The synthesis of methanol (CH_3OH) from CO_2 hydrogenation ($CO_2+3H_2 \rightarrow CH_3OH+H_2O$) has attracted considerable attention recently due to its industrial and environmental significance. It is a promising way to convert CO_2, a greenhouse gas, into a renewable liquid fuel, CH_3OH. Commercially, the reaction is conducted over a Cu-ZnO/Al_2O_3 catalyst under high temperature (220-240°C) and high pressure (50-100 bar) conditions, but the conversion is limited to ~20%. In this work, a combined theoretical and experimental study was carried out in order to derive general principles to improve the performance of Cu-based catalysts.

Density Functional Theory (DFT) calculations were carried out to elucidate the reaction mechanism of CO_2 hydrogenation on the Cu(111) surface and an unsupported Cu nanoparticle (NP). The dominant reaction pathway and key intermediates were identified. The effect of Cu NP size on the catalytic activity was revealed.

The promotion effect by a second metal dopant towards the activity of Cu-based catalysts was also investigated. A NiCu catalyst was found to be the most promising one after screening of a series of bimetallic systems. Two descriptors were proposed to predict the catalytic activity by DFT-based Kinetic Monte Carlo (KMC) simulations.

Inverse catalysts were used as model systems to study the role of the metal oxide supports towards the activity of the catalysts. Metal oxides were deposited on Cu(111) to model the oxide-Cu interface. Both small metal oxide clusters and metaloxide chain structures were included to elucidate the size effect of the metal oxide towards the promotion of methanol synthesis reaction. Ti_3O_6/Cu(111) shows the best activity since it can promote methanol production from two different pathways.

The electronic interaction between the metal-oxide and Cu(111) was also probed experimentally using Two-photon photoemission spectroscopy (2PPE). Inverse catalysts were prepared by depositing size-selected metal oxide nanoclusters on Cu(111). The charge transfer direction and magnitude between the metal oxide clusters and Cu(111) was elucidated by a combination of DFT calculations and work function measurement from 2PPE experiments.

Table of Contents

List of Tables

List of Figures

List of Abbreviations

DMFC: Direct Methanol Fuel Cell

DFT: Density Functional Theory

KMC: Kinetic Monte Carlo

2PPE: Two-photon Photoemission

TS: Transition State

HF: Hartree-Fock

CI: Configuration Interaction

XC: Exchange Correlation

LDA: Local Density Approximation

GGA: Generalized Gradient Approximation

ECP: Effective Core Potential

PP: Pseudopotential

LST: Linear Synchronous Transit

QST: Quadratic Synchronous Transit

CG: Conjugated Gradient

UHV: Ultrahigh Vacuum

RF: Radio Frequency

DC: Direct Current

TPD: Temperature Programmed Desorption

AES: Auger Electron Spectroscopy

XPS: X-ray Photoemission Spectroscopy

CW: Continuous Wave

SHG: Second Harmonic Generation

THG: Third Harmonic Generation

BBO: Beta Barium Borate

IS: Image State

SS: Surface State

DOS: Density of State

Acknowledgement

I would like to take the chance to show my great appreciation toward all of the people who helped me throughout my graduate study. First and foremost, I would like to thank my advisors, Prof. Michael White and Dr. Ping Liu, for their guidance and advice. I have always been inspired and motivated by their enthusiasm and dedication to research. Their great patience and faith in me despite all the mistakes I have made in the past six years are greatly appreciated. I also thank my committee members, Prof. Philip Johnson and Dr. Jose Rodriguez for all the help and inspiring discussions.

In addition, I am grateful to my colleagues and groups members for their help and support. I enjoyed all the useful discussions with Dr. Yongman Choi about DFT calculations at the very beginning of my graduate study. I would also like to thank Dr. Jing Zhou and Dr. Jia Zhou, especially. They were not only great mentors in the lab, but also close friends of mine after work. Their intelligence and dedication to work serve as a great model for me. I enjoyed the time with the other members in the group too and would like to thank them for being there whenever I needed a hand in the lab.

Last but not least, I would like to thank my parents for their understanding and support. I would not be here without their encouragement and love.

Chapter 1. Introduction

Methanol (CH_3OH) synthesis from CO_2 hydrogenation ($CO_2 + 3H_2 \rightarrow CH_3OH + H_2O$) has attracted a significant amount of interest in the past few decades[1-3]. This reaction is of great industrial significance because methanol can be used as the raw material for other synthetic hydrocarbons. More importantly, methanol provides an efficient way to store energy and can be used as a convenient liquid fuel in an internal combustion engine or direct methanol fuel cell (DMFC)[4]. The CO_2 generated from the use of CH_3OH as a liquid fuel can be chemically recycled by converting it to CH_3OH through the hydrogenation reaction, which is considered as a promising way to reduce CO_2 emissions[5].

Commercially, methanol is synthesized from syngas (CO-CO_2-H_2) over a Cu-ZnO/Al_2O_3 catalyst at 493-573K and 5-10MPa[6]. It has been shown that CO_2 is the predominant carbon source for methanol under industrial conditions by means of isotope labeling experiments[7]. Even though the reaction is exothermic[2], the conversion of CO_2 to methanol is kinetically limited to 15-25%. Therefore, a catalyst with better performance is highly desired to improve the efficiency of the reaction.

Rational design of a novel catalyst cannot be realized without a comprehensive understanding of detailed reaction mechanisms. Recent advances in both theoretical methods and experimental techniques have made it possible. In this dissertation, an atomic-level understanding of the reaction mechanism was achieved by a combination of Density Functional Theory (DFT)-based calculations and experimental surface science investigations.

The industrial catalysts for methanol production from CO_2 hydrogenation consist of Cu particles dispersed on oxide supports. Previous experimental results showed that catalyst performance greatly depends on the size of the Cu particles[8]. Cu nanoparticles exhibited higher activity compared with bulk Cu. In Chapter 3 of this dissertation, DFT calculations were employed to elucidate the size effect in the catalyst performance. A pyramidal structure consisting of 29 Cu atoms (Cu_{29}) was used to model the Cu nanoparticles. For comparison, extended Cu(111) was also studied because it is the most exposed facet in bulk Cu materials. Key reaction intermediates and reaction pathways on Cu were identified. The superior activity of Cu nanoparticles were understood by comparing the reaction energetics along the pathway on Cu_{29} and Cu(111).

Following a detailed description of reaction mechanisms on pure Cu catalysts, Chapter 4 of this dissertation focused on the effect of metal dopants on the catalyst activity. A screening of a series Cu-based alloy catalysts was conducted by DFT calculations and Kinetic Monte Carlo (KMC) simulations. The effect of a secondary metal dopant to the reaction energetics and dominating pathway on Cu-based catalysts was elucidated. Two possible descriptors, which can be used to predict the Cu-based catalysts towards methanol production reaction, were also proposed.

The interaction between the metal-oxide support and Cu is believed to play an important role determining the catalyst activity. Chapter 5 of this dissertation elucidates the detailed reaction energetics at the interface of metal-oxide and Cu(111) surface by employing an inverse catalyst as a model system. Small metal oxide clusters (Ti_3O_6, Zn_3O_3 and Mo_3O_9) were used to simulate the relatively small oxide nanoparticles. For comparison, metal oxide chain structures (TiO_2, ZnO and MoO_3) were also employed to simulate the interface between Cu and relatively big oxide nanoparticles with bulk-like structures.

In order to further understand the electronic interactions between the metal-oxide and Cu(111), a combination of two-photon photoemission (2PPE) and DFT investigation was conducted and is reported in Chapter 6 of this dissertation. A size-selected cluster beam deposition apparatus was employed to deposit small metal-oxide clusters (Mo_3O_9, W_3O_9, Ti_3O_6, Mo_3O_6, W_3O_6, Ti_5O_{10}) on Cu(111). The surface dipole moment resulted from the deposition of clusters was probed by work function measurement using 2PPE. The measured overall dipole moment was resolved into two components, i.e, the dipole associated with the cluster itself and a dipole induced by the charge transfer between the cluster and the Cu(111) surface. With the aid of DFT calculations, the dipole contribution from charge transfer can then be easily determined.

Chapter 2. Computational and experimental methods

2.1. Computational method

2.1.1. Density Functional Theory

First principles calculations based on DFT have been playing an increasingly important role in the field of surface science and heterogeneous catalysis due to the continuing improvements in computing capabilities and electronic structure calculation algorithms. Results from DFT calculations can provide great insights into reaction mechanism, some of which are difficult to obtain by experimental techniques. DFT can determine the geometries and electronic structures of the intermediates and transition states (TS) involved in the reaction. Detailed description of reaction mechanisms is possible by calculating energetics for elementary steps.

The fundamental equation upon which electronic structure theories are based is the time-independent Schrödinger equation,

$$\hat{H}\psi(\vec{x}_1, \vec{x}_2, \dots \vec{x}_N, \vec{R}_1, \vec{R}_2, \dots \vec{R}_M) = E\psi(\vec{x}_1, \vec{x}_2, \dots \vec{x}_N, \vec{R}_1, \vec{R}_2, \dots \vec{R}_M) \qquad (2.1)$$

where $\hat{H}$ is the Hamiltonian for a system consisting of N electrons and M nuclei, E is the total energy of the system and ψ is the wave function. Solution of this equation would yield fundamental information about the system. $\hat{H}$ is consisted of five terms, as

$$\hat{H} = \hat{T}_e + \hat{T}_N + \hat{V}_{NN} + \hat{V}_{Ne} + \hat{V}_{ee} \qquad (2.2)$$

where the first two terms describe the kinetic energy of electrons and nuclei and the other three terms describe the potential due to the nuclei-nuclei, nuclei-electron and electron-electron electrostatic interactions. The Schrödinger equation can be further simplified using the Born-Oppenheimer approximation, which assumes the electrons move in the field of fixed nuclei because of the significant differences between the masses of nuclei and electrons. As a result, the kinetic energy of nuclei is zero and the potential due to the nuclei-nuclei interaction is a constant and can be calculated by:

$$E_{nuc} = \sum_{A=1}^{M} \sum_{B>A}^{M} \frac{Z_A Z_B}{r_{AB}}\ , \tag{2.3}$$

where A and B run over the M nuclei, Z_A and Z_B are the charges of the nuclei and r^{AB} is the distance between nuclei A and B. The problem now is to calculate E_{elec} if total energy E is defined as:

$$E_{total} = E_{elec} + E_{nuc}\ , \tag{2.4}$$

where E_{elec} is defined as:

$$\hat{H}_{elec} \psi_{elec} = E_{elec} \psi_{elec}\ . \tag{2.5}$$

Eq.(2.5) is the so-called electronic Schrödinger equation, ψ_{elec} is the electronic wave function and $\hat{H}_{elec}$ is electronic Hamiltonian defined as:

$$\hat{H}_{elec} = \hat{T}_e + \hat{V}_{Ne} + \hat{V}_{ee} = -\frac{1}{2} \sum_{i=1}^{N} \nabla_i^2 - \sum_{i=1}^{N} \sum_{A=1}^{M} \frac{Z_A}{r_{iA}} + \sum_{i=1}^{N} \sum_{j>i}^{N} \frac{1}{r_{ij}}\ . \tag{2.6}$$

From this point, only the electronic Schrödinger equation is considered and the subscript ‘elec’ will be neglected. Ψ is a N-electron wave function and if ψ is known, Ecan be calculated by:

$$E = \frac{\langle \psi | \hat{H} | \psi \rangle}{\langle \psi | \psi \rangle} \tag{2.7}$$

Unfortunately, ψ is unknown and the electronic Schrödinger equation is analytically insolvable for the complex many-atom, many-electron system, which happen to be the interest of chemists and physicists. Various computational schemes, e.g., Hartree-Fock (HF), perturbation theory, configuration interaction (CI), etc. are available to construct an approximation to ψ but these methods are usually computational expensive in order to get a good approximation. As a result, their applications in surface chemistry and heterogeneous catalysis are limited.

A breakthrough was realized by the introduction of DFT, which lowered the computational burden significantly. In the scheme of DFT, electron density $\rho(\vec{r})$ is the basic quantity and defined as the probability of finding any of the N electrons within the volume element $d\vec{r}$ while the other N-1 electrons have arbitrary positions. The first Hohenberg-Kohn theorem demonstrates that the $\rho(\vec{r})$ uniquely determines the $\widehat{H}$ and thus the energy of the system E. The total energy is a functional of electron density. The total energy is further divided into three terms as:

$$E[\rho(\vec{r})] = T[\rho(\vec{r})] + E_{ee}[\rho(\vec{r})] + E_{Ne}[\rho(\vec{r})] \tag{2.8}$$

where $T[\rho(\vec{r})]$ is kinetic energy, $E_{ee}[\rho(\vec{r})]$ and $E_{Ne}[\rho(\vec{r})]$ are the potential energy due to the electron-electron interaction and nuclei-electron attraction respectively. The first two terms are system independent and defined as the Hohenberg-Kohn functional:

$$E_{HK}[\rho(\vec{r})] = T[\rho(\vec{r})] + E_{ee}[\rho(\vec{r})]. \tag{2.9}$$

The ground state energy E_0 will be delivered if and only if the input density is the true ground state density ρ_0, as stated in the second Honhenberg-Kohn Theorem:

$$E_0 = \ T[\rho_0] + E_{ee}[\rho_0] + E_{Ne}[\rho_0] \tag{2.10}$$

However, the exact forms of the terms in Eq(2.10) are still unknown. To tackle this problem, Kohn and Sham introduced a fictitious system of non-interacting electrons, with a Hamiltonian with an effective local potential $V_s(\vec{r})$:

$$\widehat{H}_S = -\frac{1}{2}\sum_{i=1}^{N} \nabla_i^2 + \sum_{i=1}^{N} V_s(\vec{r_i}). \tag{2.11}$$

The ground-state electron density of the reference system is the same as the real system of interest where the electrons do interact with each other. The one-electron Kohn-Sham operator is defined as:

$$\hat{f}^{KS} = -\frac{1}{2}\nabla^2 + V_s(\vec{r}) \, , \tag{2.12}$$

Using the spin orbitals φ_i in the reference system, the energy ε_i is:

$$\hat{f}^{KS}\varphi_i = \varepsilon_i\varphi_i \tag{2.13}$$

These orbitals φ_i are so-called Kohn-Sham orbitals. The ground state wave function of the reference system can be represented by a Slater determinant as:

$$\Theta_S = \frac{1}{\sqrt{N!}}\begin{vmatrix} \varphi_1(\vec{x}_1) & \varphi_2(\vec{x}_1) & \cdots & \varphi_N(\vec{x}_1) \\ \varphi_1(\vec{x}_2) & \varphi_2(\vec{x}_2) & \cdots & \varphi_N(\vec{x}_2) \\ \vdots & \vdots & & \vdots \\ \varphi_1(\vec{x}_N) & \varphi_2(\vec{x}_N) & \cdots & \varphi_N(\vec{x}_N) \end{vmatrix} \tag{2.14}$$

The effective potential $V_s(\vec{r})$ is chosen so that the density resulting from the reference system is exactly the ground state density of the real system:

$$\rho_S(\vec{r}) = \sum_{i=1}^{N}|\varphi_i(\vec{r})|^2 = \rho_0(\vec{r}) \tag{2.15}$$

The exact kinetic energy of the reference system can be calculated as:

$$T_s[\rho(\vec{r})] = -\frac{1}{2}\sum_{i=1}^{N}\langle\varphi_i|\nabla^2|\varphi_i\rangle \tag{2.16}$$

$E_{ee}[\rho(\vec{r})]$ is consisted of two component, i.e. the classical Coulomb interaction $J[\rho(\vec{r})]$ and the non-classical portion due to exchange and correlation effects $E_{ncl}[\rho(\vec{r})]$. Only $J[\rho(\vec{r})]$ is known as:

$$J[\rho(\vec{r})] = \frac{1}{2}\int\int\frac{\rho(\vec{r_1})\rho(\vec{r_2})}{r_{12}}d\vec{r_1}d\vec{r_2} \tag{2.17}$$

$E_{Ne}[\rho(\vec{r})]$ can be calculated by:

$$E_{Ne}[\rho(\vec{r})] = \sum_{i=1}^{N}\int\sum_{A=1}^{M}\frac{Z_A}{r_{iA}}|\varphi_i(\vec{r})|^2 d\vec{r_i} \tag{2.18}$$

As a result, the total energy is:

$$E[\rho(\vec{r})] = T_s[\rho(\vec{r})] + J[\rho(\vec{r})] + E_{Ne}[\rho(\vec{r})] + E_{XC}[\rho(\vec{r})], \tag{2.19}$$

where $E_{XC}[\rho(\vec{r})]$ is the only unknown term and is called the exchange-correlation energy. Different approximations are used within the DFT scheme to calculate$E_{XC}[\rho(\vec{r})]$. The difference between various DFT methods is the choice of functional form for the exchange-correlation energy.

2.1.1.1. Functionals for exchange-correlation energy

Different levels of approximations have been developed to calculate E_{XC}. Local Density Approximation (LDA) is the basis of all the other exchange-correlation functionals. In LDA, a system of uniform electron gas was introduced, in which electrons move on a positive background charge distribution so that the total system is still neutral. E_{XC} at any point in space is a function of the electron density at that point:

$$E_{XC}^{LDA} = \int \rho(\vec{r})\, \varepsilon_{XC}(\rho(\vec{r})) d\vec{r} \tag{2.20}$$

where $\varepsilon_{xc}(\rho(\vec{r}))$ is the exchange-correlation energy per particle of a uniform electron gas of density $\rho(\vec{r})$. The probability that there is an electron at this position in space is $\rho(\vec{r})$. ε_{XC}^{LDA} can be further divided into two terms, i.e., the exchange energy ε_x and correlation energyε_c:

$$\varepsilon_{XC}\big(\rho(\vec{r})\big) = \varepsilon_X\big(\rho(\vec{r})\big) + \varepsilon_C(\rho(\vec{r})) \tag{2.21}$$

$\varepsilon_X\big(\rho(\vec{r})\big)$ is defined explicitly as :

$$\varepsilon_X\big(\rho(\vec{r})\big) = -\frac{3}{4}\sqrt[3]{\frac{3\rho(\vec{r})}{\pi}} \tag{2.22}$$

No such expressions are available for $\varepsilon_C(\rho(\vec{r}))$ and the available LDA methods differ only in their representation of $\varepsilon_C\big(\rho(\vec{r})\big)$. Though results from LDA give reasonable structural information, the accuracy in the aspect of energetics is rather poor.

In order to account for the non-homogeneity of the true electron density, the gradient of density $\nabla\rho(\vec{r})$ is considered in the generalized gradient approximation (GGA):

$$E_{XC}^{GGA} = \int f(\rho(\vec{r}), \nabla\rho(\vec{r}))\, d\vec{r} \tag{2.23}$$

The functional has very complicated analytical forms due to complex mathematical constructs. It cannot be understood by simple physically motivated reasoning and therefore will not be discussed here in this thesis. The studies reported in this thesis were conducted using GGA method proposed by Perdew and Wang[9] (PW91).

GGA methods are by far the most popular method used in surface chemistry and catalysis. The accuracy of GGA is superior compared with LDA in most cases. It can provide structural information, energetics and electronic structures for most systems with a good accuracy. However, GGA methods fail to describe the electronic structures of strongly correlated materials such as transition-metal oxide. These materials have localized valence orbitals, e.g., d and f electron systems with narrow bands. GGA methods over delocalize the electrons and fail to account for the strong Coulomb repulsion between electrons in these narrow bands. The DFT+U method was introduced in order to improve the description of such systems. Among different DFT+U methods available, the one introduced by Dudarev[10] was adopted in this thesis.

The electrons are divided into two groups: delocalized electrons and localized electrons. The delocalized electrons are described as in standard GGA methods. For the delocalized electron, the energy is:

$$E^{GGA+U} = E^{GGA} + E^{U} - E^{dc}. \tag{2.24}$$

Coulomb interactions were counted by a term E^{U} as:

$$E^{U} = \frac{1}{2} U \sum_{i,j} n_i n_j, \tag{2.25}$$

where n_i and n_j are orbital occupancy. E^{dc} is the so called double counting term, because the energy contribution already included in the GGA functional has to be removed in order to avoid counting its contribution twice. If the number of delocalized electrons is $N = \sum_i n_i$ then E^{dc} can be approximated as:

$$E^{dc} = \frac{UN(N-1)}{2}. \tag{2.26}$$

As a result, Eq (2.24) can be rewritten as:

$$E^{GGA+U} = E^{GGA} + \frac{1}{2} U \sum_{i,j} n_i n_j + \frac{UN(N-1)}{2}. \tag{2.27}$$

Oribtal energy is the derivative of the total energy with respect to n_i:

$$\epsilon_i^{GGA+U} = \epsilon_i^{GGA} + U(\frac{1}{2} - n_i), \tag{2.28}$$

which means the energy of occupied states are lowed by $\frac{1}{2}U$ and the energy of unoccupied states are increased by $\frac{1}{2}U$. The value of U can be calculated by *ab initio* methods or determined empirically, fitting the calculated electronic structures to experimental observations.

2.1.1.2. Basis set

In DFT, the Kohn-Sham orbitals are represented by a linear combination of a set of basis functions:

$$\varphi_i = \sum_\mu c_{i\mu} \chi_\mu, \tag{2.29}$$

Basis set χ_μ can be a local basis set (atomic orbitals) or a plane-wave basis set. In this thesis, both of these two types of basis sets were employed. The numerical basis set used in this thesis is a kind of local basis set. The basis set, χ_μ, is given numerically as values on an atomic-centered spherical polar mesh, rather than as analytical functions.

In this thesis, most systems of interests are periodic, where the electron density is a periodic function of $\vec{r}$:

$$\rho_{(\vec{r})} = \rho_{(\vec{r}+\vec{R})} \tag{2.30}$$

$\vec{R}$ is any translational vector of the lattice under consideration. According to Bloch's theorem, the orbitals of a periodic system can be written as a product of a plane wave and a lattice-periodic part as:

$$\varphi(\vec{k},\vec{r}) = e^{i\vec{k}\vec{r}} \cdot u(\vec{k},\vec{r}), \tag{2.31}$$

where the wave vector $\vec{k}$ are within the first Brillouin zone and the lattice-periodic part has the same periodicity as φ:

$$u(\vec{k},\vec{r}+\vec{R}) = u(\vec{k},\vec{r}). \tag{2.32}$$

Specifically, $u(\vec{k},\vec{r})$ can be expanded in plane waves whose wave vector, $\vec{G}$, is the reciprocal lattice vector:

$$u(\vec{k},\vec{r}) = \textstyle\sum_G c_{\vec{k},\vec{G}} e^{i\vec{G}\vec{r}}. \tag{2.33}$$

Combining Eq(2.32) and (2.33), Eq(2.31) can be rewritten as:

$$\varphi(\vec{k},\vec{r}) = \textstyle\sum_G c_{\vec{k},\vec{G}} e^{-i(\vec{G}+\vec{k})\vec{r}}. \tag{2.34}$$

In other words, the Kohn-Sham orbitals are a linear combination of a series of plane-wave basis functions. The basis functions can be written as:

$$\chi(\vec{r}) = e^{-i(\vec{G}+\vec{k})\vec{r}}. \tag{2.35}$$

2.1.1.3. Pseudopotentials

Core electrons are usually chemically inert because they are strongly bound to nuclei, spatially compact and do not participate in bonding. Therefore, the explicit treatment of these inert core electrons can be replaced by an effective core potential (ECP) or pseudopotential (PP) in order to reduce the computational cost. PP is a must for calculations using plane-wave basis sets because the orbitals are strong oscillations near the nuclei. A very large number of plane waves are required to describe these oscillations and it is impossible to do so for systems with practical interest.

2.1.1.4. Brillouin zone sampling

For periodic systems, the application of Bloch's theorem (Eq(2.34)) changes the problem of calculating an infinite number of electronic wave functions to one of calculating a finite number of electron wave functions at an infinite number of $\vec{k}$ points. However, it is impractical to calculate every $\vec{k}$ point and integrate over the Brillouin zone. Instead, a weighted summation of special $\vec{k}$ is used to replace the integration over the Brillouin zone. In this thesis, the sampling of $\vec{k}$ points was conducted by using the method proposed by Monkhorst and Pack[11]. In the MP scheme, the $\vec{k}$ points mesh is an equally spaced mesh in the Brillouin zone. If the number of $\vec{k}$ points sampled in a specific direction (x, y or z) is n, only the special $\vec{k}$ points

$$\vec{k} = u_x\vec{b}_x + u_y\vec{b}_y + u_z\vec{b}_z, \qquad (2.36)$$

are considered in the calculation. $\vec{b}_i$ is the reciprocal lattice vector. u_i is defined as:

$$u_i = \frac{2r-n-1}{2n}, \qquad (2.37)$$

where $r = 1, 2, \cdots, n$.

2.1.1.5. Transition state search method

In order to study the reaction kinetics, information about the activation barrier for reactions and the structures of the transition state (TS) is necessary. A TS is at a saddle point on the potential energy surface. It is a minimum in all directions except along the reaction coordinate, in which it is a maximum. Different techniques are available to locate the TS on the potential energy surface. In this thesis, linear synchronous transit (LST) and quadratic synchronous transit (QST) methods are employed. In an LST search, a maximum is located by changing the coordinates linearly between the reactant and product. LST is followed by an energy minimization in directions conjugate to the reaction pathway, which is so called conjugated gradient minimization (CG). Another maximization is conducted after that by using QST, in which the coordinates are assumed to follow a parabola, defined by reactant, product and the point located by CG. A TS is located after repeated cycles of CG and QST.

2.1.2. Kinetic Monte Carlo (KMC) simulations

Great insights into reaction mechanisms can be obtained by DFT calculations, which provide a detailed description of the elementary steps involved in the description. It can elucidate the reaction energetics, the geometries and electronic structures of intermediates and TS. However, in order to understand the surface chemical kinetics, a statistical simulation account for the interplay between all the elementary steps under certain reaction condition is desired. Such a simulation is achieved by the KMC method in this thesis. A typical output of a KMC simulation can provide the surface composition and rate of each elementary step at a certain time under a specific reaction condition. With such information available, the identity of key intermediates and the kinetic-relevant steps can be revealed conveniently.

In a KMC simulation, the system starts with a state i. There are N possible processes or escape pathways for the system to escape from state i. Each of these escape pathways has its own rate constant k_p and the total rate constant (k_{tot}) is defined as:

$$k_{tot} = \sum_{p=1}^{N} k_p. \tag{2.38}$$

The probability of the system has not yet escaped from state i is given by a Poisson distribution as:

$$p_{survival}(\Delta t) = \exp(-k_{tot}\Delta t). \tag{2.39}$$

The probability distribution function for the time of first escape Δt is:

$$p(\Delta t) = \frac{d[1-p_{survival}(\Delta t)]}{d\Delta t} = k_{tot}\exp(-k_{tot}\Delta t). \tag{2.40}$$

Such exponentially distributed escape time is numerically achieved through the expression:

$$\Delta t_{escape} = -\frac{\ln \rho_1}{k_{tot}}, \tag{2.41}$$

where ρ_1 is a random number on the interval $(0, 1]$. The system clock is advanced by Δt_{escape} as:

$$t \to t + \Delta t_{escape}. \tag{2.42}$$

The system is updated by executing process q, which fulfills the condition:

$$\sum_{p=1}^{q} k_p \geq \rho_2 k_{tot} \geq \sum_{p=1}^{q-1} k_p, \tag{2.43}$$

where ρ_2 is a random number on the interval $(0, 1]$. In this way, a process with a larger rate constant has a higher chance of being chosen, as it should. Once the system is in the new state, the list of pathways and rates is updated and the procedure is repeated. For the application of KMC in chemical reactions specifically, the rate constant of each pathway is usually computed by the Arrhenius equation:

$$k = Aexp\left(-\frac{E_a}{k_B T}\right), \tag{2.44}$$

where A is a pre-exponential factor and $E_a$is activation barrier of the reaction, k_B is the Boltzmann constant and T is reaction temperature.

2.2. Experimental setup

2.2.1. Size-selected cluster deposition apparatus

A size-selected cluster deposition apparatus was employed to generate metal-oxide clusters in this thesis. It consists of five sections, i.e, a magnetron sputtering source, a quadrupole ion guide, a quadrupole mass selector, a hexapole ion guide and a Ultrahigh vacuum (UHV) analysis chamber, as shown schematically in Figure 2.1. Because the pressure in the magnetron source is high (~5×10^{-3} Torr) during operation, each section is equipped with a turbomolecular pump to allow for differential pumping to maintain UHV condition (<1×10^{-9} Torr) in the analysis chamber.

The gas-phase clusters are produced by a commercial magnetron sputtering source (Oxford Applied Research NC200U), whose design is based on the concept originally developed by Haberland[12,13]. Metal targets are used and mounted against a magnet. To produce metal-oxide clusters, a gas mixture of ~2% O_2 in Ar is introduced in the source. A glow discharge of Ar is realized after application of a bias voltage (~200V). The ionized Ar^+ ions are confined close to the target by the magnetic field from the magnet. They are accelerated towards the target by applied voltage and begin to sputter the metal targets. The sputtered metal atoms react with O_2 to form metal-oxide clusters. These clusters are usually very energetic and an aggregation gas (He in this study) is introduced to cool the clusters by collisions. As a result, the high kinetic energy is dissipated and the small clusters agglomerate into bigger clusters by colliding with each other. The volume of the aggregation area can be adjusted by a translational stage so that the size-distribution of the generated clusters can be easily controlled.

The clusters are transported downstream by a quadrupole ion guide, which is constructed from four mutually parallel metal rods. Each opposing pair of rods is electrically connected but electrically isolated from the other pair of rods. Two radio frequency (RF) voltages (~600kHz) with the same amplitude but 180˚ out of phase are applied to the two pairs of rods respectively. The RF voltages are provided by a custom built power supply and the amplitude is controlled by an external high voltage power supply (Bertan High Voltage) to maximize the cluster ion intensity going through the ion guide. The survived clusters enter the next chamber, which houses a commercial quadrupole mass filter (Extrel) . The design of the quadrupole mass filter is similar to the quadrupole ion guide. However, a Direct Current (DC) bias (0-10V) is also applied to the rods in addition to the RF voltage. The commercial power supply (Extrel 150-QC; 40 KHz) provides good ion transmission and a unit mass resolution up to 4000 amu. The applied DC bias can be controlled through a Labview program while the ratio between DC and RF voltage is fixed during operation. The program is set up such that the mass filter can run in two modes: mass scan mode generating a mass spectrum of all the cluster species and single mass selection mode only allowing ions with a certain mass to charge ratio to pass.

The selected clusters are extracted into the UHV analysis chamber by a hexapole ion guide. Instead of two pairs of metal rods in quadrupole ion guide, three pairs of rods are used. The RF voltages (~600kHz) are provided by a custom built power supply. A quadrupole bender is attached to hexapole ion guide so that the clusters exiting the hexapole ion guide are deflected by 90˚ before being deposited onto the substrate. The deflection is necessary to prevent contamination from the neutral clusters. Both neutral and ionic clusters are generated from the magnetron source but only the ionic clusters can be selected by the mass selector. A small portion of the neutral clusters can enter the UHV analysis chamber along with the mass-selected ionic clusters. The bender only deflects the ionic clusters on to the substrate and the neutral clusters pass through the bender.

A Faraday cup, a few millimeters away from the exit of the bender is used to detect the cluster intensity. A picoammeter (Keithly) is used to monitor the ion current on the Faraday cup. Figure 2.2 is a typical mass spectrum of $Mo_xO_y^+$ clusters reaching the Faraday cup obtained by using mass scan mode of the quadruopole mass selector. The kinetic energy distribution of a cluster is measured by applying a DC voltage ramp on the Faraday cup while monitoring the cluster ion current. This measurement is necessary to ensure the 'soft-landing' condition, which prevents the deformation of clusters upon deposition[14-17]. The Faraday cup is translated away before deposition. The ion current on the crystal is also measured by the picoammeter. The total number of clusters deposited on the crystal is calculated by the Labview program mentioned above by summing up the current detected by the picoammeter.

2.2.2. UHV analysis chamber

The surface characterization is conducted in a UHV analysis chamber, which is shown schematically in Figure 2.3. The chamber consists of two main levels and is equipped with a XYZ manipulator and rotation stage, which allow for positioning of the crystal within the chamber. The cluster deposition described in the previous section happens at the lower level of the chamber (Figure 2.3(a)), where the quadrupole bender and Faraday cup are mounted. At the same level, there is a quadrupole mass spectrometer (Hiden) to conduct Temperature Programmed Desorption (TPD) to study the binding of adsorbates on the surface.

The rest of the surface characterization happens at the upper level of the chamber (Figure 2.3(b)). This analysis section is equipped with a hemispherical electron energy analyzer (Specs Phoibos 100). During Auger electron spectroscopy (AES) and two photon-photoemission (2PPE) experiments, the crystal is positioned perpendicular to the electron energy analyzer. The incident angle of the electron beam from the electron gun (EQ 22/35, Specs) is 47.5˚ with regard to the surface normal. The beam path of the laser pulse in 2PPE experiments is symmetric to the electron beam path with respect to the analyzer, i.e., the incident angle of the laser pulse is also 47.5˚ with regard to the surface normal during 2PPE measurement. This level also houses an X-ray source (XR-50, Specs), with which X-ray photoelectron spectroscopy (XPS) experiments can be carried out. In this thesis, results from 2PPE and AES measurement will be presented and a brief description of these two techniques will be provided below.

2.2.2.1. Auger Electron Spectroscopy

AES is a spectroscopic technique used to provide qualitative and quantitative analysis of the elemental composition at the surface. In an Auger process, a core-level electron is ejected as a result of high energy electron irradiation. The generated hole is then filled by an electron from a higher energy state, accompanied by an ejection of another electron. The ejected electron is called an Auger electron. The kinetic energy of the Auger electron is independent of the incident electron energy. It is only determined by the energy of the electronic states involved in the Auger process, which are element specific. By detecting the kinetic energy of the Auger electron by an electron energy analyzer, elemental information on the surface is obtained.

2.2.2.2. Two-photon photoemission Spectroscopy

2PPE is a spectroscopic technique for the investigation of interfacial electronic states. It is capable of examining both occupied and unoccupied states by using two photons to remove electrons from the solid. To avoid one-photon photoemission, the energies of the two photons used in 2PPE experiment are lower than the work function of the system of interest. In a 2PPE process, an electron from an initially occupied state is excited into an intermediates state by the first photon $(h\nu_1)$. The second photon$(h\nu_2)$ photoemits the excited electron into vacuum and the kinetic energy of the electron can then be detected experimentally. The measured kinetic energy gives information on the binding energy of the probed electron. Similar as other photoemission spectroscopic techniques, the work function can obtained from the low-energy secondary electron cutoff conveniently in 2PPE experiments. The intermediate state involved in the 2PPE process can be either an unoccupied state (Figure 2.4(a)) or a virtual state (Figure 2.4(b)). The occupancy of the probed state can be easily determined by varying the used photon energy. If the two photon energies are varied by $h\nabla\nu_1$ and $h\nabla\nu_2$ respectively, the measured kinetic energy of the electrons from initially unoccupied states will vary by $h\nabla\nu_2$ .However, the kinetic energy will vary by $h\nabla\nu_1 + h\nabla\nu_2$ from electrons from initially occupied states.

2.2.3. Laser system

The laser system used in the 2PPE experiment will be described in this section. A mode-locked Ti:sapphire oscillator (Spectra-Physics Tsunami) is used to generate the fundamental ultrafast laser pulse. It is pumped by a 5W continuous wave (CW) laser at 532nm from a Nd:YVO_4 gain medium (Spectra-Physics Millennia V). The output laser wavelength is tunable within the range from 720 to 850nm, with a pulse duration of ~100fs. The fundamental laser from the Ti:sapphire system is within the visible and near infrared regions. Higher photon energies can be achieved after second harmonic generation (SHG) and third harmonic generation (THG) processes. . In a SHG process, two photons from fundamental light (ω) go through a beta barium borate (BBO) crystal and one photon with a doubled frequency (2ω) is generated as a result. In a THG process, a photon from the fundamental (ω) and a photon from the SHG process (2ω) are used to interact with another BBO crystal and the frequency of the resulted photon will be tripled (3ω). In our experiment, a time-plate harmonic generator (Photop TP-2000B) is used to accomplish such conversions.

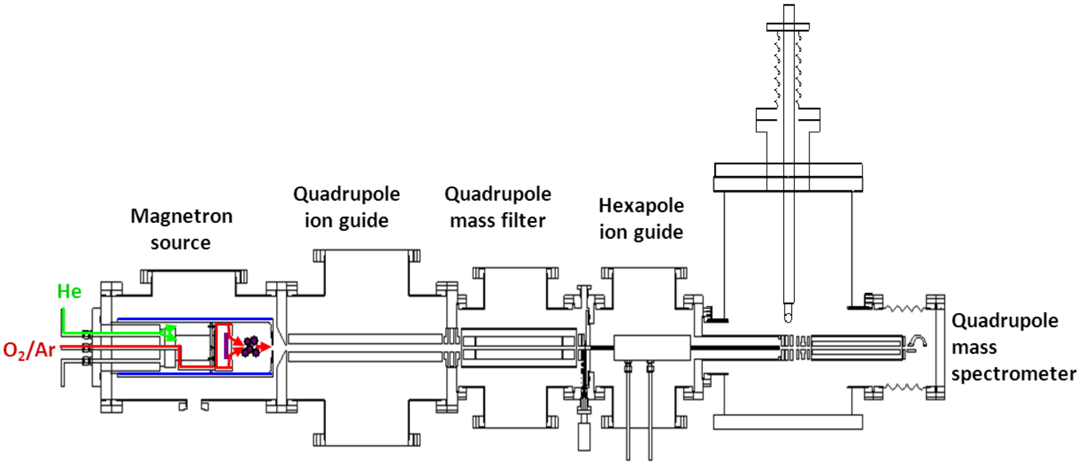

Figure 2.1. Schematic of size-selected cluster deposition apparatus.

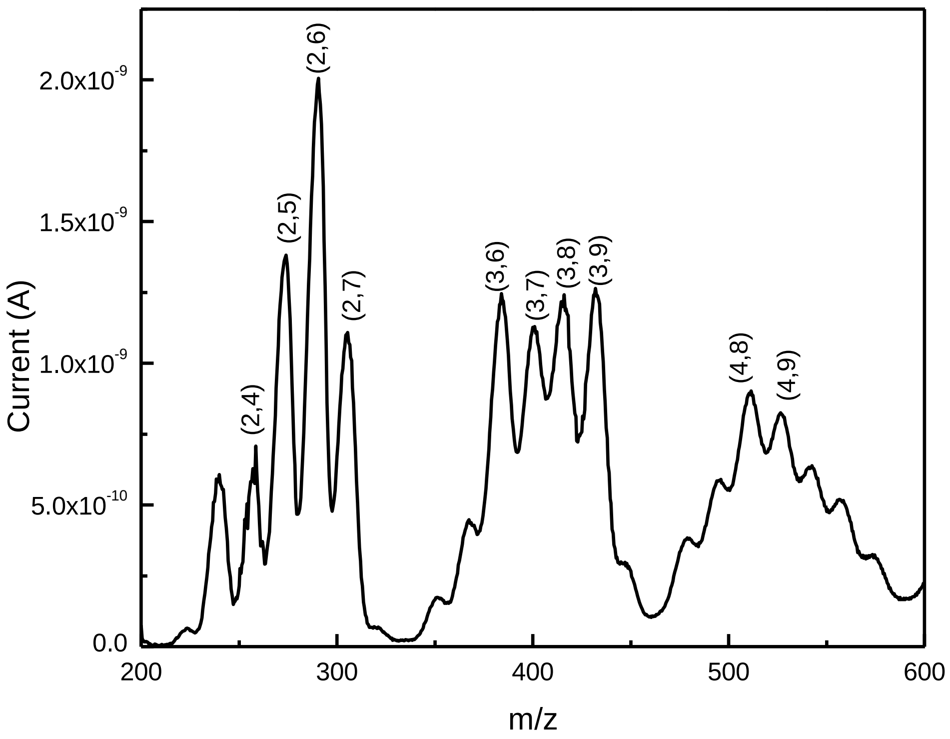

Figure 2.2 A mass spectrum of Mo_xO_y clusters reaching the Faraday cup in the UHV analysis chamber.

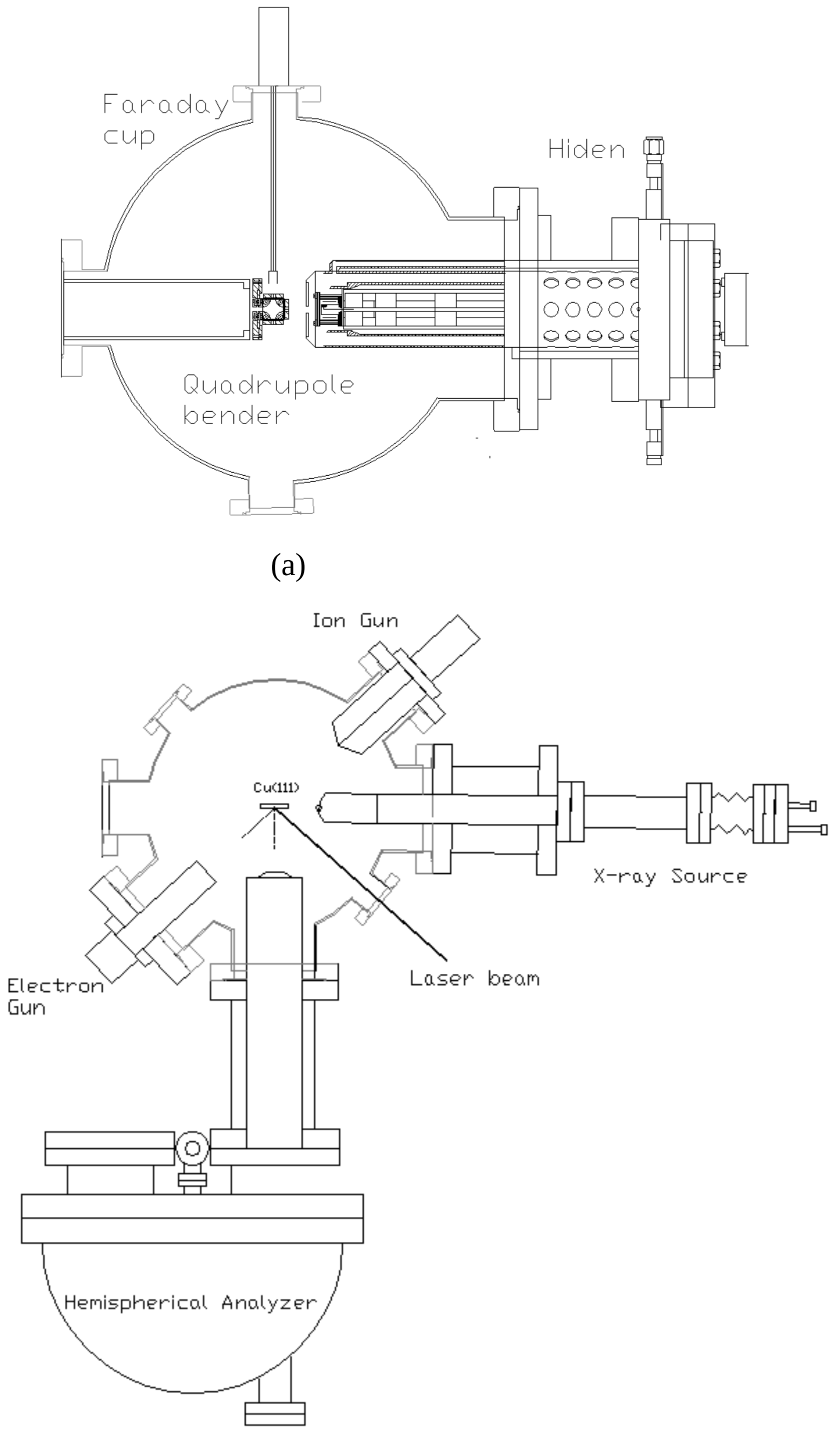

(a)

(b)

Figure 2.3. Schematic picture of the two levels of the UHV analysis chamber: lower (a) and upper (b).

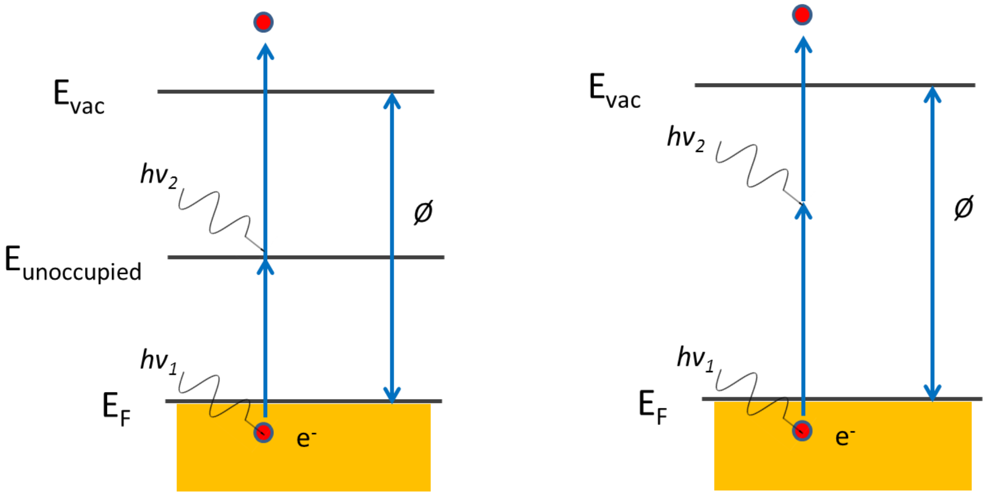

(a) (b)

Figure 2.4. Schematic energy diagram for the 2PPE process.

Chapter 3. Theoretical study of methanol synthesis from CO_2 hydrogenation on Cu clusters and Cu(111)

This section was published in *Phys. Chem. Chem. Phys.* 2010, 12, 9909.

3.1. Introduction

To improve the performance of current Cu-based catalysts for the production of methanol from CO_2 hydrogenation, extensive experimental[18-29] and theoretical[30-35] efforts have been devoted to understanding the underlying reaction mechanism; however, controversies over the mechanism still remain. Traditionally, two possible reaction pathways have been proposed. One is the formate pathway[18,19,27,28,36,37], where the CO_2 hydrogenation leads to formate (HCOO), followed by dioxomethylene (H_2COO) and formaldehyde (H_2CO). The other possible pathway (RWGS + CO-Hydro) involves the reverse water-gas-shift (RWGS) reaction, where CO_2 is converted to CO ($CO_2 + H_2 \rightarrow CO + H_2O$), followed by CO hydrogenation to methanol ($CO + 2H_2 \rightarrow CH_3OH$) via intermediate formyl (HCO) and H_2CO[30]. The intermediate H_2CO from either pathway can be further hydrogenated to methoxy (H_3CO) and the product CH_3OH. Previous studies suggest that CH_3OH synthesis proceeds *via* the formate pathway on Cu surfaces[18,19,27,32], Cu alloy surfaces[32] and Cu nanoparticles supported on metal oxides (ZnO, ZrO_2/SiO_2)[28,38]. A very recent theoretical study, however, predicts that the RWGS pathway is the main source of methanol on Cu/ZrO_2 with only a minor contribution from the formate reaction path.[30] In the latter study, hydrogenation of the HCOO intermediate was assumed to be the rate-limiting step[27] since it was found by postreaction analysis (XPS, TPD and HREELS) to be the most stable intermediate on Cu catalysts [18-20,27]. On the other hand, kinetic modeling showed that H_2COO hydrogenation was the rate-limiting step[18,33]. More recently, Mavrikakis et al. [34] reported that on Cu(111), the CO_2 hydrogenation product HCOO would be further hydrogenated to formic acid (HCOOH) rather than H_2COO. CH_3OH is produced by the subsequent hydrogenation of HCOOH to CH_3O_2, which leads to the formation of H_2CO and CH_3O via C-O bond scission. On the other hand, Mei and coworkers[35] claimed that HCOOH was most likely to desorb due to the weak binding or dissociate back to HCOO with a low barrier. Instead, they proposed that CO_2 hydrogenation would lead to the formation of hydrocarboxyl (trans-COOH) in the presence of H_2O. The CH_3OH is then produced via the intermediates dihydroxycarbene (COHOH), hydroxymethylidyne (COH), hydroxymethylene (HCOH) and hydroxymethyl (H_2COH).

In addition to uncertainties in the mechanism, there is also no general agreement as to the nature of the active site(s) and the effect of oxide support[2]. Metallic Cu has been proposed as the active site for supported catalysts[19,26,33], while the oxide support is thought to help the dispersion of the Cu particles and stabilize the metallic Cu sites[20]. Electronic interactions between Cu and the oxide support have been proposed as key to catalytic activity and still other studies suggest that the active sites are Cu cations[21] or the Cu-oxide interface[24,39].

In this chapter, a theoretical study of the synthesis of CH_3OH over extended Cu(111) surfaces and unsupported Cu_{29} nanoparticles will be presented. Previous experiment showed that Cu nanoparticles supported on ZnO($000\bar{1}$) are more active for the conversion of CO_2 to methanol than Cu(111)[8]. Our main objective is to understand what controls the yield of CH_3OH when moving from a close-packed Cu surface to a Cu nanoparticle.

3.2. Theoretical Method

The unrestricted density functional calculations were conducted using the code DMol^3 which allows the study of molecular systems and periodic surfaces. [40,41]. The generalized gradient approximation proposed by Perdew and Wang[9] was employed for the exchange and correlation functional. The electron-ion interaction was described using effective core potentials. The wave functions were expanded in terms of a double-numerical basis set with a polarization d-function on all non-hydrogen atoms. A global orbital cutoff of 5.5 Å was used. The Cu(111) surface was modeled by a three-layer slab with a (3×3) unit cell, separated by a 15-Å-thick vacuum layer. The bottom two layers of atoms were fixed in their optimized bulk positions while the top layer was allowed to relax together with the adsorbates. Brillouin-zone integrations were performed on a grid of 4×4×1 Monkhorst-Pack[11] special **k**-points. The Cu_{29} nanoparticle was allowed to fully optimize with no symmetry constraints. Instead of characterizing the transition state (TS) by frequency calculations, in this study, TS were identified by synchronous transit methods[42], which yield results close to those obtained by eigenvector following methods. The Linear Synchronous Transit (LST) was performed to bracket the maximum between the reactants and products, followed by repeated conjugate gradient minimizations and the Quadratic Synchronous Transit (QST) maximizations until a transition state was located. The convergence thresholds were set as that the root mean square (rms) forces on the atoms were smaller than 0.002Ha/Å.

3.3. Results and discussions

3.3.1. Methanol synthesis on Cu_{29} nanoparticle

Cu_{29} was considered in our DFT calculations as a model to simulate the Cu nanoparticles on ZnO(000ī), assuming that ZnO behaves only as a support and does not participate in the reaction directly. According to the experiments, this is a reasonable assumption, where the O-terminated ZnO(000ī) was observed covered by carbonate and formate after the reaction and both intermediates do not seem to be active to produce methanol[8]. Therefore, ZnO was only considered as a support to prevent the sintering of copper particles. The Cu_{29} nanoparticle has a pyramidal structure formed by a combination of (100) and (111) faces and a diameter of 1.2 nm (Figure 3.1). According to previous studies, this model is valid to capture the effects of the low-coordinated sites and the flexibility of the nanoparticle, both of which play essential roles in many catalytic processes.[43-45]

According to our calculations, Cu_{29} is able to dissociate H_2 spontaneously since the H-H bond was broken during the geometry optimization. It is not surprising since similar behavior was also observed in the previous study of Au_{29} nanoparticles[43], considering that Cu has been known to be more active than Au towards H_2 dissociation[46]. The atomic hydrogen binds to the top sites of Cu_{29} with a binding energy of -0.34eV (Figure 3.2). Previous DFT calculations show that CO_2 weakly adsorbs on bare Cu(111).[47,48] In presence of adsorbed H, the CO_2 molecule, cannot bind to the nanoparticle, but instead reacts with H atoms via an Eley-Rideal (ER) mechanism, in which gaseous CO_2 directly reacts with an adsorbed H atom. Besides, CO_2 will not physisorb on Cu at the reaction temperature, 573 K. This is consistent with the experimental observations that the increase of adsorbed H coverage only hinders the dissociative adsorption of H_2 on Cu, but not the adsorption of CO_2[49]. Such a mechanism was also confirmed by the DFT studies.[50,51]

There are two possible pathways for the first hydrogenation of CO_2 (Figure 3.2). One leads to the formation of HCOO ($CO_2 + H^* + * \rightarrow HCOO^{**}$) and the other results in HOCO (carboxyl) production ($CO_2 + H^* + * \rightarrow HOCO^{**}$). The HCOO binds to the top site of the nanoparticle in a bidentate configuration through two O atoms (η^2-O, O), while the carboxyl binds to the same site with both C and O atoms interacting with the nanoparticle (η^2-C, O). Our results show that the HCOO pathway is energetically favored since it is highly exothermic with reaction energy (ΔE) of -1.05 eV and an activation barrier (E_a) as low as +0.04 eV. In contrast, the HOCO is much less stable on the nanoparticle and the formation reaction is thermoneutral (ΔE= +0.14eV). Therefore, CO_2 hydrogenation is likely to proceed via the formate pathway.

Similarly, two possible products were considered for the further hydrogenation of HCOO, i.e., H2COO and HCOOH (Figure 3.3). The formation of HCOOH is a highly activated step (ΔE = +1.21eV and E_a = +1.90eV); in contrast, the H_2COO formation is much less endothermic (ΔE = +0.39eV) and the reaction barrier (E_a = +1.34eV) is 0.56eV lower than that of the HCOOH formation. The preference for H_2COO formation can be attributed to the relative stabilities of different binding configurations. Figure 3.3 shows that H_2COO strongly binds to Cu_{29} through the two O atoms. In the case of HCOOH, it is anchored through only one O atom and the dangling OH of HCOOH points away from the nanoparticle. Therefore, as shown in Figure 3.3, the H_2COO^{**} conformation on Cu_{29} is 0.82eV more stable than HCOOH*, which contributes to a lower activation energy. As a result, the reaction prefers to proceed through C-H bond formation rather than O-H bond formation.

The two possible pathways for the further H_2COO hydrogenation were shown in Figure 3.3. The H_2COO intermediate can react via either the direct hydrogenation ($H_2COO^{**} + 1/2H_2 \rightarrow H_2COOH^{**}$) or the H-guided dissociation ($H_2COO^{**} + 1/2H_2 \rightarrow H_2CO^* + OH^*$) . The production of H_3COO was not included because such species do not survive during the geometry optimization. Depending on the different initial geometries, it dissociates back into either HCOO and gas-phase H_2 or H_2COO + H. The direct hydrogenation of H_2COO is not energetically preferred ($\Delta E = +0.17eV$, $E_a = +1.69eV$), though the H_2COOH product species easily dissociates into H_2CO and hydroxyl (OH) ($\Delta E = +0.28eV$, $E_a = +0.44eV$). Instead, the direct formation of H_2CO and OH via the H-guided dissociation is more favorable ($\Delta E = +0.45eV$, $E_a = +1.41eV$) without going through the H_2COOH intermediate. The resulting OH fragment is likely to combine with an H atom and desorb as gas-phase water under high temperature reaction conditions, which releases the Cu top site for further H atom adsorption and hydrogenation. The binding configuration of H_2CO changes from η^1-O (Figure 3.3) to η^2-C,O (Figure 3.4) to satisfy the tendency of tetravalency of C, by which H_2CO binds more strongly to the nanoparticle by -0.11eV.

According to our calculations, the η^2-H_2CO species is likely hydrogenated to η^1-H_3CO ($\Delta E = -1.18eV$, $E_a = +0.11eV$), where the C-Cu bond is broken and the H_3CO binds via an O-Cu bond (Figure 3.4). Hydrogenation to form CH_2OH ($\Delta E = -0.22eV$) and the H-guided dissociation ($H_2CO^{**} + 1/2H_2 \rightarrow CH_2^* + OH^*$, $\Delta E = -0.77eV$, $E_a = +1.29eV$) cannot compete with it energetically. Finally, CH_3OH is produced via

H_3CO hydrogenation (ΔE = -0.04eV, E_a = +0.88eV). The alternative H-guided dissociation of H_3CO to produce CH_3 + HO has a much higher activation energy (ΔE = -0.55eV, E_a = +1.58eV; Figure 3.4).

In summary, the methanol synthesis reaction on a Cu_{29} nanoparticle proceeds via the pathway as follows,

$$H_2 + 2^* \rightarrow 2H^* \qquad (1)$$

$$H^* + CO_2 \rightarrow HCOO^{**} \qquad (2)$$

$$HCOO^{**} + H^* \rightarrow H_2COO^{**} + ^* \qquad (3)$$

$$H_2COO^{**} + H^* \rightarrow H_2CO^{**} + OH^* \qquad (4)$$

$$OH^* + H^* \rightarrow H_2O + 2^* \qquad (5)$$

$$H_2CO^{**} + H^* \rightarrow H_3CO^* + 2^* \qquad (6)$$

$$H_3CO^* + H^* \rightarrow CH_3OH^* + ^* \qquad (7)$$

$$CH_3OH^* \rightarrow CH_3OH + ^* \qquad (8)$$

where “*” represents a free site and “*X” stands for the adsorbed X species. The corresponding geometries of TS are displayed in Figure 3.6. During the reaction, Cu_{29} stays intact, but interaction with adsorbates induces some structural distortion. The flexibility of the Cu_{29} nanoparticle gives rise to added stability to adsorbate conformations that is not seen for the more rigid Cu(111) surface.

3.3.2.Methanol synthesis on Cu(111) surface

By comparison to Cu nanoparticles, the synthesis of methanol on extended Cu surfaces has been more extensively studied. Hu et al. studied the reaction mechanism on Cu(100) using dipped adcluster model (DAM) combined with *ab initio* Hartree-Fock (HF) and second-order Møller-Plesset (MP2).[31] They identified the reaction intermediates as HCOO, H_2COO, H_2CO and H_3CO, and the rate-limiting step is the hydrogenation of HCOO to H_2COO ($E_a = +0.97eV$). On Cu(111), several important elementary steps were studied. Mavrikakis et al.[52] found that on Cu(111), CO_2 reacts with H to produce bidentate HCOO ($E_a = +0.83eV$, $\Delta E = -0.30eV$) via a monodentate HCOO intermediate. A similar pathway was also identified by Wang et al.[50] and Mei et al[51]. In particular, Mei et al., showed that HCOO hydrogenation to H_2COO ($E_a = +1.24eV$) is energetically preferred over the HCOO decomposition pathway ($E_a = +1.70eV$). To date, a complete theoretical analysis of the reaction pathway for methanol synthesis on Cu(111) has not yet been reported.

In this study, the complete reaction pathway of methanol synthesis on the Cu(111) surface was studied. The geometries of the reaction intermediates and TS are displayed in Figure 3.7 and the energetics is shown in Figure 3.5. Molecular hydrogen undergoes dissociative adsorption on Cu(111) with an H atom binding energy of -0.30 eV. The H atoms prefer to reside on the three-fold hollow site on Cu(111), which agrees well with previous theoretical studies[53,54]. The corresponding Ea is +0.93eV, and the H-H bond distance of the TS is 1.34 Å. Both the activation barrier and the H-H bond length of TS agrees reasonably well with that found by Hammer et al[55], when considering the differences in TS search method employed in the two studies.

Similar to the case of Cu_{29}, CO_2 cannot adsorb on Cu(111), but reacts with H atoms to form bidentate HCOO via the ER mechanism with $\Delta E = -0.17eV$ and $E_a = +1.23eV$. Further hydrogenation of HCOO to form H_2COO is endothermic ($\Delta E = +0.70eV$) with E_a as high as +1.60eV, where H_2COO binds to the surface through both of the O atoms. The more energetically favorable reaction with H atoms is the dissociation of H_2COO into H_2CO and OH species. The OH species preferentially adsorb on the three-fold hollow sites, while the H_2CO binds to the surface weakly with a calculated binding energy of only -0.01eV. The C-O bond is roughly parallel to the surface and the C and O atoms are 3.86 Å above the surface. The reaction is slightly downhill (ΔE= -0.14eV) with an E_a = +1.60eV. Further hydrogenation of H_2CO leads to the formation of CH_3O residing on the three-fold hollow sites of the surface (ΔE = -1.16eV, E_a =+0.69eV), which is eventually hydrogenated to CH_3OH (ΔE = -0.06eV, E_a = +1.15eV). Our calculations are consistent with previous theoretical work performed by Mavrikakis et al.,[56] who found that H_2CO interacts with the Cu surface very weakly (binding energy of -0.10eV) and the production of H_3CO by H_2CO hydrogenation is facile (ΔE = -0.97eV, E_a = +0.45eV).

Generally speaking, the results from the present calculations on Cu(111) are in good agreement with previous theoretical studies, though our calculations tend to yield somewhat higher activation barriers. These differences can be attributed to the different methods used for the TS search and does not compromise the validity of this study since we are primarily interested in the relative energies of one step to another.

3.3.3. Kinetic analysis for methanol synthesis on Cu_{29} and Cu(111)

The complete energy profiles for the methanol synthesis reaction on Cu_{29} nanoparticle and Cu(111) surface are shown in Figure 3.5. The energies are presented with respect to a bare nanoparticle or clean Cu(111) surface, a CO_2 molecule and three H_2 molecules in gas phase. One can see that the reaction on Cu(111) and Cu_{29} follows the same formate mechanism *via* the HCOO species and the reaction rate is controlled by the same step, i.e., H_2COO (TS3) hydrogenation. However, the energies along the reaction pathways differ significantly. Compared to Cu(111), the H atom bonds to Cu_{29} more strongly by occupying the corner sites, which are more flexible and generally considered more active than the terrace sites due to their low coordination.[45] Similarly, the key intermediates, HCOO, H_2COO and H_2CO, are also more stable on Cu_{29} than on Cu(111) by +0.91eV, +1.23eV and +0.63eV, respectively (Figure 3.5). As a result, the corresponding activation barrier for the rate-limiting H_2COO hydrogenation is lowered by 0.19 eV when moving from Cu(111) to Cu_{29}, and therefore a higher activity is expected. A similar relationship between binding activity and reaction barrier was also observed in our previous study on the WGS reaction on Cu and Au nanoparticles and surfaces,[45] showing that the binding energy of the key intermediate, OH, correlates well with the overall WGS activity.

Similar to previous kinetic studies,[45,57-59] we also considered the barrier of the rate-limiting step along the reaction pathway, E_a^h, as a descriptor to estimate the relative catalytic activity. On both Cu_{29} and Cu(111), Ea^h corresponds to the energy difference between dioxomethylene ($H_2COO^* + 2H_2(g)$, Figure 3.5) and the transition state for H_2COO hydrogenation (TS3, Figure 3.5). For the synthesis of CH_3OH on Cu(111), E_a^h equals to +1.60 eV, while it is lowered to +1.41eV in the case of Cu_{29}. Using the Arrehenius rate expression, rate ~ $\nu e^{-\Delta Ea/kT}$, and assuming the same pre-exponential factor for reactions on both Cu_{29} and Cu(111), the differences in activation energies imply a methanol production rate that is ~ 50 times faster on Cu_{29} than on Cu(111). The calculated increase in rate agrees very well with experimental results, showing that rate increase on going from Cu(111) and ZnO-supported Cu nanoparticles[8]. Note, as documented by Stoltze, et al.,[60] the measured apparent activation energy and the barrier of the rate-limiting step calculated from DFT cannot be compared quantitatively, while the qualitative comparison of the variation from Cu(111) to Cu particles is more meaningful, which is our interest here. Two factors contribute to the enhanced ability of a Cu nanoparticle to convert CO_2 to methanol. As shown in Figure 3.5, compared with Cu(111), the reactants, intermediates, transition states and products are more stable at the low-coordinated sites of Cu_{29}. For CO_2 hydrogenation to methanol, our calculations shows that the slow kinetics on Cu(111) is associated with low stability of H_2COO and H_2CO. Given that, the number of active low-coordinated sites is of great importance to the overall activity. In addition, the structural flexibility of Cu_{29} contributes to stabilize the intermediates and transition states on the surface. One can see that both factors must be taken into consideration when dealing with the reactions on metal particles.

3.3.4. RWGS and CO hydrogenation reaction on Cu_{29} nanoparticle

Besides methanol synthesis, the RWGS reaction also occurs over the same catalyst and under the same conditions simultaneously. Campbell et al.[20] suggested that the RWGS reaction was roughly 3 orders of magnitude faster than methanol synthesis over Cu(110) at a total pressure of 5.1 bar ($CO_2 : H_2 = 1 : 11$). Similar kinetics were also observed on polycrystalline Cu[26]. To understand the effect of RWGS in the methanol synthesis reaction over Cu nanoparticles, we also considered the catalytic activity of Cu_{29} for RWGS in this study.

The reaction mechanism of WGS on Cu_{29} nanoparticles were reported previously[45]. Therefore, the intermediates involved in the RWGS reaction on the Cu_{29} nanoparticle and the relative energetics are also known based on the principle of microscopic reversibility. Again, the active sites for the RWGS on Cu_{29}, is the low-coordinated Cu sites. This agrees well with recent studies of WGS reaction on Cu(321), where the presence of step sites affects the activity of WGS and hence the RWGS significantly.[61]

As shown in Figure 3.8, for the RWGS reaction on Cu_{29}, the activation energy for the rate-limiting step , E_a^h, corresponds to the energy difference between CO* + H* + OH* + $2H_2(g)$ and TS3. Compared with methanol synthesis on Cu_{29}, E_a^h for the RWGS is 0.27eV lower (E_a^h(RWGS) = +1.14eV). The estimated reaction rate of RWGS is $\sim 10^3$ per second per site at T= 573K, which is two orders of magnitude larger than that for methanol synthesis reaction. This also agrees with experimental observations[8,20,26] that show that CO_2 hydrogenation over a Cu catalyst produces a significant amount of CO.

The question that now arises is why the CO produced from the RWGS reaction is a terminal product and does not react with hydrogen? To address this question, the hydrogenation of CO on Cu_{29} was also studied. Two possible products were considered for the first step CO hydrogenation: HCO and COH (Figure 3.9). The production of HCO (ΔE= +0.37eV, Ea= +0.40eV) is energetically more favorable than the highly endothermic COH production (ΔE= +0.94eV). The further hydrogenation of HCO leads to H_2CO (ΔE= -0.42eV, Ea= +0.45eV), rather than HCOH (ΔE= +0.68eV) (Figure 3.9). This is not surprising since H_2CO binds to the nanoparticle much stronger (η^2-C,O), while HCOH interacts with the nanoparticle only through the C atom with a dangling OH.

Eventually, the H_2CO intermediate will follow the same pathway as shown in Figure 3.4 to form CH_3OH. Note that E_a^h for CO hydrogenation to CH_3OH, which corresponds to the energy difference between H_3CO* + $H_2O(g)$ + $1/2H_2(g)$ and TS7

(Figure 3.8), is not as high as that for CO_2 hydrogenation via formate pathway (Figure 3.5). Considering the fast kinetics of the RWGS reaction as demonstrated above, one would expect that the CH_3OH synthesis via the RWGS pathway should dominate the formate pathway. However, our calculations (Figure 3.8) show that the reverse reaction in which CO is hydrogenated to HCO is almost barrierless (E_a = +0.03eV) and there is a barrier of +0.45eV to be overcome for the further hydrogenation to H_2CO. Hence, the HCO intermediate is not stable, and quickly dissociates to CO* and H* before further hydrogenation. Since the formation of HCO cannot compete with its decomposition, CO from the RWGS reaction becomes a significant product as observed in our experiment. This suggests that the hydrogen coverage under reaction condition was not high enough to shift the equilibrium of $CO^* + H^* \leftrightarrow HCO^* + *$ towards the direction of HCO formation since the HCO dehydrogenation is almost barrierless. In fact, HCO has been identified as an essential intermediate species in many reactions associated with CO hydrogenation on various metals, such as Pd, Pt, Ru, Co, Ni and Rh.[57,62-64] The stability of HCO is identified as a key factor which may affect the overall reaction significantly. In the case of Cu, the CH_3OH synthesis via the RWGS pathway is hindered by the low stability of the HCO intermediate, which eventually dissociates into CO and terminates the CH_3OH formation via the RWGS pathway.

Overall, methanol synthesis on Cu from CO_2 hydrogenation proceeds via the formate pathway. In contrast, the faster RWGS pathway does not lead to the production of methanol, but the accumulation of CO, due to the low stability of the CO hydrogenation product, HCO, which prefers the H-C bond cleavage on Cu. The flexibility and the active low-coordinated sites of Cu nanoparticles play key roles in the methanol synthesis from CO_2 by helping to stabilize key intermediates (HCOO, H_2COO, H_2CO and H_3CO), the corresponding transition states and thereby lower the barrier for the rate-limiting H_2COO hydrogenation.

3.4. Conclusions

A theoretical studies was carried out to investigate the methanol synthesis via CO_2 hydrogenation on Cu(111) and unsupported Cu_{29} nanoparticles. According to our calculated results, methanol synthesis on both surfaces follows the formate pathway via intermediates HCOO, H_2COO, H_2CO and H_3CO, and the rate-limiting step is H_2COO hydrogenation. Compared with that on Cu(111), the barrier for the rate-limiting step of methanol synthesis reaction on Cu_{29} is 0.19 eV lower which corresponds to a reaction rate ~50 times faster (T = 573K), which is in qualitative agreement with experimental measurements of ~15 times[8]. The activity enhancement can be attributed to the flexibility and the presence of the active low-coordinated Cu sites in the nanoparticle, which significantly stabilize the key intermediates and the corresponding transition states, and therefore lower the barrier for the rate-limiting hydrogenation process. These results clearly illustrate the need to consider catalyst particle-size effects in methanol synthesis reaction.

The competing RWGS reaction was also considered. Compared to the methanol synthesis, the barrier of the slowest step of the RWGS is calculated to be -0.27 eV lower, with a corresponding reaction rate that is faster by a factor of $\sim 10^2$ at T= 573K. This is consistent with experimental observations, showing that the RWGS reaction is 2-3 orders of magnitude faster and that the dominant product on Cu catalyst is CO rather than methanol[8]. Our calculations indicate that methanol production from CO hydrogenation via the RWGS pathway is hindered by the first hydrogenation of CO to HCO. The latter is not stable on Cu and prefers to dissociate into CO and H. Therefore, the faster RWGS only leads to the accumulation of CO, rather the methanol formation.

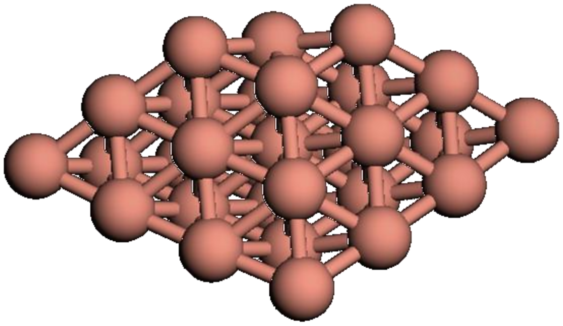

Figure 3.1. Structure for Cu_{29} nanoparticle

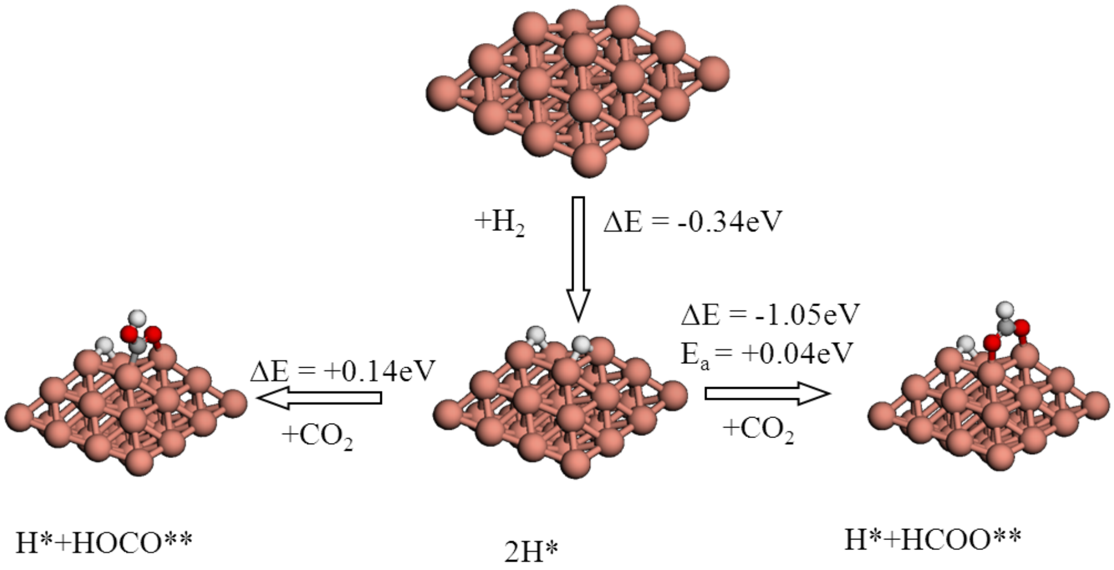

Figure 3.2. Possible reaction pathways for CO_2 hydrogenation on Cu_{29} (Big brown: Cu; small white: H; small red: O; small grey: C)

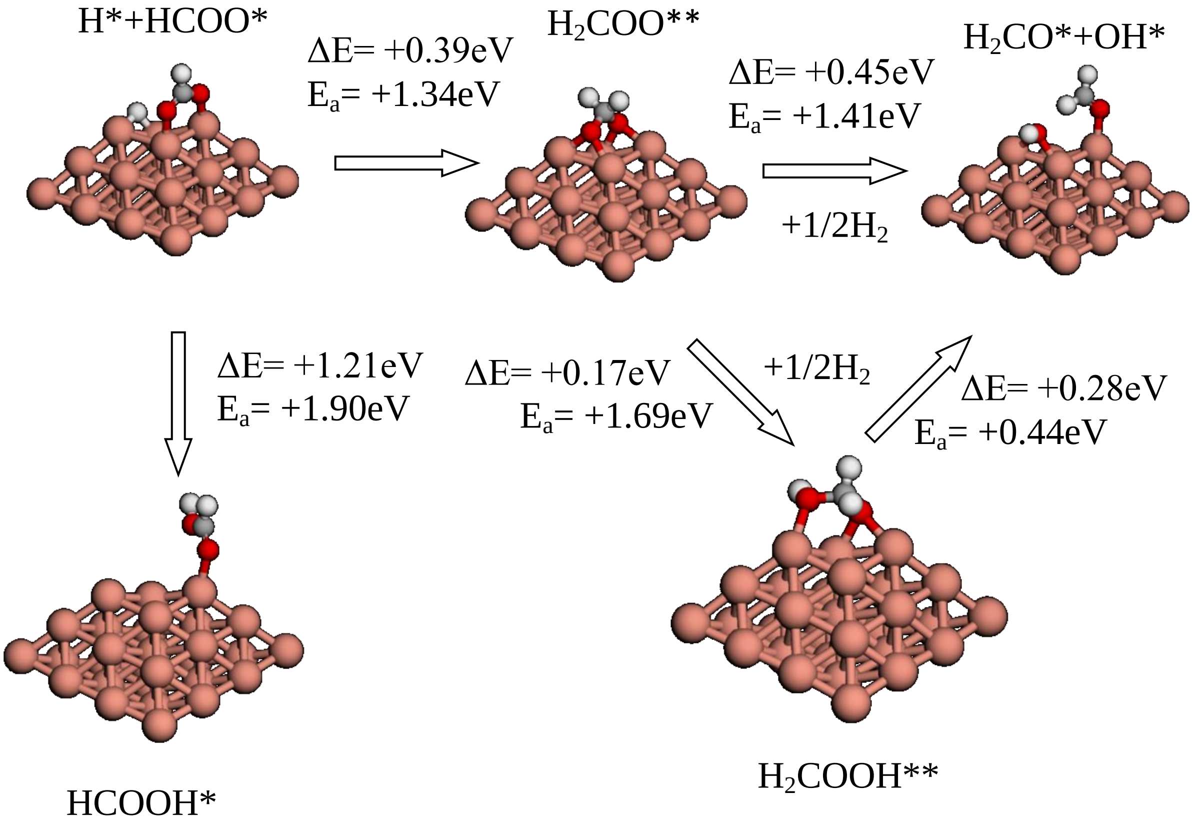

Figure 3.3. Possible reaction pathways for formate and dioxomethylene hydrogenation on Cu_{29} (Big brown: Cu; small white: H; small red: O; small grey: C)

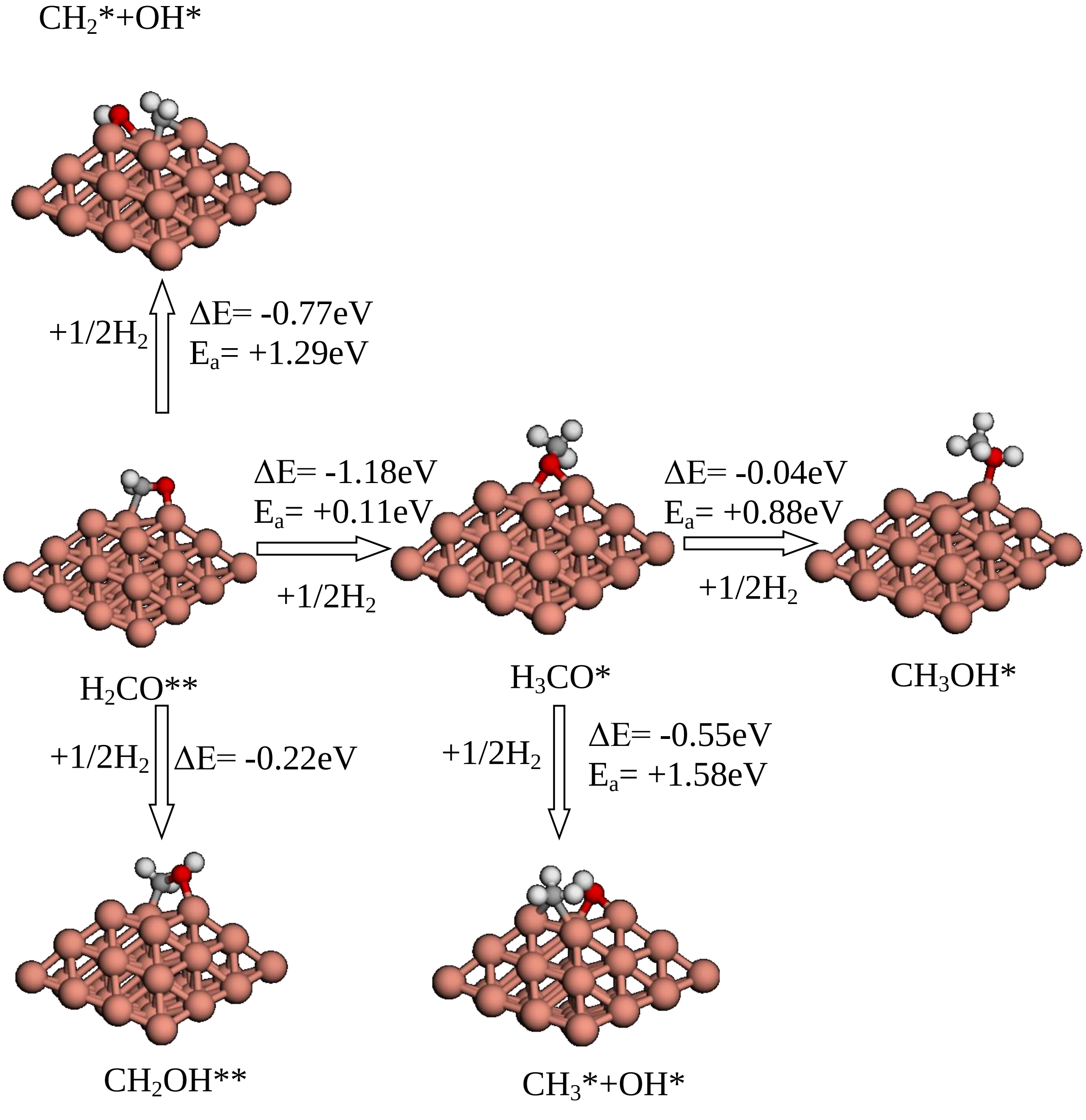

Figure 3.4. Possible reaction pathways for formaldehyde and methoxy hydrogenation on Cu_{29} (Big brown: Cu; small white: H; small red: O; small grey: C)

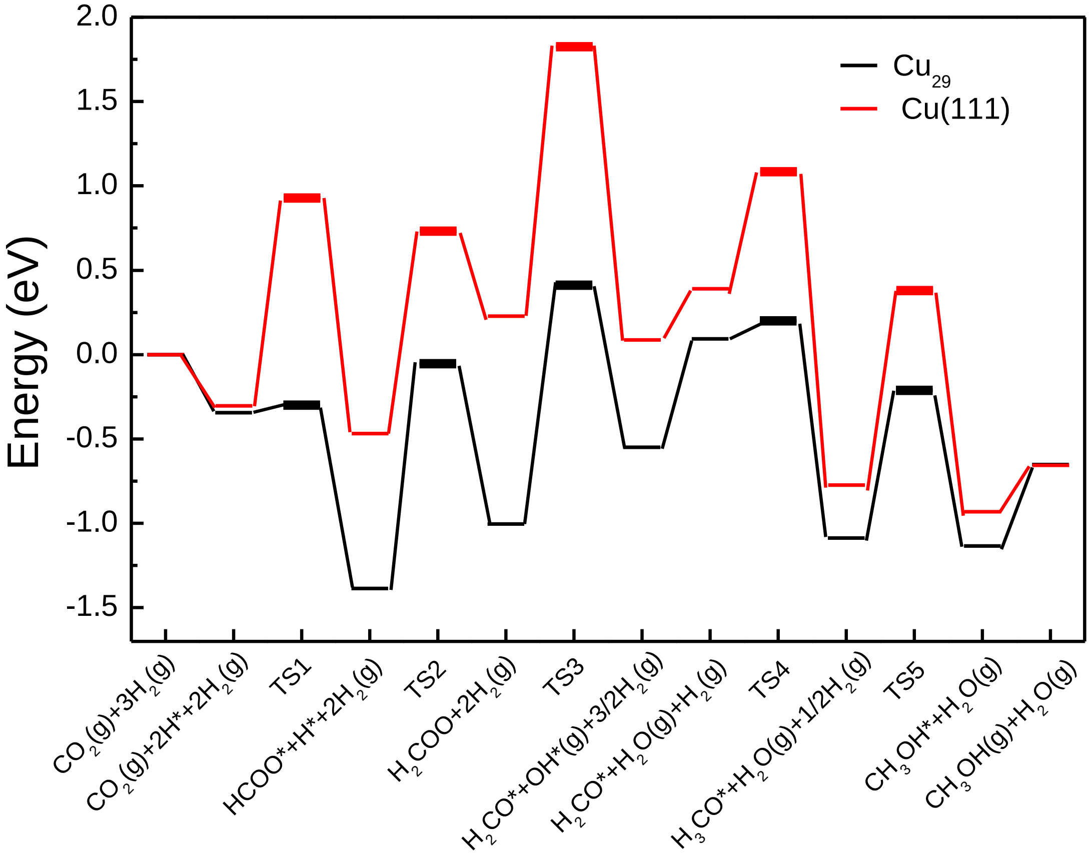

Figure 3.5. Potential energy diagram for the methanol synthesis reaction on the Cu(111) surface and Cu_{29} nanoparticle, where thin bar represents the intermediates and thick bar represents the transition states. The upper diagram (in red) corresponds to Cu(111) and the lower diagram (in black) corresponds to Cu_{29}.

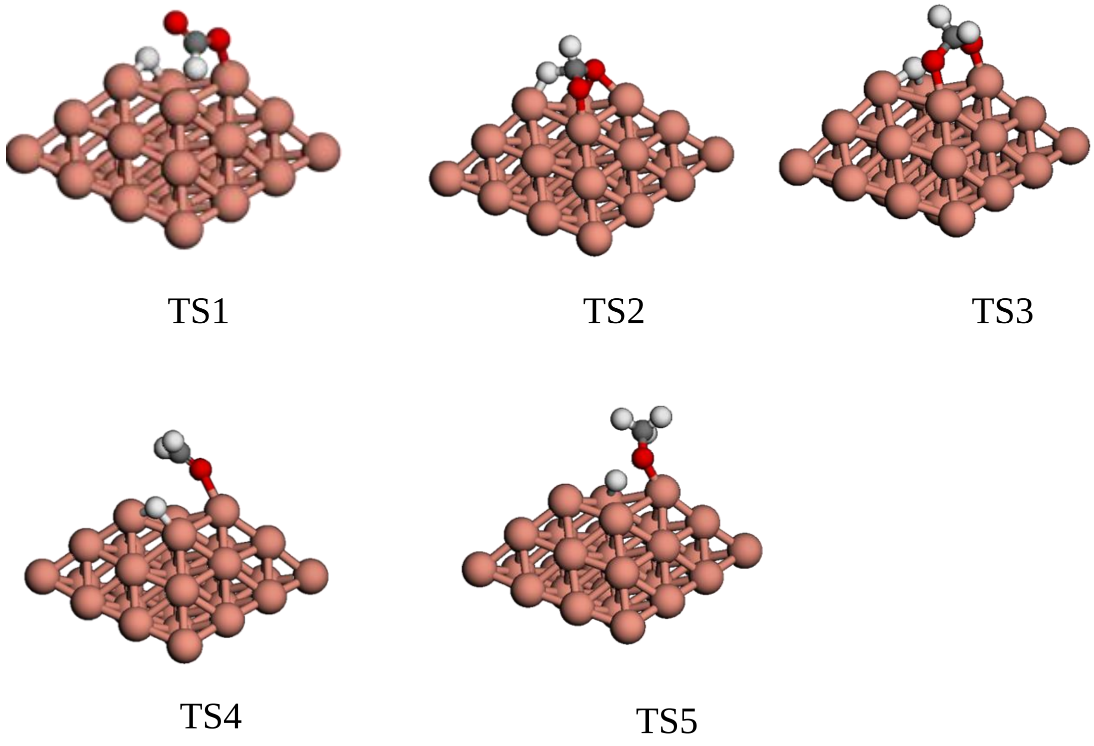

TS1 TS2 TS3

TS4 TS5

Figure 3.6. Structures of intermediates and transition states (TS) involved in the methanol synthesis reaction on the Cu29 nanoparticle (Big brown: Cu; small white: H; small red: O; small grey: C)

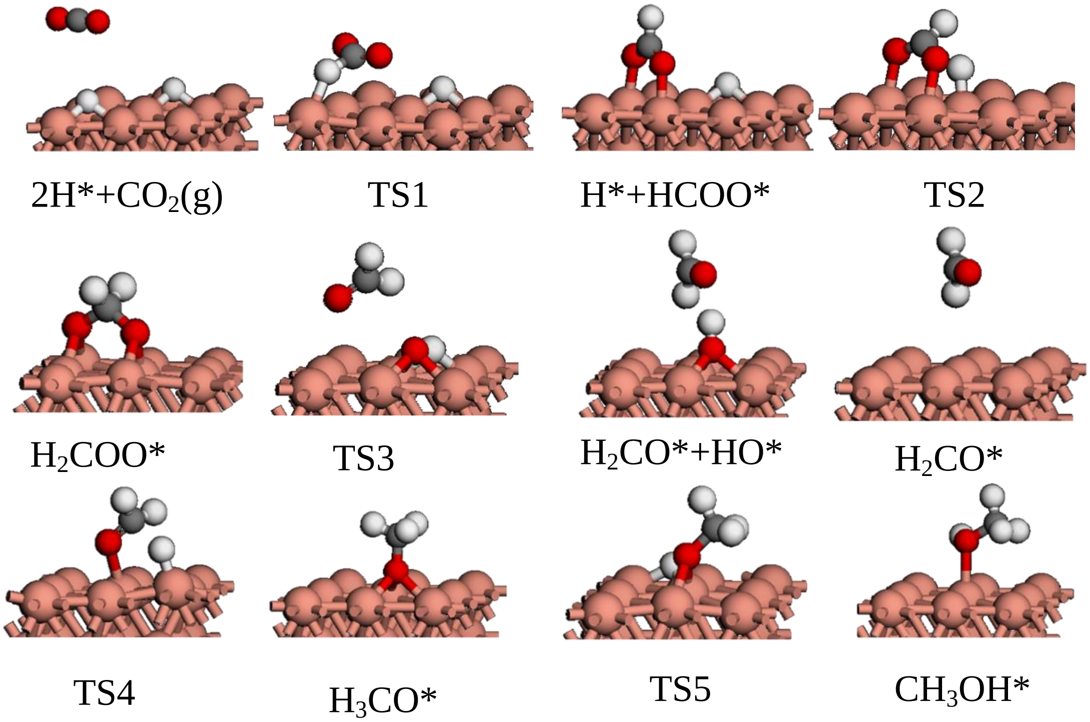

$2H^*+CO_2(g)$ TS1 H^*+HCOO^* TS2

H_2COO^* TS3 $H_2CO^*+HO^*$ H_2CO^*

TS4 H_3CO^* TS5 CH_3OH^*

Figure 3.7 Structures of intermediates and transition states (TS) involved in the methanol synthesis reaction on the Cu(111) surface (Big brown: Cu; small white: H; small red: O; small grey: C)

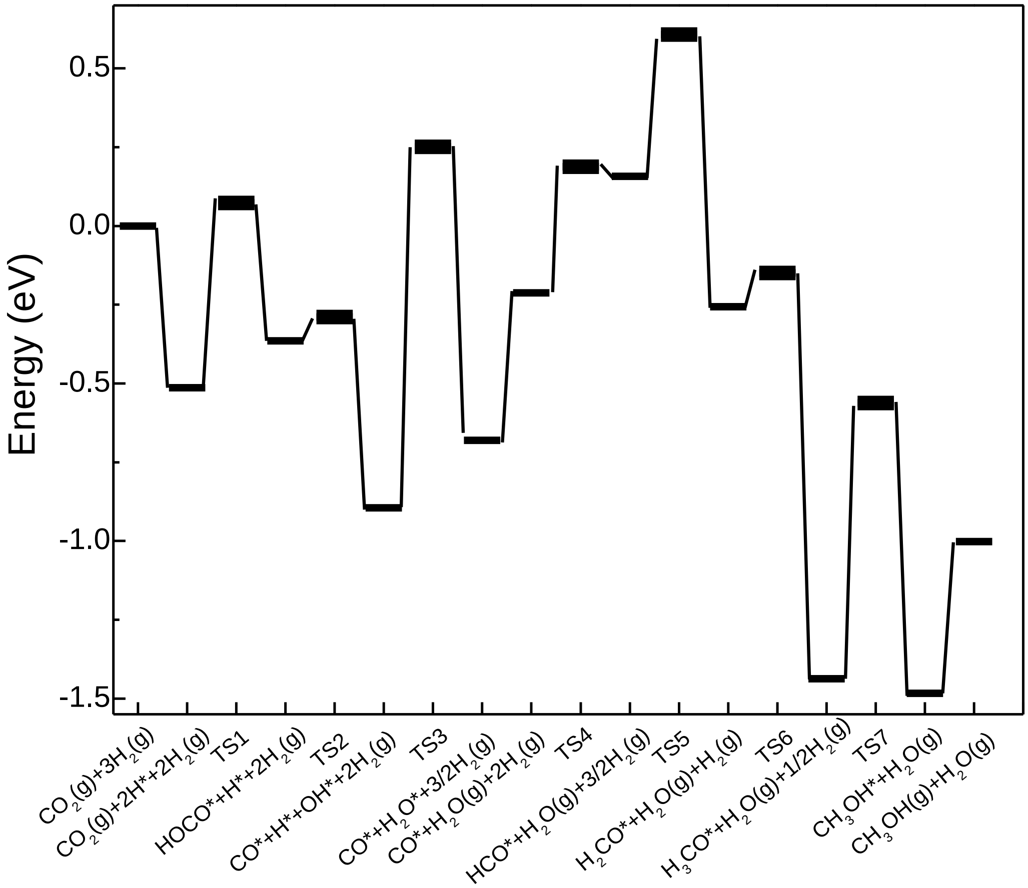

Figure 3.8. Potential energy diagram for the methanol synthesis reaction via RWGS pathway on the Cu_{29} nanoparticle, where thin bar represents the intermediates and thick bar represents the transition states.

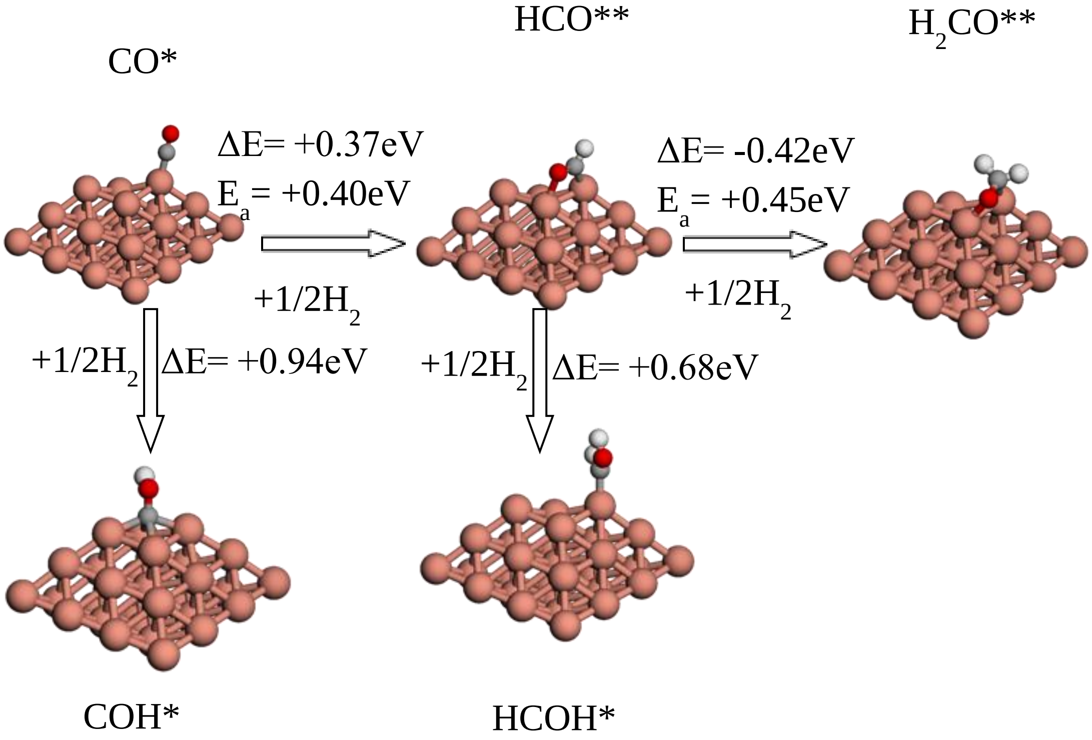

Figure 3.9. Possible reaction pathways for CO hydrogenation on Cu_{29} (Big brown: Cu; small white: H; small red: O; small grey: C)

Chapter 4. Theoretical study of methanol synthesis from CO_2 hydrogenation on metal-doped Cu(111) surfaces

This section was published in *J. Phys. Chem. C,* 2012, *116* (1), 248.

4.1. Introduction

Two conventional reaction pathways have been proposed for methanol synthesis reaction from CO_2 hydrogenation over Cu-based catalysts. One is the formate pathway[18,19,27,28,36,37], where the reaction proceeds through the formation of HCOO, H_2COO, H_2CO, H_3CO and the final product, CH_3OH. The other possible pathway (RWGS + CO-Hydro) involves the reverse water-gas-shift (RWGS) reaction, where CO_2 is converted to CO ($CO_2 + H_2 \rightarrow CO + H_2O$) through HOCO intermediate, followed by CO hydrogenation to methanol ($CO + 2H_2 \rightarrow CH_3OH$) via intermediate formyl (HCO) and H_2CO[30]. More recently, Mavrikakis et al. [34] reported a modified formate pathway on Cu(111). It also starts with the HCOO formation, while different from traditional formate, the HCOOH was formed rather than H_2COO. Instead of desorption, HCOOH is further hydrogenated to form H_2COOH. The subsequent reaction steps overlaps with traditional formation pathway to produce H_2CO and CH_3OH. On the other hand, Mei and coworkers[35] proposed a H_2O-mediated mechanism. The H source for hydrogenation is from H_2O, while one of the O-H bonds in H_2O breaks and the H reacts with the adsorbed CO_2 to form HOCO, while the remaining OH group reacts with the surface H to produce H_2O. The produced HOCO is further hydrogenated into dihydrocarbene (COHOH) by O-H bond formation. The further dissociation of COHOH leads to the formation of COH and finally CH_3OH via the intermediates HCOH and H_2COH.

This chapter mainly focuses on the effect of metal dopants on Cu(111) to the two traditional pathways. The reaction network scheme of the two pathways is displayed in Figure 4.1. Our previous study[8] showed that on the Cu(111) surface, CH_3OH synthesis from CO_2 and H_2 through the formate pathway is limited by the high barrier for hydrogenation of HCOO and H_2COO. The alternative RWGS + CO-Hydro pathway is hindered by the hydrogenation of CO and formyl (HCO). Instead of further hydrogenation, CO prefers to desorb from the surface and HCO favors to dissociate back to CO and H. Thus, an extensive amount of CO was observed desorbing from the catalysts experimentally and the methanol yield on Cu(111) was low.[8] To improve the catalytic performance, a promoter is needed to lower the barriers for HCOO and H_2COO hydrogenations and therefore enhance the production of CH_3OH via the formate pathway. Similarly, CO and HCO should be stabilized so that CO can be further hydrogenated to CH_3OH. In particular, accelerating the conversion of CO and HCO to CH_3OH seems to be more effective on Cu, which is a much faster reaction than the CH_3OH synthesis via the formate pathway.[8]

Alloys have been extensively used to improve the alcohol synthesis and syngas conversion[65-68]. However, so far there is no systematic study of the promoting effect of alloying on CH_3OH synthesis. In this study, the effect of doping Ni, Pd, Pt, Rh and Au on the CH_3OH synthesis from CO_2 and H_2 on Cu(111) was investigated. Previous experimental studies[69-71] have proposed that compared with the clean Cu(100) surface, the Ni modified Cu(100) surface displayed a superior catalytic activity with respect to the CH_3OH synthesis from a mixture of CO, CO_2 and H_2. Such enhancement was attributed to the capability of Ni to promote CH_3OH production by activating CO_2[72] and stabilizing the intermediates due to the higher oxygen affinity of Ni compared to Cu. Later, a theoretical study by Nørskov et al. [73] also suggested that CH_3OH synthesis from CO and H_2 could take place on the Ni(111) surface. Pd and Pt were also considered as potential dopants to enhance the CH_3OH production from direct CO hydrogenation because CO binds more strongly on Pd and Pt compared to Cu[74]. A stronger CO binding on PdCu alloy compared with Cu was observed in the previous DFT study[75]. Moreover, both Pd single crystal[76] and oxide supported Pd catalysts[77-80] have been shown to be catalytically active towards CH_3OH synthesis from CO hydrogenation. Rh is known as an active catalyst for CO and CO_2 hydrogenation even though the selectivity towards CH_3OH is low[81-83]. The hydrogenation of CO and CO_2 on Rh catalysts tends to form ethanol[58,84] and hydrocarbons[80,85]. However, by alloying with Co[86,87] or doping with alkali and alkaline earth oxides[88], the CH_3OH selectivity can be improved. Similar as the case of PdCu alloy, previous studies[89,90] showed that CO preferred to bind to Rh sites on the RhCu alloy and the binding of CO to RhCu was stronger than that to Cu. For the purposes of comparison, Au was also included as a possible dopant in this study.

In this study, density functional theory (DFT) calculations were first performed to determine the reaction mechanisms on the Cu(111) surface doped by metals, providing more insight into the effects of doping on the preference of reaction pathways, the possible intermediates and transition states. To further elucidate the reaction kinetics, a KMC study based on the DFT results was also carried out. The KMC simulation is able to properly evaluate the surface chemical kinetics by combining the accurate description of the elementary steps from the DFT calculations with an account for their statistical interplay[91]. The results of such simulation include the rate of each elementary step at any time so that it can be used to evaluate the catalytic activity by averaging the rate during steady-state operation. In the present study, the KMC study was conducted to estimate the CH_3OH yield under experimental conditions. A sensitivity analysis based on the KMC simulation also allows us to identify the descriptors which can describe the catalytic activity and therefore are useful for the rational design of better of Cu-based catalysts for CH_3OH synthesis.

4.2. Theoretical method

The unrestricted DFT calculations were conducted using the code DMol^3 [18,19]. The generalized gradient approximation proposed by Perdew and Wang[9] was employed for the exchange and correlation functional. The core-electron interaction was described by the effective core potentials. The wave functions were expanded in terms of a double-numerical basis set with a polarization d-function on all non-hydrogen atoms. The global orbital cutoff was 5.5Å. A three-layer slab with a (3×3) unit cell was used to model the doped Cu(111) surface, which has been shown to be thick enough to well describe the CO_2 hydrogenation on the Cu surfaces. In addition, the surface segregation was not considered in the present calculation. It has been shown that among all the dopants, Pd, Pt and Au prefer to stay in the surface of Cu(111), while Ni and Rh favor the bulk[92]. However, according to the experiments by Chorkendorff et al. [69-71], the active adsorbates, such as CO, are able to pull the Ni atom out to the surface under CH_3OH synthesis conditions. Therefore, the segregation of Ni and Rh into the bulk was not included in this study. Only atoms on the top layer were allowed to relax while the bottom two layers of atoms were fixed in their optimized bulk positions. One surface Cu atom was substituted by a dopant (Ni, Pd, Pt, Rh, Au) atom in each unit cell, corresponding to a dopant coverage of 1/9ML. The transition state (TS) was located by synchronous transit methods [42]. The Linear Synchronous Transit (LST) was conducted to bracket the maximum between the reactants and products, followed by repeated conjugate gradient minimizations and the Quadratic Synchronous Transit (QST) maximizations until a transition state was located. The convergence thresholds were set as that the root mean square (rms) forces on the atoms were smaller than 0.002 Ha/Å. Such methods yield results close to those obtained by eigenvector following methods. The KMC simulation is conducted with Kinetix, a software recently implemented in Material Studio 5.0[93].

4.3. Results and discussion

In the present study, DFT calculations were first performed to determine the intermediates and transition states (TS) for CH_3OH synthesis from CO_2 and H_2 via both the formate and the RWGS + CO-Hydro pathways. Previous experiments[8,18-20] observed a large amount of HCOO produced on Cu nanoparticles and surfaces during CH_3OH synthesis reaction. Our previous DFT studies also showed that HCOO formation was promoted by the low-coordinates sites present in the Cu nanoparticles with an activation barrier as low as +0.14eV.[8] Although our calculations show the activated formation of HCOO on Cu(111), the barrier seems to be readily overcome under the experimental conditions associated with high pressures and temperatures according to the experiments.[7-9,23] Therefore, it is reasonable to conclude that HCOO formation on Cu catalysts is facile and methanol synthesis is hindered by some other sequential steps. In this study, we used the metal-doped Cu(111) surfaces as a simplified model to study the promoting effect of alloy on the more difficult steps during the reaction. Therefore, we skipped this step on the metal-doped Cu(111) surfaces and focused on the subsequent hydrogenations of HCOO to CH_3OH. According to the experiments[8,26], CO is another main product under reaction conditions. Since Cu(111) is catalytically active towards the conversion of CO_2 to CO via the RWGS reaction,[8] only the subsequent steps associated with the direct CO hydrogenation to CH_3OH were considered here. In the following discussion, the results on doped surfaces will be compared to those on Cu(111), which have been partly reported in our previous study[8].

4.3.1. Reaction mechanism

4.3.1.1. Ni/Cu(111)

The potential energy diagrams for CH_3OH synthesis on Ni/Cu(111) via the formate and RWGS+CO-Hydro pathways are shown in Figure 4.2 and the geometries of the reaction intermediates and TS are displayed in Figure 4.3. Our calculations show that along both pathways, the presence of Ni alters the energetics of the intermediates and TS involved in the case of Cu(111). Following the formate pathway, HCOO binds to Ni/Cu(111) in the bidentate configuration with one O residing on top of a Ni atom while the other one resides on top of a Cu atom (η^2-O, O, Figure 4.3). The adsorption configuration is similar to that on Cu(111), yet the binding of HCOO on Ni/Cu(111) is 0.37eV more stronger due to the direct Ni-O interaction. As a result, the activation barrier (E_a) of HCOO hydrogenation ($HCOO^* + 1/2H_2 \rightarrow H_2COO^*$, $E_a = +1.39$eV, where "X*" represents an adsorbed species on the surface) is higher than that of Cu(111) by 0.30eV. The product H_2COO also anchors through the two oxygen atoms (η^2-O, O, Figure 4.3), with one O atom binding to the Cu-Cu bridge site and the other one binding to the Ni-Cu bridge site. For the dissociative hydrogenation of H_2COO ($H_2COO^* + 1/2H_2 +^* \rightarrow$

H_2CO*+ OH*) on Ni/Cu(111), E_a = +0.69eV, which is 0.91eV lower than the corresponding barrier on the Cu(111) surface.

For the CO hydrogenation pathway, our previous study[8] and the work from Mei et al.[35] have shown that CO prefers to desorb from Cu rather than to undergo further hydrogenation to HCO, which favors dissociation back to CO and H. Both steps hinder the CH_3OH synthesis from CO hydrogenation on Cu and experimentally, a large amount of CO was observed under CH_3OH synthesis conditions.[8] According to our present calculations, the doping of Ni helps to stabilize CO and improve the corresponding hydrogenation processes. CO binds Ni/Cu(111) on top of the Ni site (Figure 4.3), stronger than that on Cu(111) by 0.94eV. The hydrogenation of CO yields HCO (CO* + $1/2H_2 \rightarrow$ HCO*), which is an endothermic reaction (reaction energy, ΔE= +0.77eV) with E_a = +0.93eV (Figure 4.2). On Ni/Cu(111), CO hydrogenation is preferred over CO desorption since the hydrogenation barrier is 0.73eV lower than for the desorption due to the stronger CO binding. In addition, HCO binds on Ni/Cu(111) via the η^2-C, O configuration (Figure 4.3), which is 0.78eV more stable than that on Cu(111). The further hydrogenation of HCO to H_2CO (HCO* + $1/2H_2 \rightarrow H_2CO$*, E_a = +0.29eV) is energetically comparable to the HCO dissociation back to CO (HCO* +*$\rightarrow$ H* + CO*, E_a= +0.26eV).

H_2CO is produced by both H_2COO hydrogenation via the formate pathway, and HCO hydrogenation via the RWGS + CO-Hydro pathway. The subsequent hydrogenation of H_2CO to H_3CO (H_2CO* + $1/2H_2 \rightarrow H_3CO$*) is facile on Ni/Cu(111) with E_a as low as +0.19eV. Compared with that on Cu(111), H_2CO on Ni/Cu(111) is 0.56eV more stable, where the C atom directly interacts with Ni, and the O atom interacts with Cu (η^2-C, O,

Figure 4.3). Further hydrogenation of H_3CO results in the formation of CH_3OH ($H_3CO^* + 1/2H_2 \rightarrow CH_3OH^*$) ($\Delta E$= -0.11eV, E_a = +0.78eV), where CH_3OH binding to the Ni site through the O atom.

It is clear that the Ni sites on Ni/Cu(111) stabilize the O-containing intermediates and therefore lowers the activation barriers for most of the hydrogenation steps. Most importantly, Ni is able to significantly decrease the activation barrier for H_2COO hydrogenation, which is the rate-limiting step in the formate pathway. Following the RWGS + CO-Hydro pathway, Ni stabilizes CO on the surface and promotes the hydrogenation of CO to HCO. In both pathways, higher CH_3OH yield is expected on Ni/Cu(111) compared to Cu(111), which is consistent with the previous observations on Ni modified Cu catalysts.[69-71].

4.3.1.2. Pd/Cu(111)

For the formate pathway, both HCOO and H_2COO prefer to bind to Cu sites on Pd/Cu(111) and the adsorption configuration is the same as on Cu(111). The stability of HCOO and H_2COO on Pd/Cu(111) is therefore comparable to Cu(111). Compared to Cu(111), Pd/Cu(111) does not promote the hydrogenation of HCOO (ΔE= +0.72eV, E_a = +1.45eV). However, the H_2COO hydrogenation is easier (ΔE= -0.13eV, E_a = +1.36eV) with a barrier 0.23eV lower than that on Cu(111).

For the CO hydrogenation pathway, CO binds on top of a Pd site and the binding is 0.49eV more stable on Pd/Cu(111) than that on Cu(111). However, the barrier for CO hydrogenation to HCO (E_a = +1.25eV), which binds on top of Pd through a C atom (η^1-C), is comparable to that of CO desorption (E_a = +1.21eV). The further hydrogenation of HCO on Pd/Cu(111) is almost barrierless (ΔE= -0.24eV, E_a = +0.01 eV). Different from the case of Cu(111) and Ni/Cu(111), the barrier for HCO hydrogenation on Pd/Cu(111) is 0.65eV lower than that of HCO dissociation.

Again, the hydrogenations of both H_2COO and HCO are predicted to yield H_2CO on Pd/Cu(111). The binding configuration of H_2CO is the same as that on Ni/Cu(111). Due to the relatively stronger binding of H_2CO by 0.21eV, the subsequent hydrogenation (ΔE= -0.86 eV, E_a = +0.42 eV) is easier on Pd/Cu(111) than that on Cu(111). The product H_3CO, which binds to Cu three-fold hollow sites, is further hydrogenated to CH_3OH (ΔE= -0.27 eV, E_a= +0.70eV).

Following the formate pathway, Pd/Cu(111) does not lower the HCOO hydrogenation barrier even though the barrier for H_2COO hydrogenation is slightly lower. However, via the CO hydrogenation pathway, Pd/Cu(111) promotes the HCO hydrogenation and therefore higher CH_3OH yield is expected.

4.3.1.3. Pt/Cu(111)

The binding configurations of the intermediates on Pt/Cu(111) are the same as those on Pd/Cu(111). In addition, the energetics are also similar as those of Pd/Cu(111). In the formate pathway, the barrier for the hydrogenation of HCOO and H_2COO on Pd/Cu(111) is 0.33 eV and 0.28 eV lower respectively than that on Cu(111).

In the CO hydrogenation pathway, CO hydrogenation to HCO (ΔE= +0.45 eV, E_a = +1.21 eV) is preferred over CO desorption (E_a = +1.38 eV) due to the strong binding of CO on top of a Pt site. Moreover, the HCO hydrogenation (E_a = +0.72 eV) is energetically comparable to the HCO dissociation (E_a = +0.76 eV).

The corresponding barrier for H_2CO hydrogenation to H_3CO is 0.59eV lower than that on Cu(111). The H_3CO hydrogenation to CH_3OH is also easier on Pt/Cu(111) than that on Cu(111) with Ea = +0.47eV.

Pt/Cu(111) seems to promote the CH_3OH production via the formate pathway by lowering the activation barriers of HCOO and H_2COO hydrogenation. In addition, Pt/Cu(111) is able to stabilize CO and prevent the CO desorption, which allows for CO hydrogenation. Therefore, the CH_3OH production via RWGS + CO-Hydro pathway should also be facilitated by doping Pt.

4.3.1.4. Rh/Cu(111)

The reaction intermediates involved in both pathways bind to Rh/Cu(111) in the same configuration as those to Ni/Cu(111). Similar to Ni/Cu(111), the hydrogenation of HCOO (ΔE= +0.76 eV, E_a = +1.43 eV) in the formate pathway on Rh/Cu(111) is more difficult than that on Cu(111). However, E_a for the hydrogenation of H_2COO is lowered to +1.28eV, which is 0.32eV lower than that on Cu(111). For the CO hydrogenation pathway, CO strongly binds on top of a Rh atom with a binding energy of -2.13eV, which effectively prevents the CO desorption. However, the strong CO-Rh interaction also hinders the CO hydrogenation, where E_a for HCO dissociation ($HCO^* + * \rightarrow CO^* + H^*$, E_a = +0.08eV) is lower than those for the CO hydrogenation to HCO (E_a = +0.90eV) and HCO hydrogenation to H_2CO (E_a = +0.36eV). That is, energetically CO seems to be a very stable intermediate during the reaction on Rh/Cu(111). The subsequent hydrogenations of H_2CO (ΔE= -0.53eV, E_a = +0.13eV) and H_3CO (ΔE= -0.37eV, E_a = +0.19eV) are both facile on Rh/Cu(111).

Rh/Cu(111) does lower the barriers for the hydrogenations of most intermediates except for HCOO. CO is stabilized on Rh/Cu(111) with the strongest binding energy among the studies surfaces. However, it seems that CO-Rh interaction is too strong to favor the further CO hydrogenation to H_3COH.

4.3.1.5. Au/Cu(111)

On Au/Cu(111), all the intermediates prefer to adsorb on the Cu sites instead of interacting with Au. Therefore, the number of active sites decreases by doping Au (ensemble effect)[94], which is not surprising since Au is less active than Cu. The intermediate configurations are the same as those on Cu(111). The binding of the intermediates on Au/Cu(111) is either comparable to or even weaker than that on Cu(111) along both pathways due to the strain introduced by doping Au, which deactivates the Cu sites (ligand effect).[92,94] The hydrogenations of HCOO (ΔE= +0.66eV, E_a = +1.55eV) and H_2COO (ΔE= -0. 10eV, E_a = +1.65eV) on Au/Cu(111) are more difficult than those on Cu(111). CO binds to Au/Cu(111) with a binding energy of -0.63eV, which is 0.09eV lower than that to Cu(111). The further CO hydrogenation is not preferred since the barrier is 0.29eV higher than that of CO desorption. The energetics of HCO dissociating back to CO (ΔE= -0.54eV, E_a = +0.38eV) are comparable to that of HCO hydrogenation to H_2CO (ΔE= -0.57eV, E_a = +0.43eV). Any H_2CO produced would be further hydrogenated to H_3CO (ΔE= -1.03eV, E_a = +0.46eV) and finally to CH_3OH (ΔE= -0.29eV, E_a = +1.41eV).

According to the calculated energetics, Au/Cu(111) would appear to be a poorer catalyst than Cu(111). The intermediates bind more weakly on Au/Cu(111), and it neither facilitates the hydrogenation steps, nor does it stabilize CO or HCO. Such results are expected since Au is inert and the strain introduced by doping Au deactivates the Cu atoms on the surface[92].

4.3.2. KMC simulations and the sensitivity analysis

In previous sections, the energetics for CH_3OH synthesis along different pathways on doped Cu(111) surfaces have been addressed, which provide a better understanding of the doping effects on the thermodynamics. In this section, we will investigate how the energetics would affect the kinetics of the reaction. How do the different dopants affect the preference of the reaction pathways and the CH_3OH yield? What are the key kinetic parameters or descriptors, being able to describe the catalytic activity of Cu-based catalysts towards CH_3OH synthesis? To answer these questions, a KMC calculation and a sensitivity analysis were conducted.

4.3.2.1. KMC simulations

The elementary steps included in the KMC simulation are summarized in Table 4.1, where both formate and the RWGS + CO-Hydro pathways are included and the coadsorption of the reactants for each step is considered. For the conversion of CO_2 to CO via the RWGS reaction on all the surfaces, the reaction energies and activation barriers on Cu(111) calculated by Mavrikakis et al[52] were adopted. In addition, the HCO dehydrogenation (R6), the reverse reaction of R5, was also included explicitly, because our previous studies have shown the significant effect of competition between HCO dissociation and HCO hydrogenation on the methanol synthesis on Cu.[8] For all the surface reactions, the prefactor $1.0\times10^{13}s^{-1}$ was used. In the KMC simulations, the reactions conditions were chosen to be T=650K with P_{H2}/P_{CO2}=9:1. In this study, the reaction rate of each elementary step was calculated by averaging the rate during the simulation time (60 seconds).

To estimate the catalytic activity towards CH_3OH synthesis, the reaction rate of CH_3OH desorption (R13, Table 4.1) was calculated. Among all the doped surfaces studied here, there is an increase of CH_3OH synthesis reactivity in the sequence: Au/Cu(111) < Cu(111) < Pd/Cu(111) < Rh/Cu(111) < Pt/Cu(111) < Ni/Cu(111) (Figure 4.4). Au/Cu(111) is worse than Cu(111) since Au is not an active site in the reaction. Doping Au deactivates the Cu sites on Au/Cu(111) due to both ensemble and ligand effects (see Section III.1.5). However, Pd, Rh, Pt as well as Ni promote CH_3OH production on Cu(111) . Under our reaction conditions, the CH_3OH production rates on the doped surface are 2.5, 4.2, 5.2 and 7.5 times of that on Cu(111), respectively.

The KMC simulations can also help in revealing the preference of reaction pathway. Both the formate and the RWGS + CO-Hydro pathways go through the same intermediate H_2CO to the final product CH_3OH. Therefore, in our simulations, the reaction rates of H_2CO formation from R7 and R10 in Table 4.1 are considered to represent the CH_3OH yield from the RWGS + CO-Hydro pathway and the formate pathway, respectively. Figure 4.5 shows the ratio of CH_3OH production rate from the two different pathways on all the surfaces studied. Doped with inert Au, as demonstrated in Section III.1, all the reactions take place at the Cu sites of Au/Cu(111). In both Au/Cu(111) and Cu(111), the formate pathway dominates the reaction, though the Cu sites are deactivated by doping Au. By contrast, the RWGS + CO-Hydro pathway plays a more important role on Pd, Rh, Pt and Ni doped Cu(111) surfaces, even though both pathways contribute to the overall production of CH_3OH. The CH_3OH yield via the

RWGS + CO-Hydro pathway is 1.1 for Pd/Cu(111), 2.9 for Rh/Cu(111), 2.1 for Pt/Cu(111) and 1.3 for Ni/Cu(111) times of that via the formate pathway. The Cu(111) surfaces doped with the active metals are able to stabilize the surface adsorbates, in particular, CO and HCO, and therefore promote the CH_3OH synthesis via the RWGS + CO-Hydro pathway. Our results imply that accelerating the conversion of CO and HCO to CH_3OH is the more effective way to improve CH_3OH synthesis on Cu-based catalysts, as the RWGS is a faster reaction than the CH_3OH synthesis via the formate pathway.[8]

4.3.2.2. Sensitivity analysis

Effort was also devoted to identifying the key factors that control the CH_3OH yield via different pathways. On the basis of the KMC simulation on Cu(111), a sensitivity analysis[58] was carried out, where the activation barrier of each elementary step was varied arbitrarily and independently. Namely, the activation barrier of only one step is changed while keeping all the others the same. In this way the sensitivity of the CH_3OH production rate to each activated elementary step can be evaluated. Among all the elementary steps which have been tested, the CH_3OH production rate is most sensitive to the H_2COO hydrogenation (R10), the CO desorption (R4) and the CO hydrogenation (R5).

As shown in Figure 4.6, the CH_3OH production can be improved by decreasing the activation barrier of H_2COO hydrogenation. Meanwhile, the CH_3OH contributed from the formate pathway increases accordingly (Figure 4.7). Lowering the activation barrier of the rate-limiting H_2COO hydrogenation promotes the CH_3OH production via the formate pathway and therefore increases the overall yield. The results agree well with our finding in the doped catalysts. As seen in Figure 4.8, the doped surface with a lower

H_2COO hydrogenation barrier exhibits a higher CH_3OH production rate. The H_2COO hydrogenation barrier can thus be considered as one of the descriptors to scale the catalytic activity of CH_3OH synthesis on Cu-based catalysts.

It is also shown in Figure 4.6 that the catalytic activity strongly depends on the activation barrier of CO desorption and hydrogenation. Upon increasing the barrier for CO desorption or decreasing the barrier for CO hydrogenation, the rate of CH_3OH production increases and the contribution from the RWGS + CO-Hydro pathway is correspondingly larger (Figure 4.7). This means that a stronger CO binding or a lower CO hydrogenation barrier enables faster CH_3OH formation kinetics via the RWGS + CO-Hydro pathway. However, among all the doped surfaces considered in this study, the CO hydrogenation barrier does not differ significantly, varying from +0.92eV to +1.25eV. In contrast, the dopants do change the CO binding energy considerably. Figure 4.9 shows the relationship between the CO binding energy and the relative CH_3OH production rate on the doped surfaces. Upon going from Ni/Cu(111) to Au/Cu(111) in Figure 4.9, the CH_3OH production rate decreases along with the decrease in CO binding energy. In the case of Rh/Cu(111), it does not show the highest CH_3OH production rate even though it has the strongest CO binding. As observed in the KMC simulation, the strong CO-Rh interaction effectively prevents CO desorption; however, it also hinders the further CO hydrogenation to CH_3OH (see Section III.1.4). Our KMC results show a buildup of CO on Rh/Cu(111) during the reaction, which is not seen on any other alloy surface in this study. We therefore attribute the decline of activity to CO poisoning the Rh/Cu(111) surface. If CO binding to the surface is too strong, the number of available sites for the reactions decreases. To verify this argument, we further increased the CO binding energy on Cu(111) by 1.5eV, while keeping all the other barriers the same. A decrease in the CH_3OH production activity, rather than a further increase as might be expected from the trend shown in Figure 4.6, was observed along with an increase of surface CO coverage. Hence, the CO binding energy can be considered as another descriptor to scale the catalytic activity of CH_3OH synthesis on Cu-based catalysts. A good Cu-based catalyst should have a moderate CO binding energy, i.e., strong enough to prevent CO desorption and weak enough to avoid poisoning of active sites.

4.4. Conclusions

A combined DFT and KMC study was carried out to investigate the effects of metal dopants on the catalytic performance of the Cu(111) surface towards the CH_3OH synthesis via CO_2 hydrogenation. Both the formate pathway and the RWGS + CO-Hydro pathway were considered in this study. Our results show that Ni, Pt, Pd as well as Rh promote the CH_3OH synthesis reaction while Au deactivates the reaction. The CH_3OH production rate was found to increase in the sequence: Au/Cu(111) < Cu(111) < Pd/Cu(111) < Rh/Cu(111) < Pt/Cu(111) < Ni/Cu(111).

The KMC simulations also help in revealing the preferred reaction pathway. On Cu(111) and Au/Cu(111), the formate pathway dominates the CH_3OH production. However, on Pd, Rh, Pt and Ni doped Cu(111) surfaces, the RWGS+CO-Hydro pathway plays a more important role even though both pathways contribute to the production of CH_3OH. Doping these active metals stabilizes the surface intermediates, in particular, CO and HCO, and therefore promotes CH_3OH synthesis via the RWGS + CO-Hydro pathway.

On the basis of the sensitivity analysis, two descriptors are proposed to describe the catalytic activity of Cu-based catalysts for CH_3OH synthesis from CO_2 hydrogenation. One is the activation barrier for H_2COO hydrogenation. With a lower barrier for H_2COO hydrogenation, the catalyst should exhibit better activity towards the CH_3OH synthesis reaction. The other is the CO binding energy. On one hand, the CO should bind to the catalyst strong enough so that CO can be hydrogenated to CH_3OH before desorption; on the other hand, it should be weak enough so that CO poisoning on the active sites can be avoided. Therefore, an ideal Cu-based catalyst towards CH_3OH synthesis should be able to hydrogenate H_2COO easily and bond CO moderately, being strong enough to favor the desired CO hydrogenation rather than CO desorption, but weak enough to prevent CO poisoning. In this way, the CH_3OH yield via both the formate pathway and the RWGS+CO-Hydro pathway can be facilitated.

Elementary Steps	Cu(111)		Ni_Cu(111)		Pd_Cu(111)		Pt_Cu(111)		Rh_Cu(111)		Au_Cu(111)	
	E_a	ΔE	E_a	ΔE	E_a	ΔE	E_a	ΔE	E_a	ΔE	E_a	ΔE
R1. H_2+2*→2H*	0.93	-0.30	0.93	-0.30	0.93	-0.30	0.93	-0.30	0.93	-0.30	0.93	-0.30
R2. H*+CO_2→HOCO*	1.80	0.39	1.80	0.39	1.80	0.39	1.80	0.39	1.80	0.39	1.80	0.39
R3. HOCO*+*→CO*+OH*	0.59	-0.02	0.59	-0.02	0.59	-0.02	0.59	-0.02	0.59	-0.02	0.59	-0.02
R4. CO*→CO+*	0.72	0.72	1.66	1.66	1.21	1.21	1.38	1.38	2.13	2.13	0.63	0.63
R5. CO*+H*→HCO*+*	1.00	0.69	1.09	0.93	1.25	0.58	1.22	0.46	1.05	0.97	1.00	0.62
R6. HCO*+*→CO*+H*	0.31	-0.69	0.16	-0.93	0.67	-0.58	0.76	-0.46	0.08	-0.97	0.38	-0.62
R7. HCO*+H*→H_2CO*+*	0.46	-0.45	0.33	-0.18	0.01	-0.24	0.70	-0.04	0.54	0.26	0.47	-0.52
R8. H*+*+CO_2→HCOO*	1.22	-0.16	1.22	-0.16	1.22	-0.16	1.22	-0.16	1.22	-0.16	1.22	-0.16
R9. HCOO*+H*→H_2COO*+*	1.20	0.70	1.50	0.86	1.64	0.91	0.96	0.92	1.63	0.99	1.58	0.68
R10.H_2COO*+H*→H_2CO*+OH*	1.64	-0.10	0.83	-0.09	1.57	0.08	1.53	-0.01	1.60	0.10	1.68	-0.08
R11. H_2CO*+H*→H_3CO*+*	0.77	-1.08	0.31	-0.69	0.52	-0.75	0.14	-0.67	0.63	-0.03	0.54	-0.95
R12. H_3CO*+H*→CH_3OH*+*	1.25	-0.06	1.00	0.12	0.79	-0.19	0.55	-0.26	0.55	-0.01	1.37	-0.25
R13. CH_3OH*→CH_3OH+*	0.27	0.27	0.46	0.46	0.30	0.30	0.31	0.31	0.44	0.44	0.28	0.28
R14. H*+OH*→ H_2O*+*	1.35	-0.01	1.35	-0.01	1.35	-0.01	1.35	-0.01	1.35	-0.01	1.35	-0.01
R15. H_2O*→H_2O+*	0.18	0.18	0.18	0.18	0.18	0.18	0.18	0.18	0.18	0.18	0.18	0.18

Table 4.1 The elementary steps included in the KMC simulations. The reaction energies (ΔE) and activation barriers (Ea) are reported in the unit of eV.

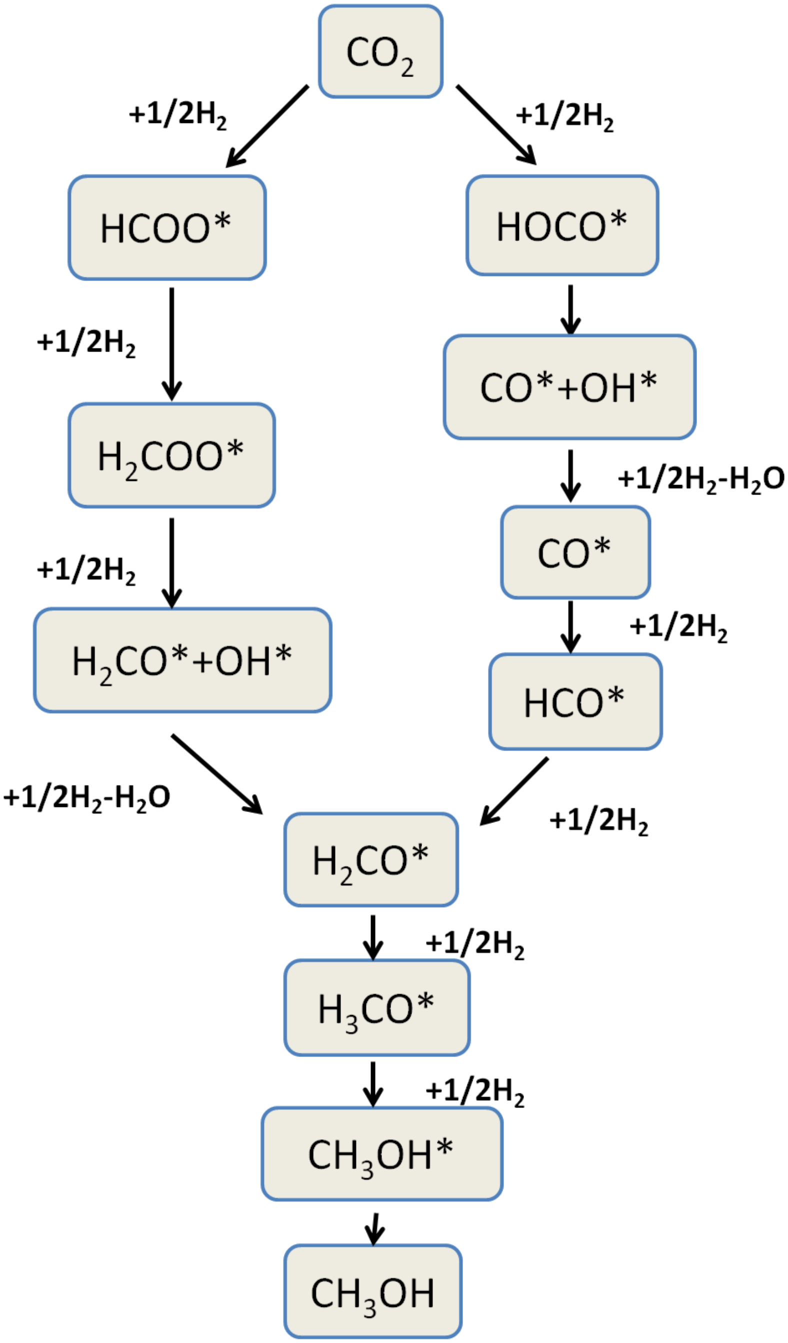

Figure 4.1. Reaction network scheme of formate pathway and RWGS+CO-Hydro pathway

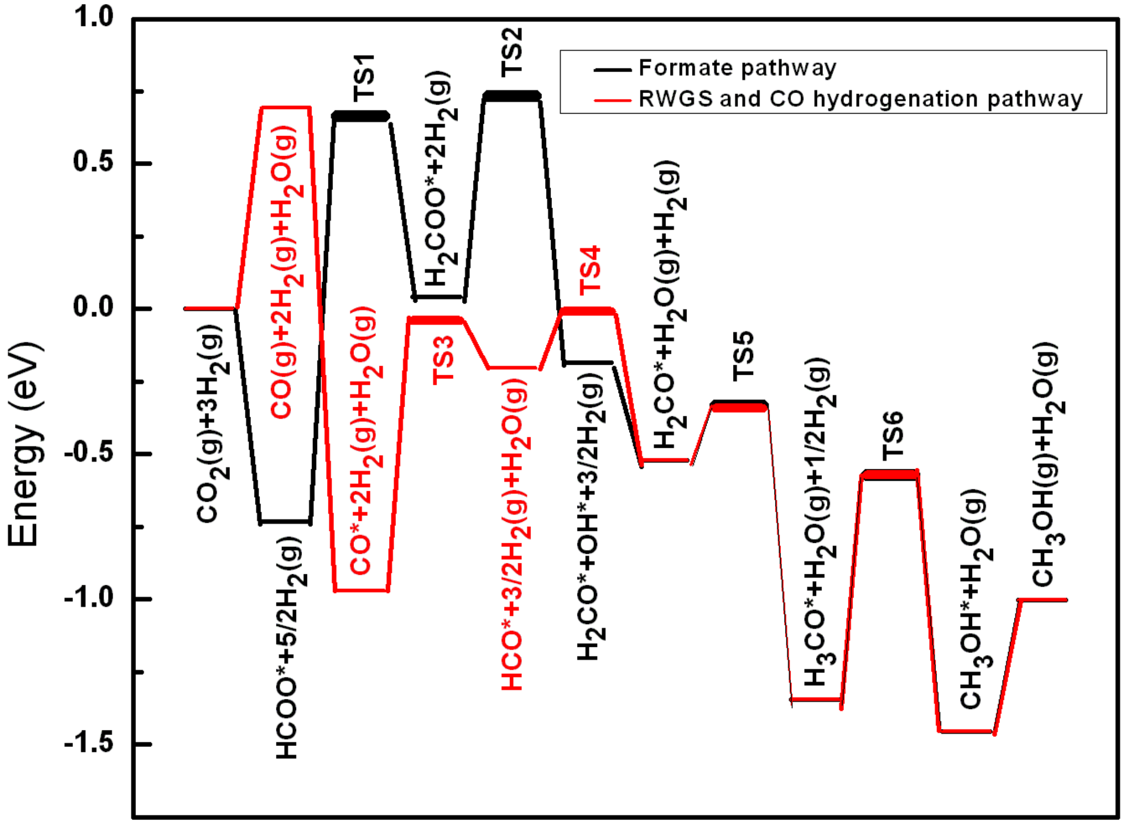

Figure 4.2. Potential energy diagrams for the CH_3OH synthesis reaction via the formate and RWGS + CO-Hydro pathways on the Ni/Cu(111) surface. The thin bars represent the energy for the reactants, intermediates and products. The thick bars stand for the energy for the transition states (TS).

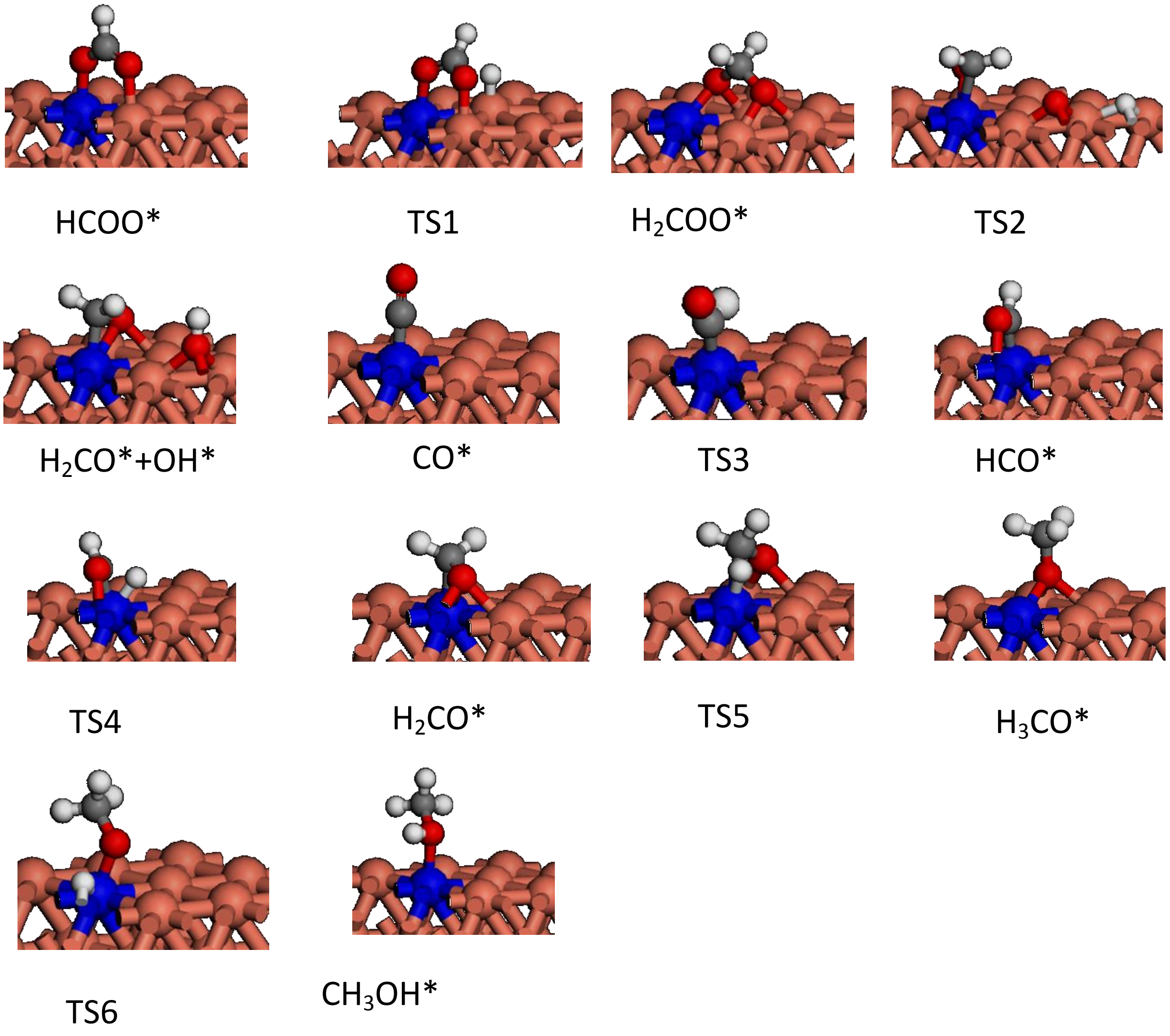

$HCOO^*$ TS1 H_2COO^* TS2

$H_2CO^*+OH^*$ CO^* TS3 HCO^*

TS4 H_2CO^* TS5 H_3CO^*

TS6 CH_3OH^*

Figure 4.3. Structures of the intermediates and TS involved in the CH_3OH synthesis reaction on the Ni/Cu(111) surface (Big brown: Cu; big blue: Ni; small white: H; small red: O; small grey: C). The corresponding energy of each configuration was shown in Figure 4.2.

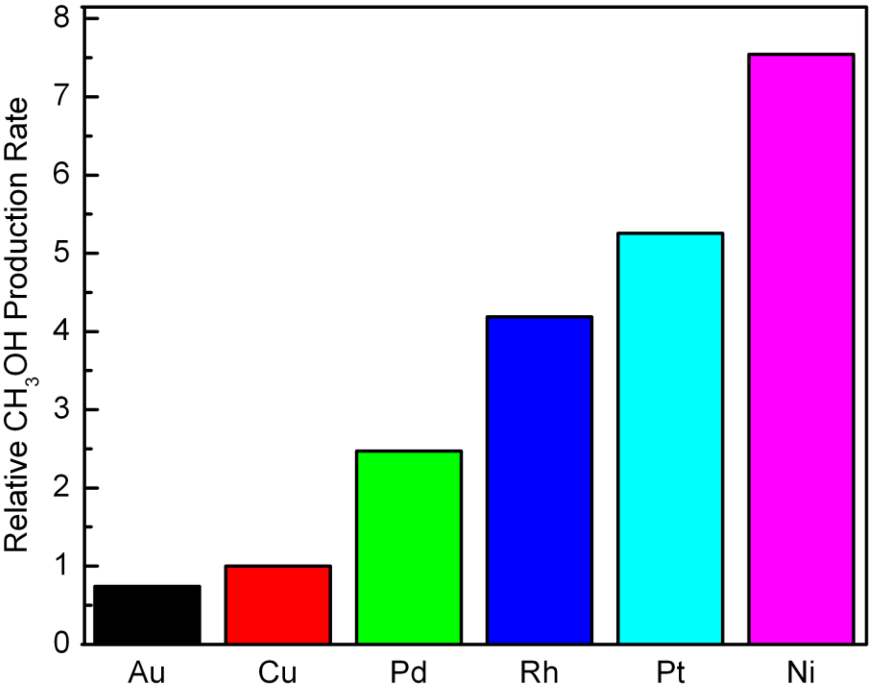

Figure 4.4 The relative rate of CH_3OH production with respect to Cu(111) on the doped surfaces.

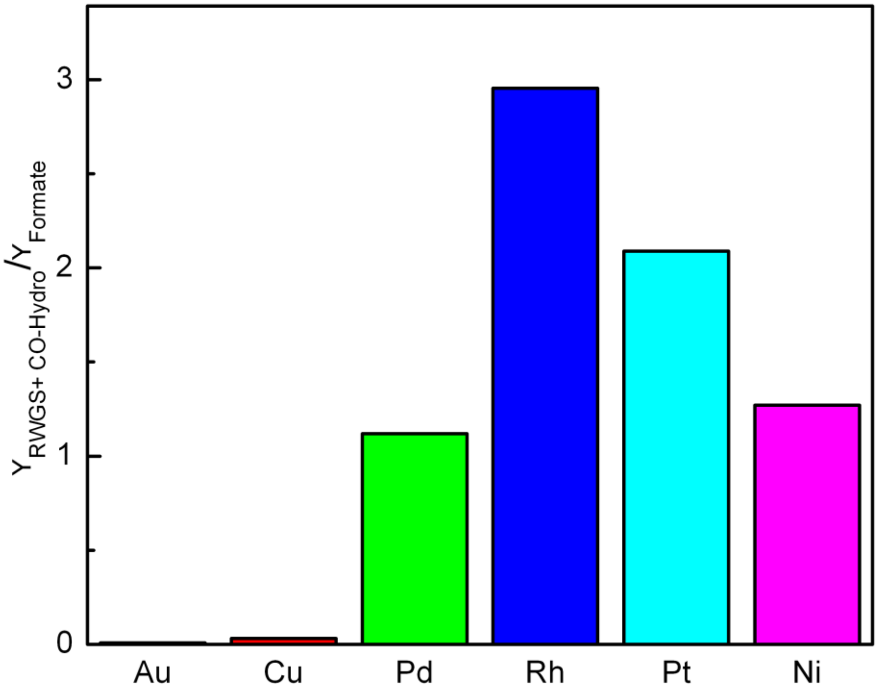

Figure 4.5. The ratio of CH_3OH production rate via RWGS + CO-Hydro pathway ($Y_{RWGS+CO-Hydro}$) to that via formate pathway ($Y_{Formate}$) on Cu(111) and the doped Cu(111) surfaces.

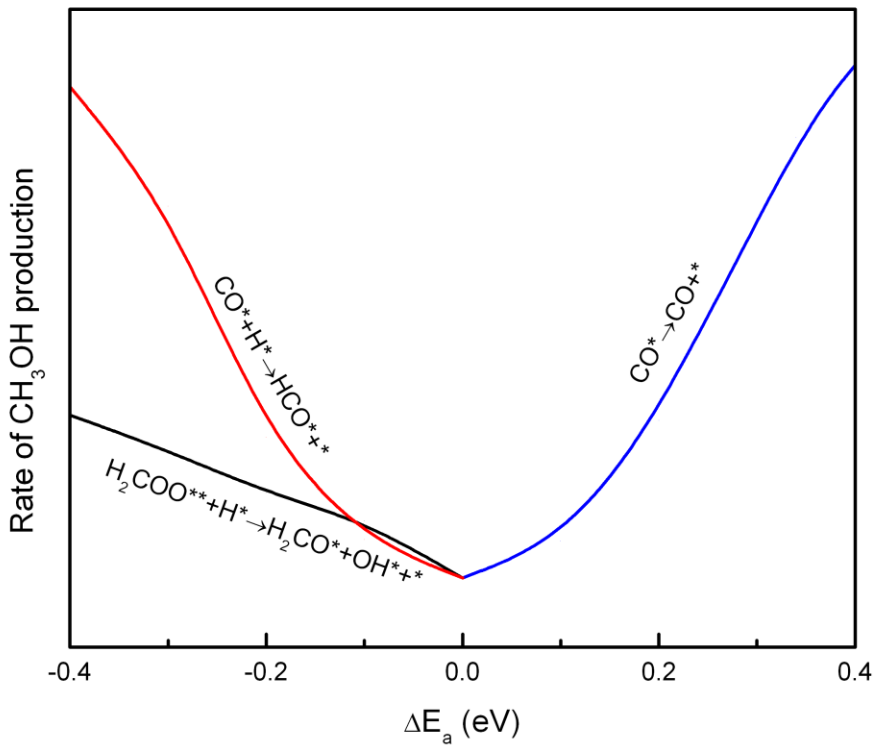

Figure 4.6 Sensitivity of CH_3OH production rate on Cu(111) to variation in activation barriers for $H_2COO^{**} + H^* \rightarrow H_2CO^* + OH^* + *$ (R10), $CO^* \rightarrow CO + *$ (R4) and $CO^* + H^* \rightarrow HCO^* + *$ (R5), respectively. Positive ΔE_a indicates the increase of the barrier from the original value on Cu(111) while negative ΔE_a indicates the decrease of the barrier from the original value.

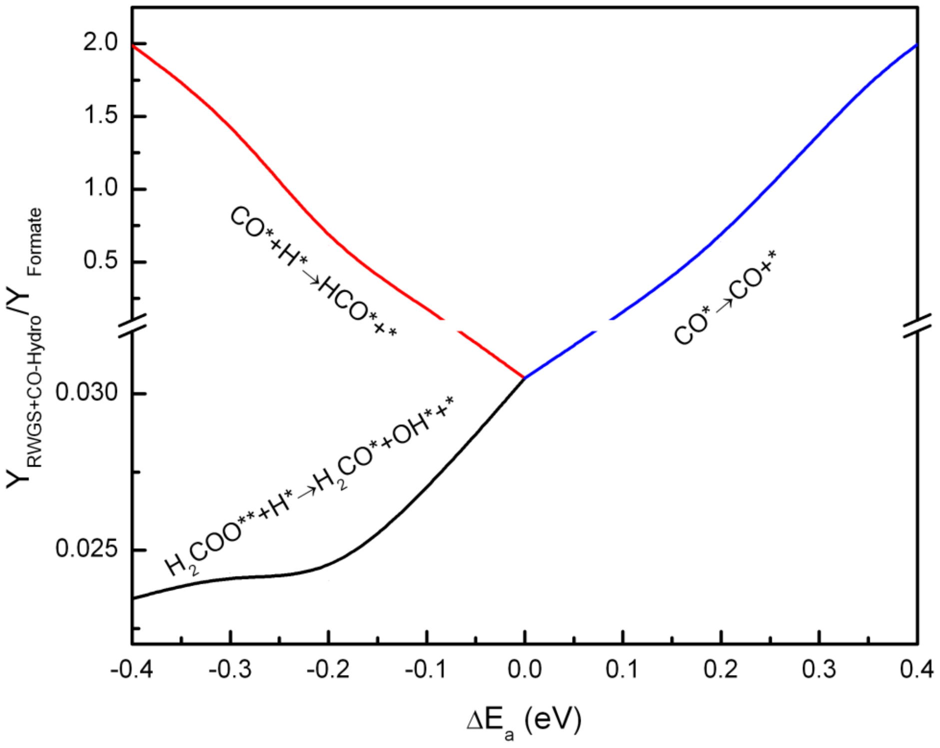

Figure 4.7 Sensitivity of the relative contribution of CH_3OH from the RWGS+CO-Hydro pathway and the formate pathway on Cu(111) to variation in reaction barriers for $H_2COO^{**} + H^* \rightarrow H_2CO^* + OH^* + {}^*$ (R10), $CO^* + H^* \rightarrow HCO^* + {}^*$ (R5) and $CO^* \rightarrow CO + {}^*$ (R4), respectively. Positive ΔE_a indicates the increase of the barrier from the original value on Cu(111) while negative ΔE_a indicates the decrease of the barrier from the original value.

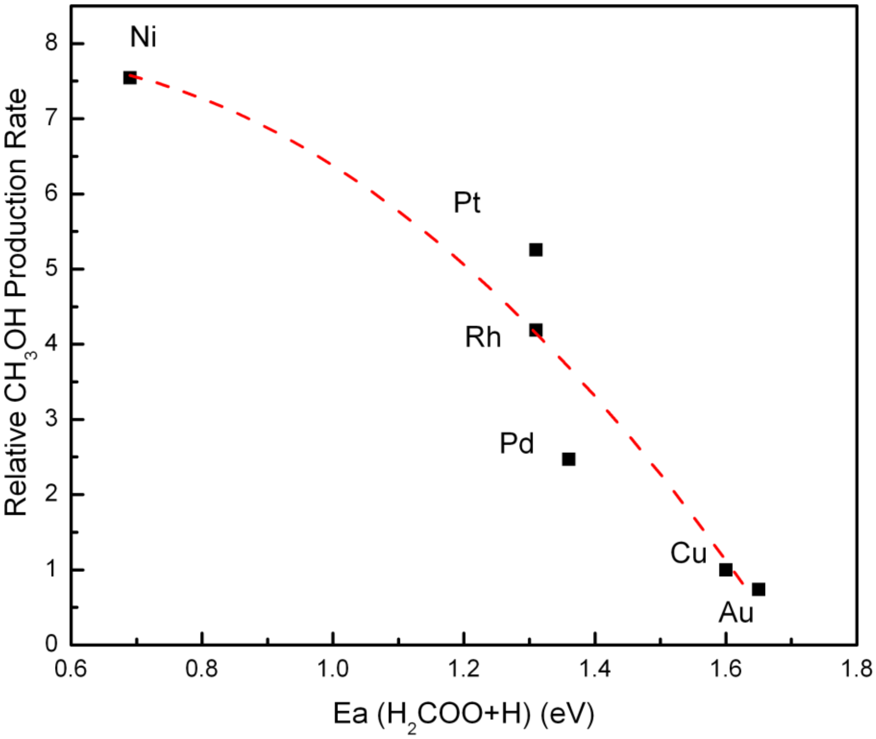

Figure 4.8. The relationship between the activation barrier of $H_2COO^{**} + H^* \rightarrow H_2CO^* + OH^* + *$ (R10) and the relative rate of CH_3OH production with respect to Cu(111) on the doped surfaces.

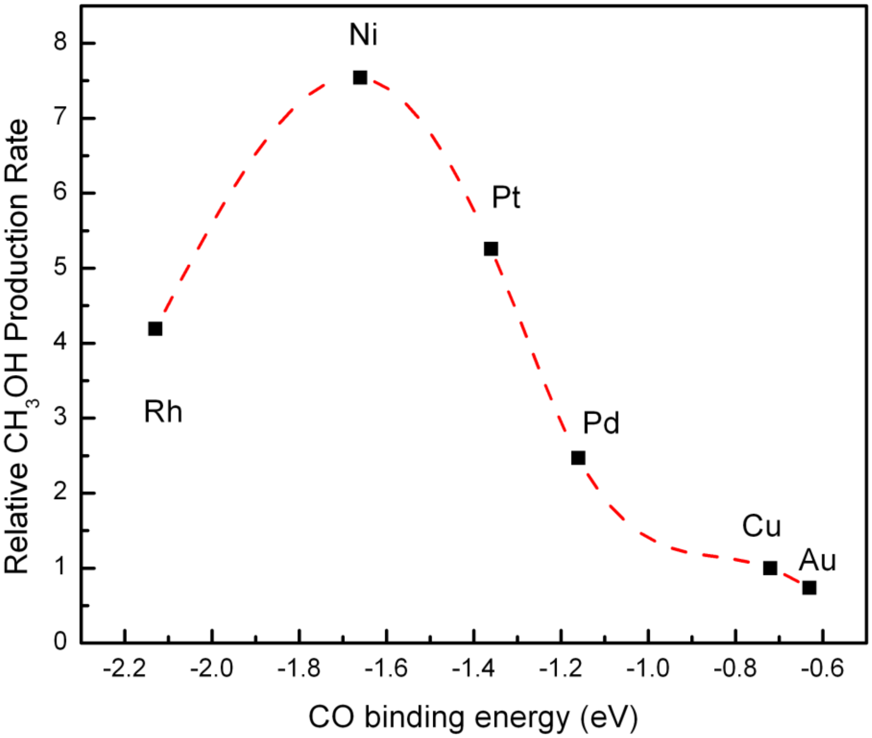

Figure 4.9 The relationship between the CO binding energy and the relative rate of CH_3OH production with respect to Cu(111) on the doped surfaces.

Chapter 5. Theoretical study of methanol synthesis from CO_2 hydrogenation on inverse catalysts: metal oxides supported on Cu(111)

5.1. Introduction

Different metal oxides, e.g. ZnO[8,18,32,89-91], ZrO_2[28], Al_2O_3[95] and SiO_2[24,28,95-99], have been used as the support in Cu-based catalysts for the methanol synthesis reaction. The activity of the catalysts can be significantly affected by the supports. Even though extensive experimental efforts have been devoted to understanding such a support effect, a fundamental understanding is still missing due to the complexity of the catalyst components and structures.

Some theoretical studies have been reported that investigate the reaction mechanisms at the Cu-oxide interface by identifying key intermediates, active sites and the dominant reaction pathway. Kakumoto et al. investigated the reaction mechanism on Cu/ZnO[100,101] and concluded that Cu^+ is the active site and the reaction is dominated by the formate pathway, where the reaction happens via intermediates HCOO, H_2COO, H_2CO and H_3CO. The RWGS+CO pathway, where CO_2 is converted into CO by the RWGS reaction followed by CO hydrogenation to CH_3OH is also possible on Cu/ZnO. But the active site for CO_2 conversion to CO is a Cu^0 site while Cu^+ is responsible for CO hydrogenation. More recently, Cu steps decorated with Zn atoms were proposed as the active site for the industrial Cu/ZnO/Al_2O_3 catalyst[102]. DFT results showed Zn promoted the reaction by strengthening the bonding of HCO, H_2CO and H_3CO due to its higher oxophilicity compared with that of Cu. Liu et al. studied the reaction at both the Cu/ZrO_2 interface[30] and O-rich Cu/ZrO_2 interface[103] by DFT-based KMC simulations. The study showed CO_2 can be dissociated into CO and O directly, followed by CO hydrogenation to methanol at the Cu/ZrO_2 interface. However, such a reaction will be deactivated fast due to the blocking of active sites by the oxidative species formed during the reaction. As a result, the O-rich Cu/ZrO_2 interface is the main active site, where the formate pathway is preferred. The reaction rate is controlled by CO_2 adsorption and H_2CO hydrogenation. The first step of CO_2 hydrogenation was also studied on Cu/Al_2O_3[104]. The complete mechanism is missing from the study but HCOO was proposed to be a key intermediate because HCOO is the product of CO_2 hydrogenation at the interface of Cu on both dry and hydroxlylated Al_2O_3.

So far there is not a systematic study trying to understand the effect of different metal-oxide supports on methanol synthesis activity. Some fundamental questions remain unanswered. Do the metal oxides act as bystanders and only serve as supports to disperse the Cu nanoparticles? Can the supports participate in the reaction by interacting with the reaction intermediates directly or affect the activity indirectly by interacting with Cu to modify the Cu oxidation state? What is the nature of the active site? In order to gain some insights into the support effect on methanol synthesis activity, a systematic DFT calculation on a series of Cu-metal oxide interface was carried out.

Inverse catalysts, i.e., metal oxide particles deposited on Cu(111), were used to model the interface structures in this study. They still allow the reactants to interact with the Cu-oxide interface sites as in the case of a conventional model catalyst. The chemical properties due to the electronic interactions between Cu and metal oxides can also be described in these model structures. Moreover, some inverse catalysts can even exhibit superior activity compared with their conventional counterparts due to the exposure of defect sites in the oxide nanoparticles[105]. In order to understand the size effect of metal oxide nanoparticles on the reaction mechanism and activity, both small metal oxide clusters and long metal oxide chain structures were included in this study. Small metal oxide clusters (Ti_3O_6, Zn_3O_3 and Mo_3O_9) were used to simulate the relatively small metal oxide nanoparticles. For comparison, long metal oxide chain structures

(TiO_2, ZnO and MoO_3) were also employed to simulate the interface between Cu and relatively large metal oxide nanoparticles with bulk-like structures. These models have been successfully employed in previous DFT studies in order to understand the reaction mechanisms of water-gas-shift (WGS) reaction at the Cu-oxide interface[106,107].

Both formate pathway and RWGS+CO-Hydro pathway were considered here. As shown in the previous chapter, methanol production on Cu-based catalysts can be promoted either by facilitating HCOO and H_2COO hydrogenation or improving CO hydrogenation. Therefore, in this chapter, we focus on the effect of the metal oxide support on these key steps instead of calculating the complete reaction mechanisms. The energetics of HCOO and H_2COO hydrogenation were considered in order to understand the effect of metal oxide support on the formate pathway. Similarly, the energetics of CO hydrogenation to H_2CO via HCO were calculated to elucidate the metal oxide contribution to the RWGS+CO-Hydro pathway.

5.2. Theoretical method

Spin-polarized DFT calculations were carried out using the Vienna *ab initio* simulation package (VASP)[108-110]. The generalized gradient approximation proposed by Perdew and Wang[9] was employed for the exchange and correlation functional. The plane-wave-pseudopotential with a cutoff energy of 400eV within the projector augmented wave (PAW)[111,112] method was used. Cu(3p,3d,4s), Zn(3p,3d,4s), Ti(3s,3p,3d,4s), Mo(4p,4d,5s), O(2s,2p), C(2s,2p) and H(1s) electrons were treated explicitly as valence states ,while the remaining electrons were kept frozen as core states. A Gaussian smearing method with an electronic temperature of $k_BT=0.05eV$ was performed to obtain faster convergence. The Cu(111) surface was modeled by a four-layer slab. The bottom two layers of atoms were fixed in their optimized bulk positions while the top two layers along with the metal oxides were allowed to relax. Brillouin-zone integrations were performed on a grid of 3×3×1 Monkhorst-Pack[11] special **k**-points.

A (5×5) unit cell was used to model metal oxide cluster/Cu(111) structures. The vacuum layer is 20Å thick. To describe the electronic structures of Ti in the Ti_3O_6 cluster correctly, the DFT+U[10] method was used. A U value of 4.5eV was applied to Ti[113,114], which gives a reasonable description of electronic structure of rutile TiO_2(110) surface.

For metal oxide chain/Cu(111) structures, a unit cell of (4×4), (5×4) and (4×3) with a 14Å thick vacuum layer was employed to describe ZnO/Cu(111), TiO_2/Cu(111) and MoO_3/Cu(111) respectively to minimize the interactions between the metal oxide chains.

5.3. Results and discussion

5.3.1. Geometries of metal oxide cluster/Cu(111) and metal oxide chain/Cu(111)

Figure 5.1 displays the most stable adsorption geometries of the metal oxide clusters supported on Cu(111). The cluster adsorption energy is defined as:

$$\Delta E_{ads}=E[cluster/Cu(111)]-E[Cu(111)]-E[cluster(g)]. \qquad Eq(5.1)$$

The adsorption geometries of Ti_3O_6 and Mo_3O_9 on Cu(111) are the same as described in the previous study[106]. The structure of the gas-phase Zn_3O_3 cluster is a six-membered ring of alternating Zn and O atoms[115]. After deposition, the Zn_3O_3 cluster is parallel to Cu(111) and ~2Å above the surface as seen in Figure 5.1(b). The binding energy of Zn_3O_3 on Cu(111) is -2.62eV.

The detailed structures of metal oxide chains (TiO_2, ZnO and MoO_3) deposited on Cu(111) were described in previous study[107]. The lattice constraint introduced by the metal oxide chain is small enough (<2%) to model the interface.

5.3.2. Formate pathway

5.3.2.1. Energetics of HCOO and H_2COO hydrogenation on metal oxide cluster/Cu(111)

The energetics of HCOO and H_2COO hydrogenation on metal oxide cluster/Cu(111) are shown in Figure 5.2(a). H adsorption energy is calculated by:

ΔE_{ads}=E[2H_cluster/Cu(111)]-E[cluster/Cu(111)]-E[H_2(g)]. Eq(5.3)

HCOO adsorption energy is expressed as:

ΔE_{ads}=E[2H_HCOO/Cu(111)]-E[2H/Cu(111)]-E[1/2H_2(g)]-E[CO_2(g)]. Eq(5.4)

H_2COO adsorption energy is expressed is defined as:

ΔE_{ads}=E[H_H_2COO/Cu(111)]-E[H/Cu(111)]-E[H_2(g)]-E[CO_2(g)]. Eq(5.5)

For comparison, the energetics on Cu(111) from our previous study[116] were also plotted. The H, HCOO and H_2COO adsorption energy on Cu(111) is -0.30eV, -0.32eV and +0.23eV respectively.

The adsorption geometries of the intermediates on Ti_3O_6/Cu(111) displays in Figure 5.3. The adsorption of H atoms disturbs the cluster structure. As seen in Figure 5.3(a), H atoms interact with O atoms of Ti_3O_6 so strongly (ΔE_{ads}=-1.49eV) that cluster tilts up and the O-Cu bonds break. HCOO binds to Cu(111) in a bidendate configuration (ΔE_{ads}=-1.05eV), with one atom interacting with Ti directly. The hydrogenation of HCOO to H_2COO (ΔE= +0.09eV) is less endothermic than that on Cu(111). The adsorption of produced H_2COO is also stabilized by Ti_3O_6 (ΔE_{ads}=-1.26eV). It tilts up to have one O atom interacting with Ti while the other one interacting with Cu (Figure 5.3(c)). Instead of being an exothermic step on Cu(111), the hydrogenation of H_2COO to H_2CO and OH is highly endothermic on Ti_3O_6/Cu(111) (ΔE=+1.10eV).

On Zn_3O_3/Cu(111), the adsorption of H on the clusters is the strongest among the systems considered here (ΔE_{ads}= -2.54eV). H atoms bind to ZnO so strongly that O atoms of the clusters are pulled up (Figure 5.4(a)). HCOO binds at the interface with one O atom bound to Zn and the other to Cu (ΔE_{ads}= -0.53eV, Figure 5.13(a)). The hydrogenation of HCOO is not facile (ΔE=+1.55eV). The produced H_2COO prefers to bind to an interface site also with a similar configuration with that on Ti_3O_6/Cu(111) ((ΔE_{ads}= -0.27eV). The further hydrogenation is also a mildly endothermic reaction (ΔE=+0.39eV).

On Mo_3O_9/Cu(111), all the intermediates stay on Cu(111) and away from Mo_3O_9 (Figure 5.5). Mo_3O_9 is inert and the resulted reaction energetics on Mo_3O_9/Cu(111) are similar to Cu(111).

5.3.3.2. Energetics of HCOO and H_2COO hydrogenation on metal oxide chain/Cu(111)

The energetics of HCOO and H_2COO hydrogenation on metal oxide chain/Cu(111) are shown in Figure 5.2(b). The adsorption geometries of the intermediates on TiO_2/Cu(111) are shown in Figure 5.6. The H atoms are strongly bound to those O sites of the cluster chain (ΔE_{ads}= -1.14eV). HCOO and H_2COO prefer to bind to Cu sites and not to interact with TiO_2 directly, which is different from those on Ti_3O_6/Cu(111). The bindings of HCOO (ΔE_{ads}= -0.51eV) and H_2COO (ΔE_{ads}= +0.21eV) on TiO_2/Cu(111) are slightly stronger than those on Cu(111) due to the hydrogen bond at the interface (Figure 5.6(a) and 5.6(b)). The hydrogenation of HCOO to H_2COO is an endothermic reaction (ΔE=+1.31eV). Instead of producing H_2CO and OH directly from H_2COO hydrogenation, it is likely that intermediate H_2COOH is the direct product of H_2COO hydrogenation because H_2COOH is more stable on TiO_2/Cu(111). Such stabilization is due to the interaction of H with the O site of TiO_2 via a hydrogen bond. H_2CO and OH will be produced from H_2COOH dissociation (ΔE=+0.72eV).

For ZnO/Cu(111), H atoms are bound to ZnO strongly (ΔE_{ads}= -2.31) such that the O atoms are pulled up significantly. HCOO prefers to adsorb on the ZnO chain structure (ΔE_{ads}= -0.66). The O atoms bind to the Zn sites with a bidentate configuration as seen in Figure 5.7(b).

The hydrogenation of HCOO would yield H_2COO, which is highly endothermic (ΔE=+2.12eV). H_2COO prefers to adsorb at the Cu-ZnO interface, with O atoms binding to Cu bridges sites and one of the O atoms interacting with Zn (ΔE_{ads}= +0.30eV). The H_2COOH structure observed on TiO_2/Cu(111) was not found here on ZnO/Cu(111). The hydrogenation of H_2COO would yield H_2CO and OH directly (ΔE=+0.30eV).

Different from the inert Mo_3O_9/Cu(111), MoO_3/Cu(111) is very active towards the adsorption of H(ΔE_{ads}= -1.35eV). The adsorption of H atoms on MoO_3 chain significantly distorts its structure (Figure 5.8(b)). Instead of a straight chain structure, MoO_3 sits on Cu(111) with a 'zig-zag' like geometry after H adsorption. However, MoO_3 still does not help stabilize HCOO and H_2COO. HCOO and H_2COO binds to Cu sites of MoO_3/Cu(111), with a similar binding energy as those on Cu(111). The hydrogenation of HCOO to H_2COO is mildly endothermic (ΔE=+0.68eV). The intermediate H_2COOH with a similar geometry as that on TiO_2/Cu(111) was found on MoO_3/Cu(111). The dissociation of H_2COOH would yield H_2CO and OH (ΔE=+0.61eV).

5.3.2.3. The effect of metal oxide on formate pathway

Among all the systems considered in this study, H is significantly stabilized by the both metal oxide cluster and metal oxide chain deposited on Cu(111) except for Mo_3O_9/Cu(111). The key step in formate pathway, i.e. H_2COO hydrogenation step is highly endothermic and a high barrier is expected as a result. This is because the binding of H to the oxide is so strong that it is difficult to break the O-H bond for the hydrogenation reaction. Therefore, the promotion of methanol production from formate pathway on metal oxide cluster/Cu(111) systems is limited. However, H can binds to Cu(111) as well under reaction condition. The hydrogenation by the H binding to Cu(111) will be investigated in the future study.

5.3.3. RWGS + CO-Hydro pathway

5.3.3.1. Energetics of CO hydrogenation on metal oxide cluster/Cu(111)

The energetics of CO hydrogenation to H_2CO on metal oxide cluster/Cu(111) were calculated and plotted in Figure 5.9(a). For comparison, the energetics on Cu(111) from our previous study[116] were also plotted. For Ti_3O_6/Cu(111), all the key intermediates i.e., CO, HCO and H_2CO, prefer to bind at the Ti_3O_6-Cu interface sites as seen in Figure 5.10. The C atom is bound at Cu sites while O interacts with a Ti atom from the cluster. CO is stabilized significantly (ΔE_{ads}=-1.60eV) at the interface site. The hydrogenation of CO to HCO is less endothermic (ΔE=+0.52eV) than that on Cu(111). The production of H_2CO from HCO hydrogenation is exothermic (ΔE= -0.16eV).

The adsorption geometries of the intermediates are shown in Figure 5.11 for Zn_3O_3/Cu(111). Unlike on Ti_3O_6/Cu(111), CO and HCO do not like to interact with the clusters for Zn_3O_3/Cu(111). CO and HCO adsorb on the Cu sites. The production of HCO is highly endothermic (ΔE=+1.89eV). The further HCO hydrogenation to H_2CO is exothermic (ΔE=-0.46eV). H_2CO is stabilized by the interface sites, where the O binds to both Cu and Zn while C is bound to Zn and O atoms simultaneously.

There is no promotion effect observed on Mo_3O_9/Cu(111). All the intermediates involved in the reaction only interact with Cu(111) and stay away from Mo_3O_9 as seen in Figure 5.12. As a result, the energetics of CO hydrogenation to H_2CO on Mo_3O_9/Cu(111) are very similar as that on Cu(111).

As described in the previous chapter, CO binding energy can be used as a descriptor to predict the methanol production activity from RWGS+CO-Hydro pathway. Therefore CO binding energies on these different systems are compared as seen in Figure 5.13(a). The relationship between CO binding and the methanol production activity obtained in last chapter is used here. The CO binding energy on Ti_3O_6/Cu(111) is within the optimum region. A significant promotion of methanol synthesis by Ti_3O_6 should be expected. The binding is moderate: strong enough to prevent CO desorption before hydrogenation and weak enough to prevent CO from poisoning the catalyst. However, no significant CO stabilization is observed for the rest of the systems.

5.3.3.2. Energetics of CO hydrogenation on metal oxide chain/Cu(111)

The energetics of CO hydrogenation to H_2CO on metal oxide chain/Cu(111) were calculated and shown in Figure 5.9(b). Similar as the case on Ti_3O_6/Cu(111), the key intermediates CO, HCO and H_2CO all prefer to adsorb at the Cu-TiO_2 interface on TiO_2/Cu(111) as seen in Figure 5.14. CO sits on a three-fold hollow site of Cu(111) while the O atoms interacting with Ti atom in the chain (Figure 5.14(a)). CO binds stronger on TiO_2/Cu(111) (ΔE=-0.86eV) than that on Cu(111). The hydrogenation of CO to HCO is endothermic (ΔE=+1.08eV). The produced HCO binds to the Cu-TiO_2 interface with the C atom interacting with Ti and O binding to the bridge site of Cu(111) (Figure 5.14(c)). The further hydrogenation of HCO to H_2CO is mildly endothermic (ΔE=+0.09eV). H_2CO also prefers the interface site, with a similar adsorption geometry as that of HCO (Figure 5.14(d)).

For ZnO/Cu(111), the optimized geometries of intermediates are shown in Figure 5.15. CO prefers to adsorb on Cu(111), away from the ZnO chain structure. HCO production from CO hydrogenation is also highly endothermic (ΔE=+1.56eV) on ZnO/Cu(111). HCO prefers to adsorb at the interface site. Zn stabilizes HCO by interacting with O directly. The further hydrogenation of HCO to H_2CO is an exothermic reaction (ΔE=-0.11eV). The resulted H_2CO

interacts with the O site of ZnO chain structure strongly to form a tilted-up ‘H_2COO’ like structure as seen in Figure 5.15(d).

Similar to the formate pathway, MoO_3 cannot help stabilize the O-containing intermediates. CO, HCO and H_2CO still prefer to bind to Cu(111) sites. The hydrogenation of CO to HCO is endothermic ($\Delta E=+0.48eV$) and the further HCO hydrogenation is exothermic ($\Delta E=-0.27eV$).

CO binding energy on different metal oxide chain/Cu(111) systems are plotted in Figure 5.9(b). Among all the systems considered here, only TiO_2/Cu(111) is able to promote methanol production from RWGS+CO-Hydro pathway due to a stronger binding of CO at the interface. ZnO and MoO_3 should not affect the activity much via RWGS+CO-Hydro pathway.

5.3.3.3. Metal oxide size effect on RWGS+CO-Hydro pathway

Particle size cannot affect the activity at the interface of Cu and metal oxide for ZnO and MoO_3. No promotion effect is observed on the metal cluster/Cu(111) or metal chain/Cu(111) structures. However, smaller TiO_2 nanoparticles should show a superior activity than their bigger counterparts considering that the Ti_3O_6 cluster stabilizes CO even more than TiO_2 chain structure.

5.4. Conclusion

DFT calculations were carried out in order to understand the support effect on the activity of Cu-based catalysts for methanol production from both the formate pathway and RWGS+CO-Hydro pathway. Inverse model catalysts were used to model the Cu-metal oxide interface, where metal oxide clusters were deposited on Cu(111). To elucidate the size effect of the metal oxide nanoparticles, metal oxide chain structure were also employed in this study to model relatively larger particles with bulk-like structures.

The calculations show that H adsorption is stronger on all the systems except for Mo_3O_9/Cu(111). Metal oxide/Cu(111) cannot promote the methanol production efficiently via formate pathway because the H_2COO hydrogenation step is difficult. This is due to the strong interaction between H and oxide, which makes the further hydrogenation barrier high. H binding to Cu(111) directly can also be the H source for hydrogenation reactions. More calculations need to be carried out to take H binding to Cu(111) into consideration.

Among all the systems considered in this study, Ti_3O_6/Cu(111) should be able to promote methanol production from RWGS+CO-Hydro pathway because CO can be stabilized by the interface of Cu-Ti_3O_6. Such stabilization is also observed on TiO_2/Cu(111). A better activity should be expected on Ti_3O_6/Cu(111) due to a stronger CO binding. No such promotion effect can be expected from the rest of the systems in this study. The stabilization of CO by Ti_3O_6 is due to its unique structure, which has an exposed Ti site for CO to interact with. A calculation on the full reaction pathways on Ti_3O_6/Cu(111) will be carried out in the future to understand the reaction mechanism completely.

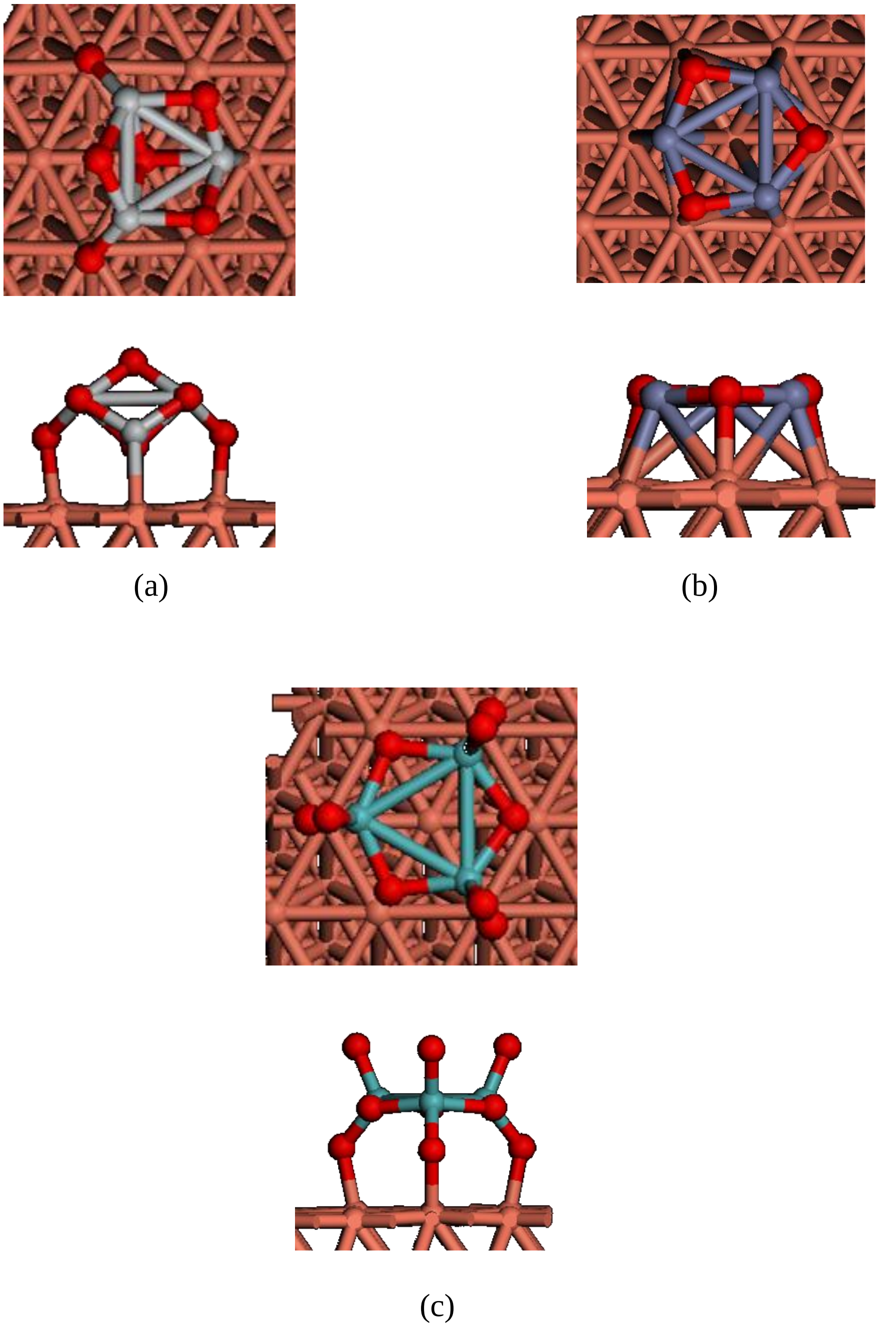

(a)

(b)

(c)

Figure 5.1. Top view and side view of optimized geometries of metal-oxide cluster/Cu(111): Ti_3O_6/Cu(111) (a); Zn_3O_3/Cu(111)(b); Mo_3O_9/Cu(111) (c); (d). (Brown: Cu; gray: Ti; blue: Zn; green: Mo; red: O)

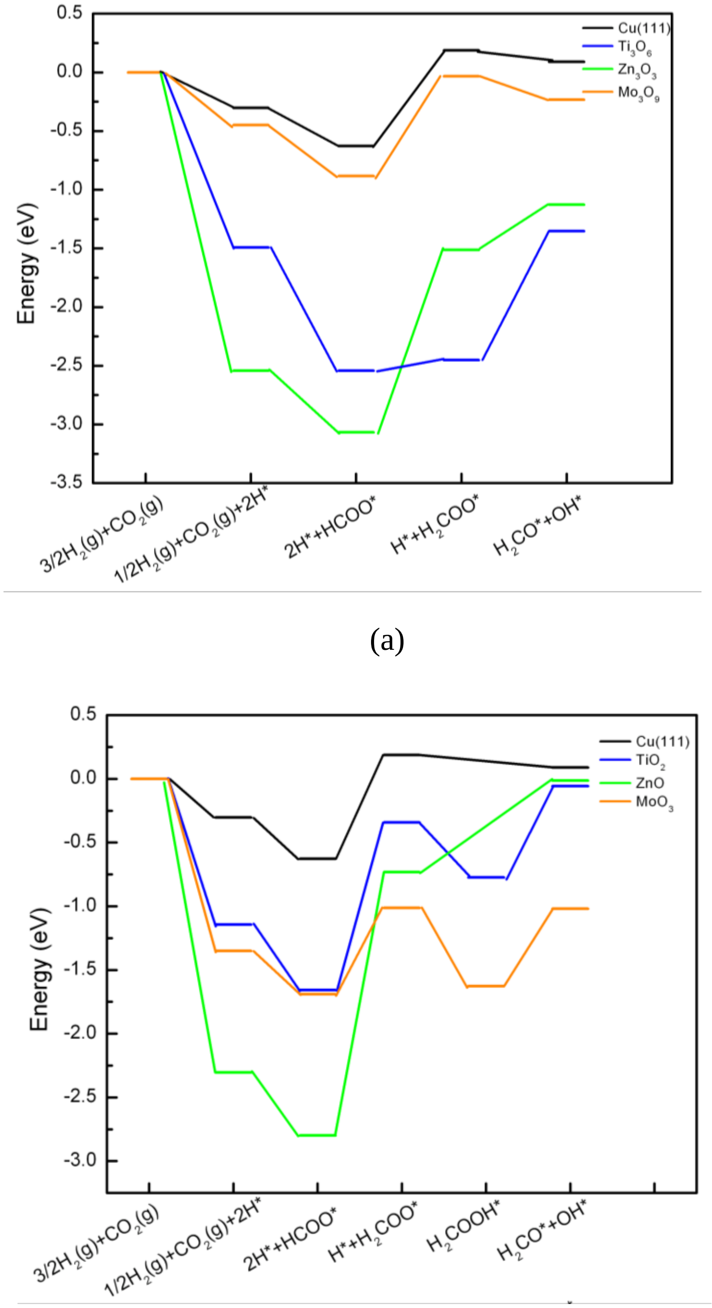

(a)

(b)

Figure 5.2. Reaction energetics of HCOO and H_2COO hydrogenation to H_2CO on metal oxide cluster/Cu(111) (a) and metal oxide chain/Cu(111) (b).

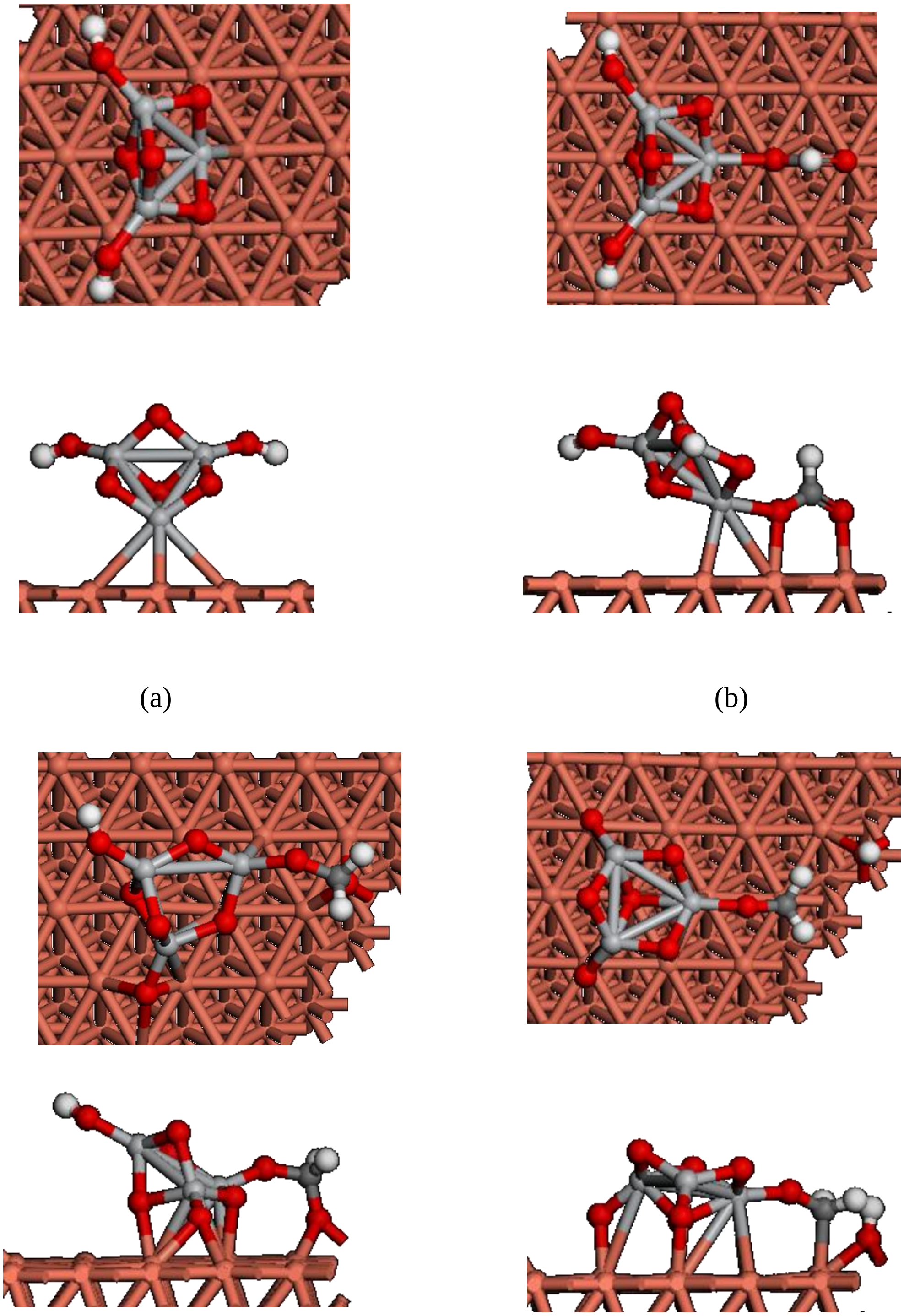 (a) (b) (c) (d)

Figure 5.3. Top view and side view of optimized geometries of adsorbates on Ti_3O_6/Cu(111): 2H(a);2H+HCOO (b); H+H_2COO(c); H_2CO+OH(d). (Brown: Cu; gray: Ti; red: O; white: H)

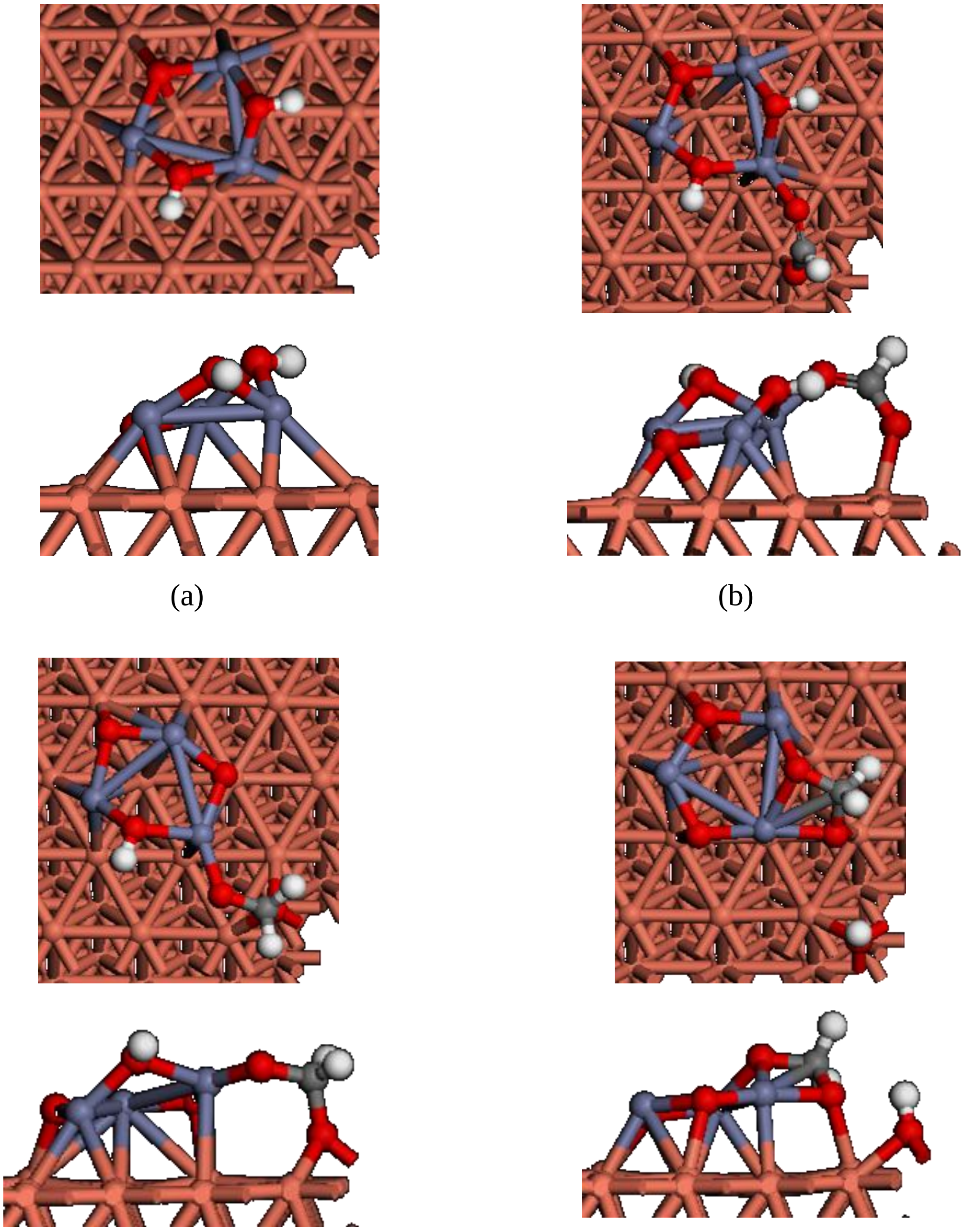

(a) (b)

(c) (d)

Figure 5.4. Top view and side view of optimized geometries of adsorbates on Zn_3O_3/Cu(111): 2H(a);2H+HCOO (b); H+H_2COO(c); H_2CO+OH(d).(Brown: Cu; blue: Zn; red: O; white: H)

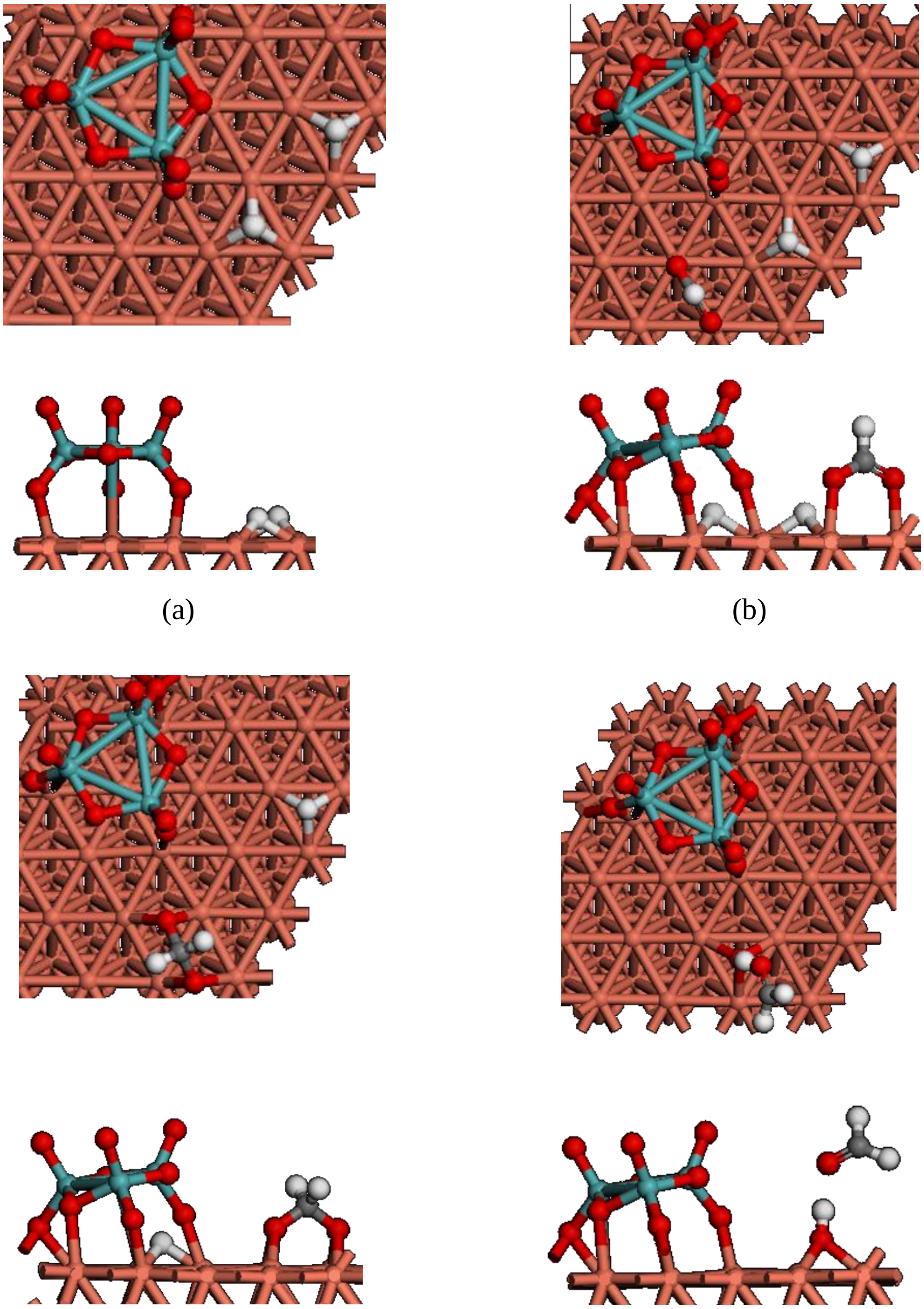

(a)

(b)

(c)

(d)

Figure 5.5. Top view and side view of optimized geometries of adsorbates on Mo_3O_9/Cu(111): 2H(a);2H+HCOO (b); H+H_2COO(c); H_2CO+OH(d). (Brown: Cu; green: Mo; red: O; white: H)

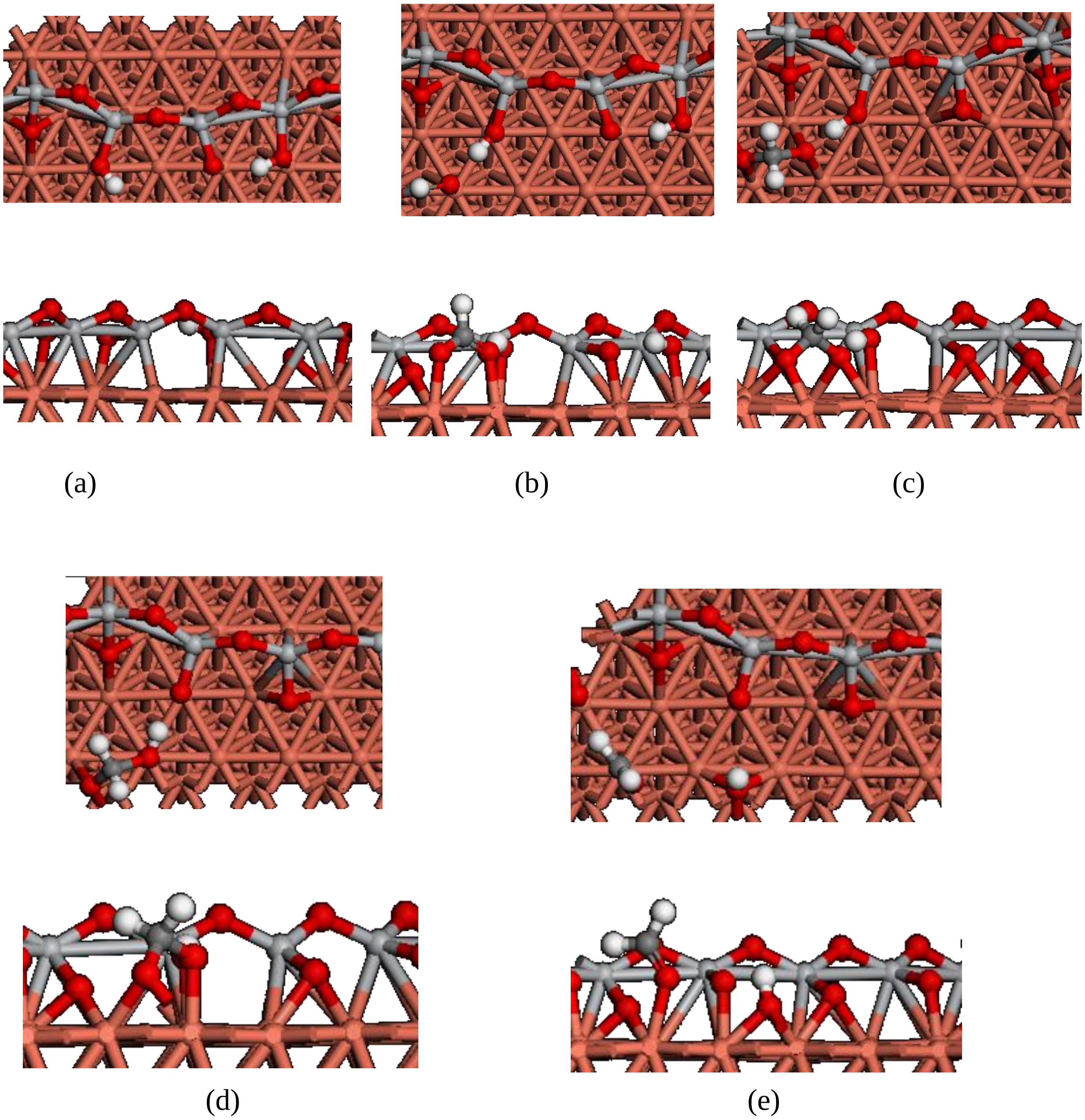

(a) (b) (c)

(d) (e)

Figure 5.6. Top view and side view of optimized geometries of adsorbates on TiO_2/Cu(111): 2H(a); 2H+HCOO (b); H+H_2COO(c); H_2COOH(d) and H_2CO+OH(e). (Brown: Cu; gray: Ti; red: O; white: H)

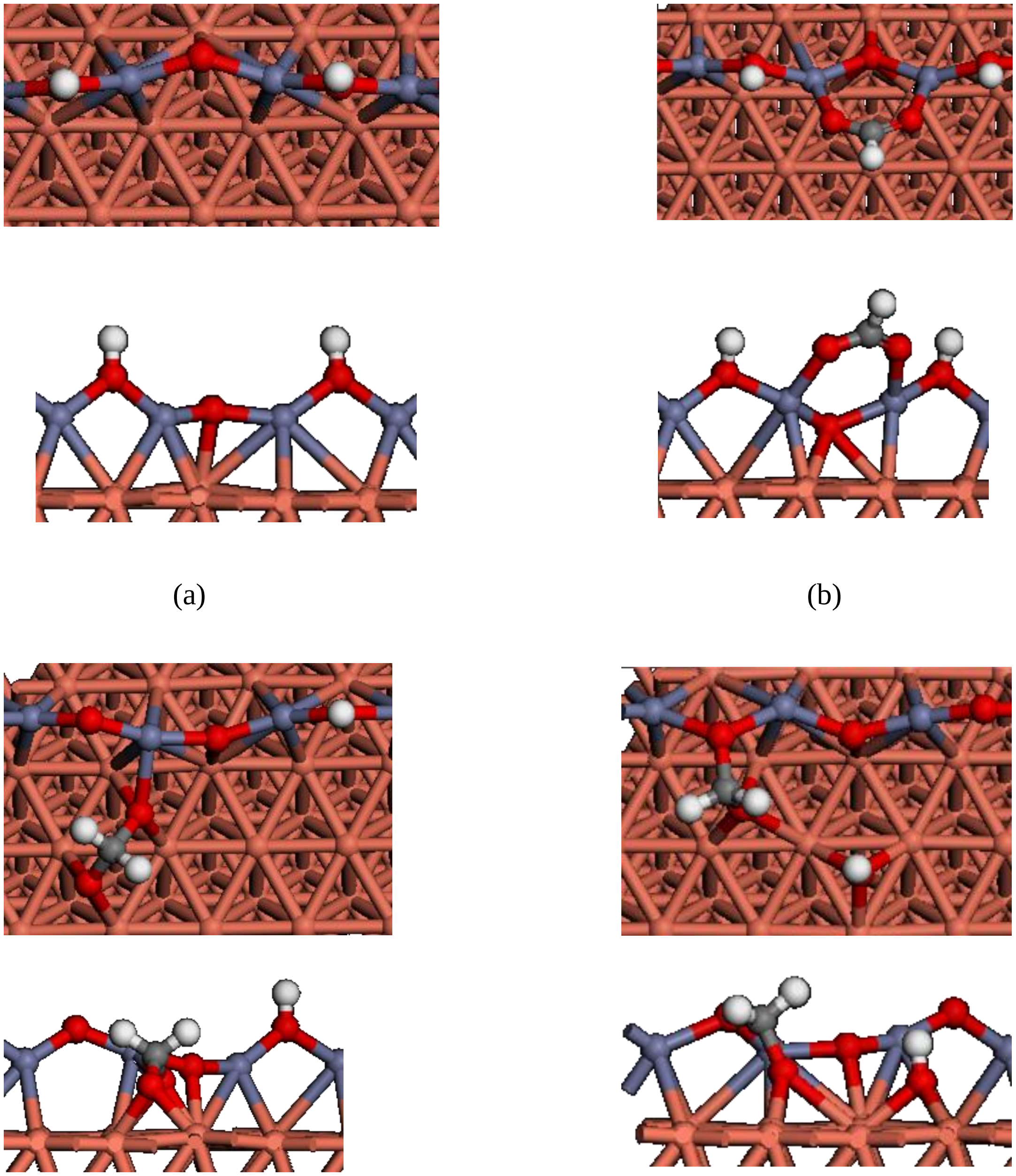
(a) (b) (c) (d)

Figure 5.7. Top view and side view of optimized geometries of adsorbates on ZnO/Cu(111): 2H(a); 2H+HCOO (b); H+H_2COO(c); H_2CO+OH(d). (Brown: Cu; blue: Zn; red: O; white: H)

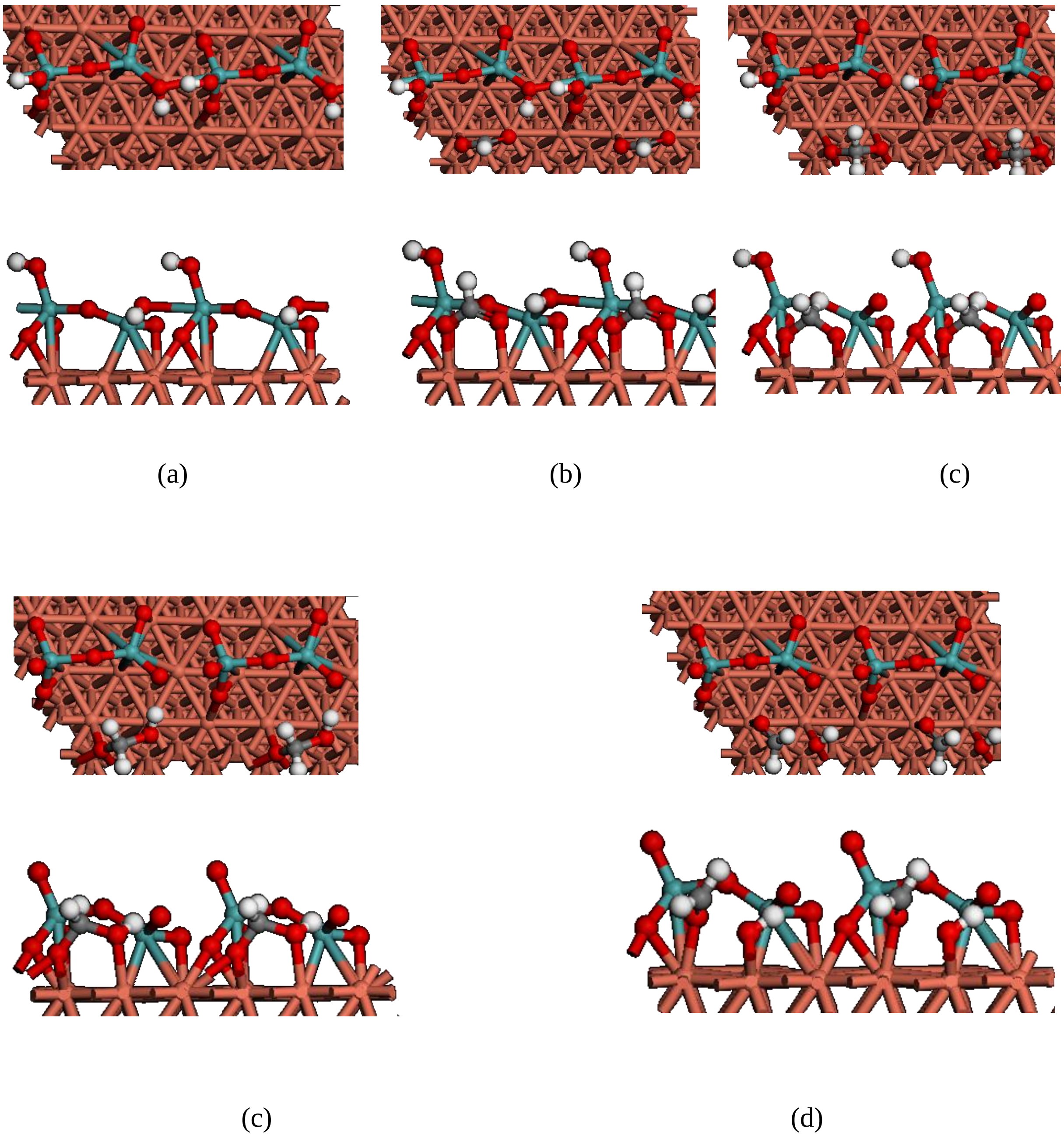
(a) (b) (c)

(c) (d)

Figure 5.8. Top view and side view of optimized geometries of adsorbates on MoO_3/Cu(111): 2H(a); 2H+HCOO (b); H+H_2COO(c); H_2COOH(d) and H_2CO+OH(e). (Brown: Cu; green: Mo; red: O; white

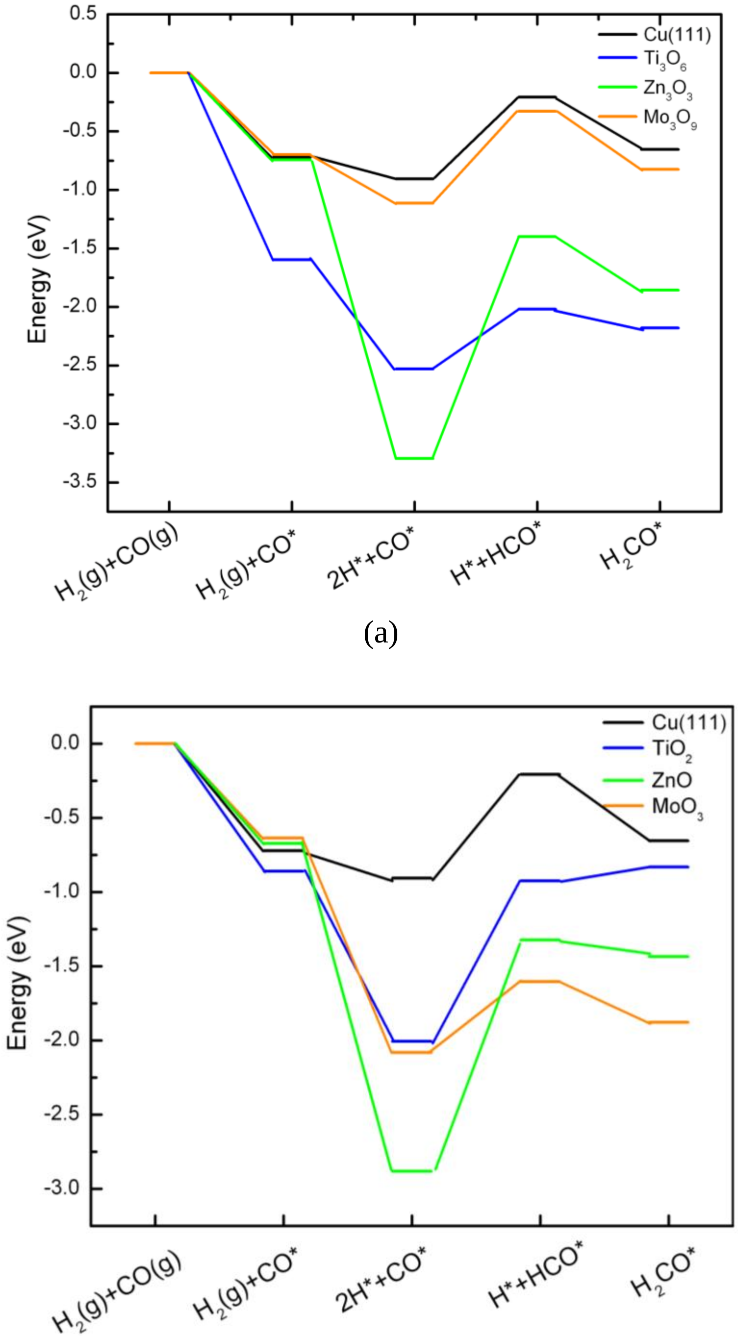

(a)

(b)

Figure 5.9. Reaction energetics of CO hydrogenation to H_2CO on metal oxide cluster/Cu(111) (a) and metal oxide chain/Cu(111) (b).

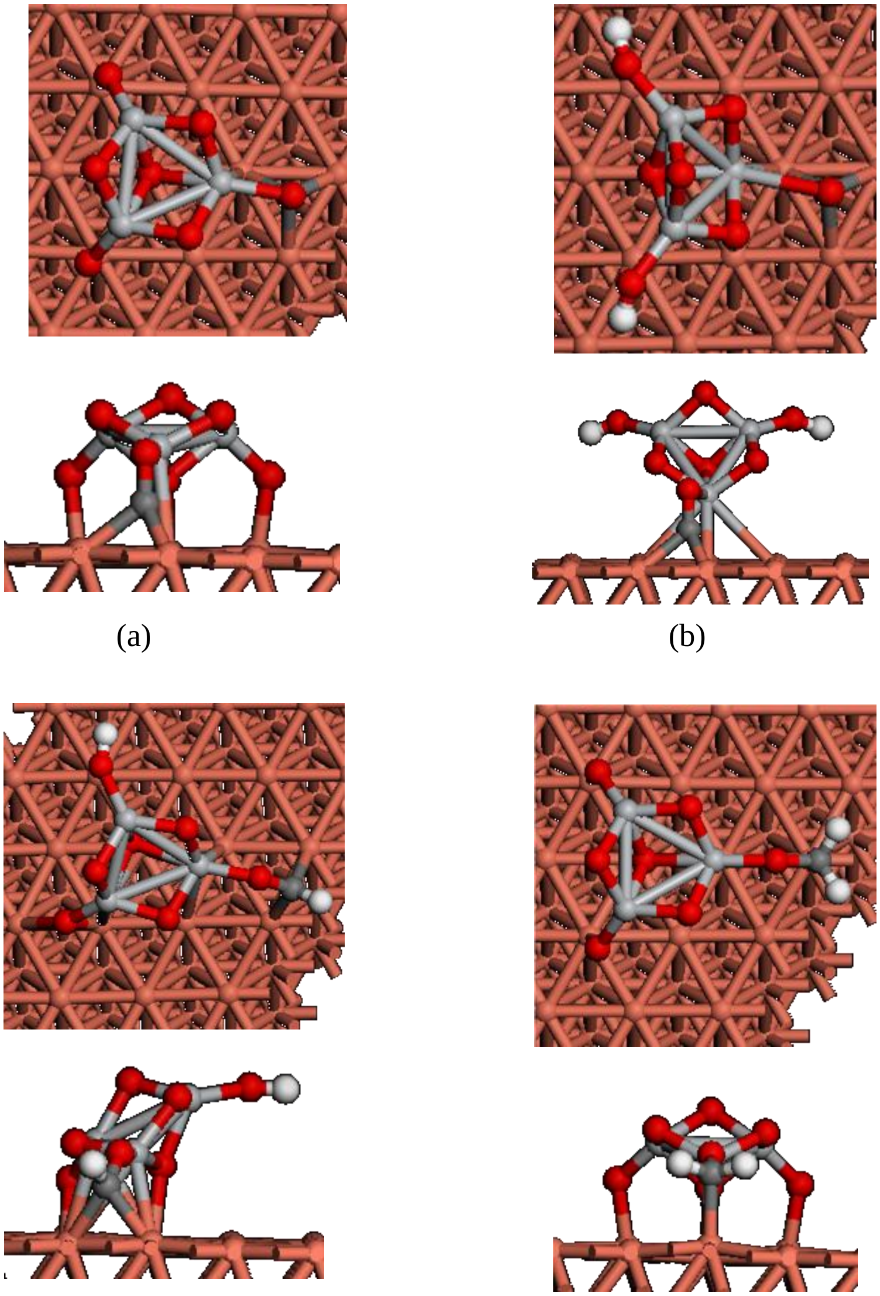

(a) (b)

(c) (d)

Figure 5.10. Top view and side view of optimized geometries of adsorbates on Ti_3O_6/Cu(111): CO (a); 2H+CO(b); H+HCO(c); H_2CO (d). (Brown: Cu; gray: Ti; red: O; white: H)

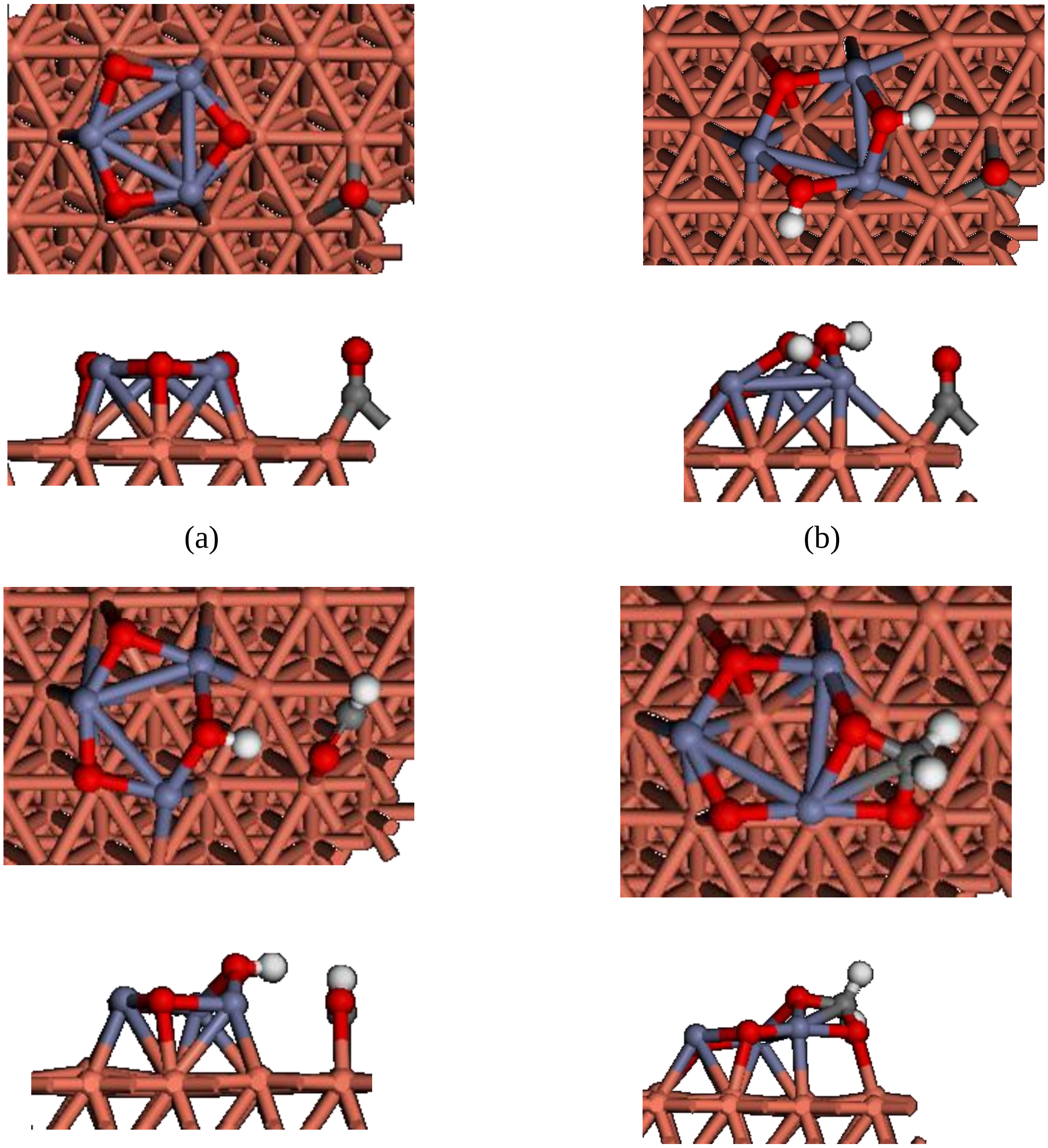

(a)

(b)

(c)

(d)

Figure 5.11. Top view and side view of optimized geometries of adsorbates on Zn_3O_3/Cu(111): CO (a); 2H+CO(b); H+HCO(c); H_2CO (d). (Brown: Cu; blue: Zn; red: O; white: H)

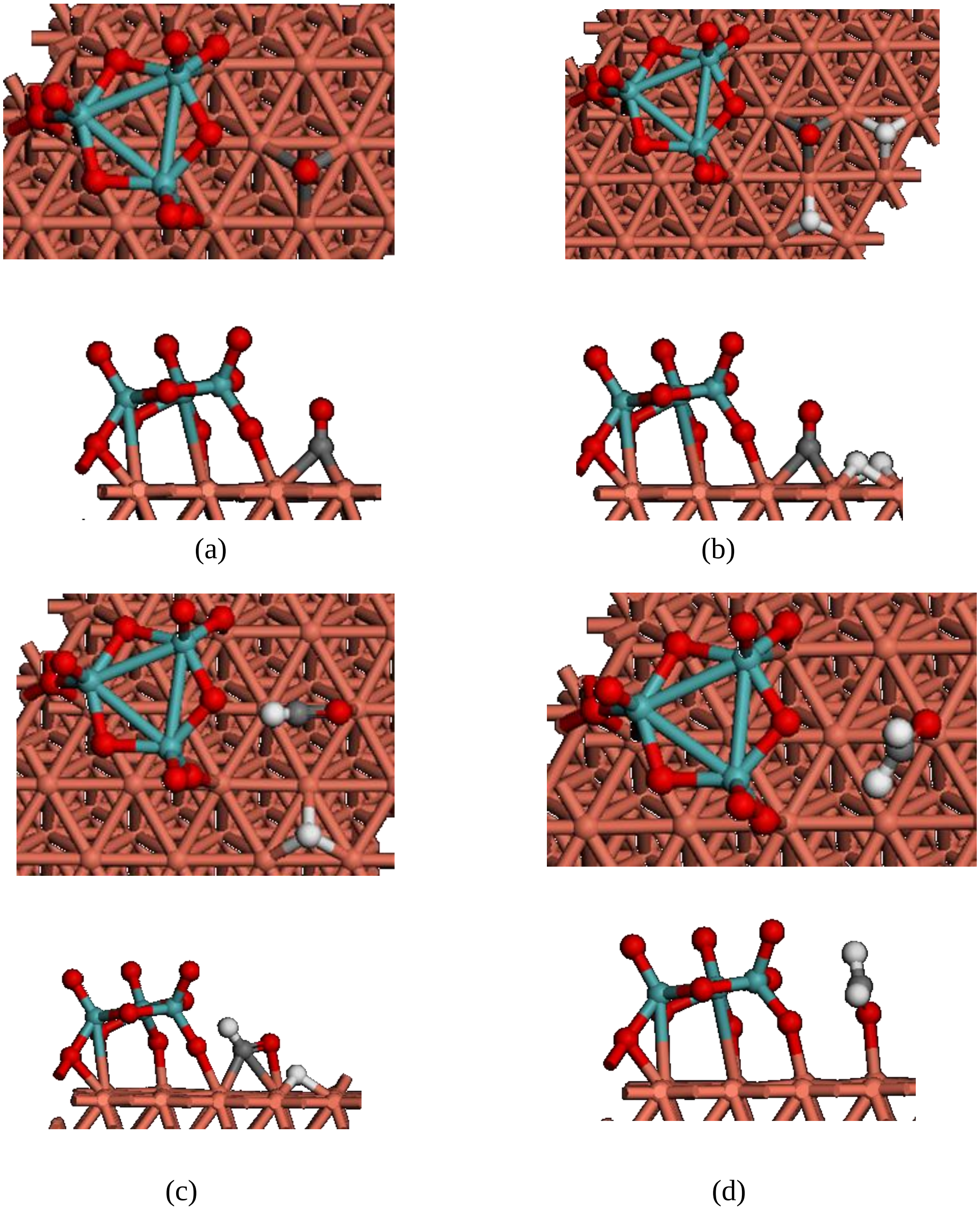

(a) (b)

(c) (d)

Figure 5.12. Top view and side view of optimized geometries of adsorbates on Mo_3O_9/Cu(111): CO (a); 2H+CO(b); H+HCO(c); H_2CO (d). (Brown: Cu; green: Mo; red: O; white: H)

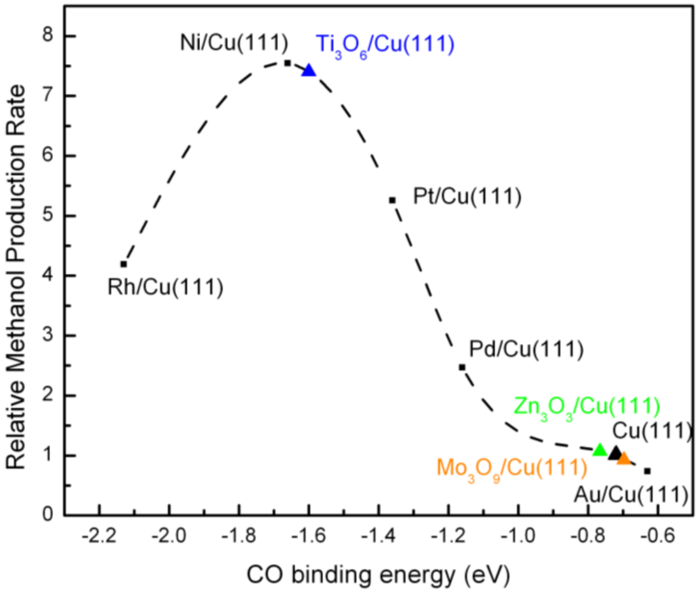

(a)

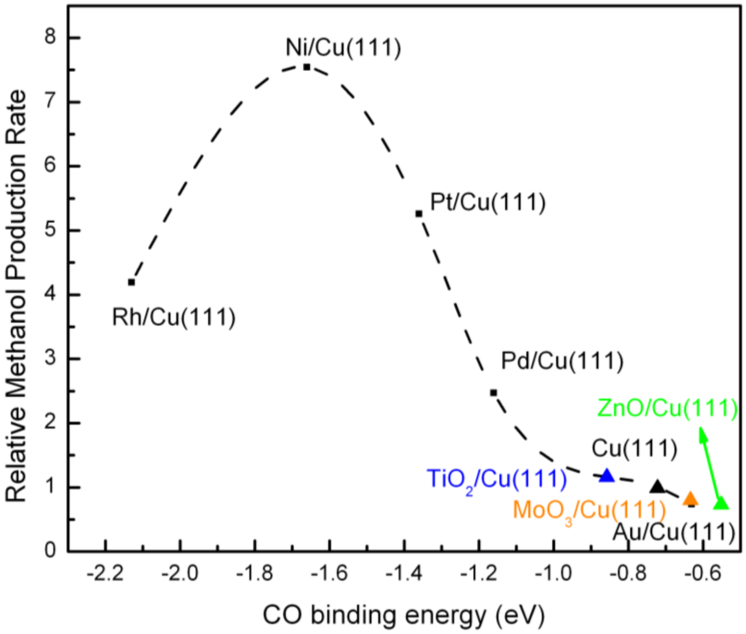

(b)

Figure 5.13. CO binding energy on metal oxide cluster/Cu(111) (a) and metal oxide chain/Cu(111) (b).

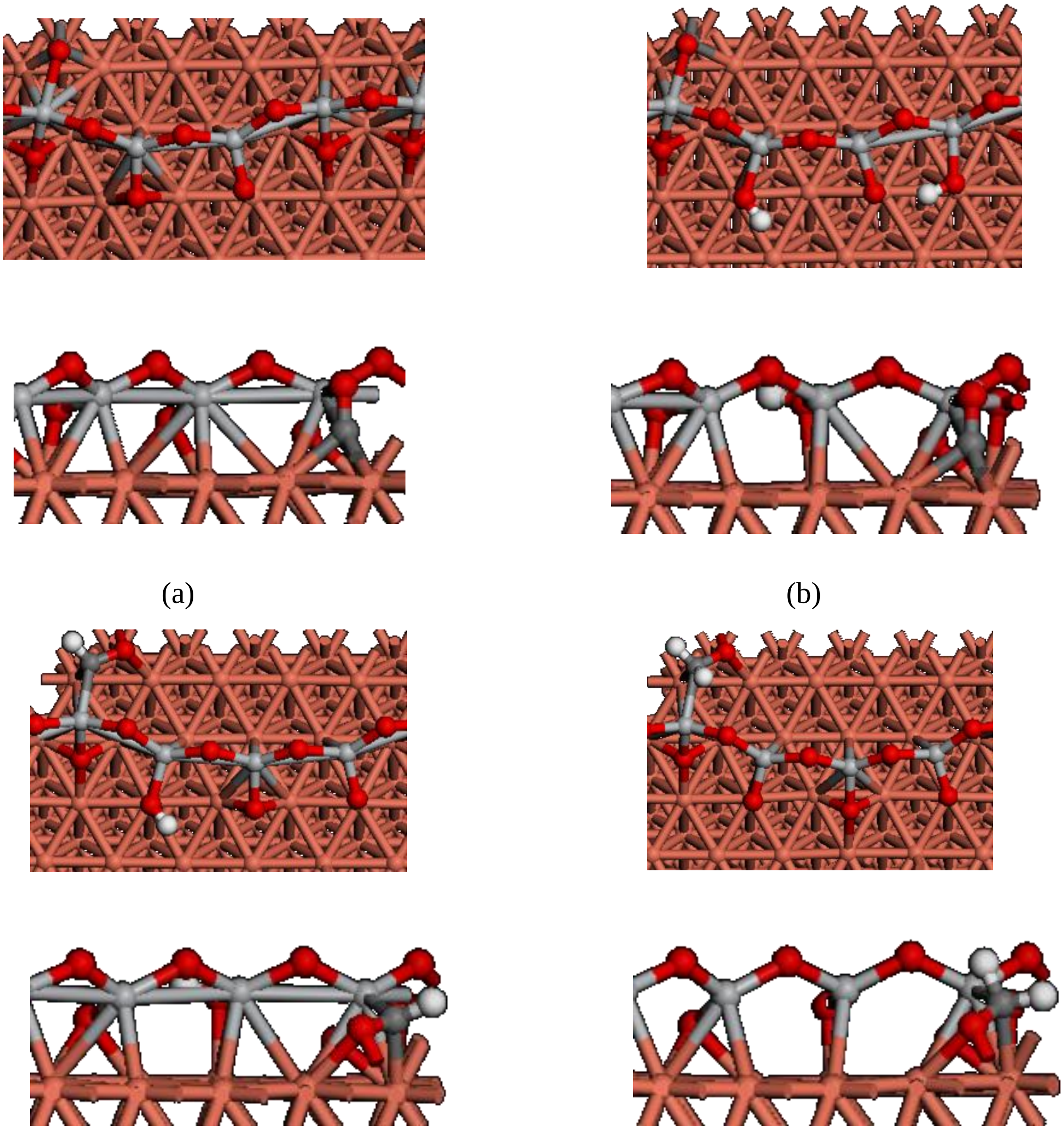

(a) (b) (c) (d)

Figure 5.14. Top view and side view of optimized geometries of adsorbates on TiO_2/Cu(111): CO (a); 2H+CO(b); H+HCO(c); H_2CO (d). (Brown: Cu; gray: Ti; red: O; white: H)

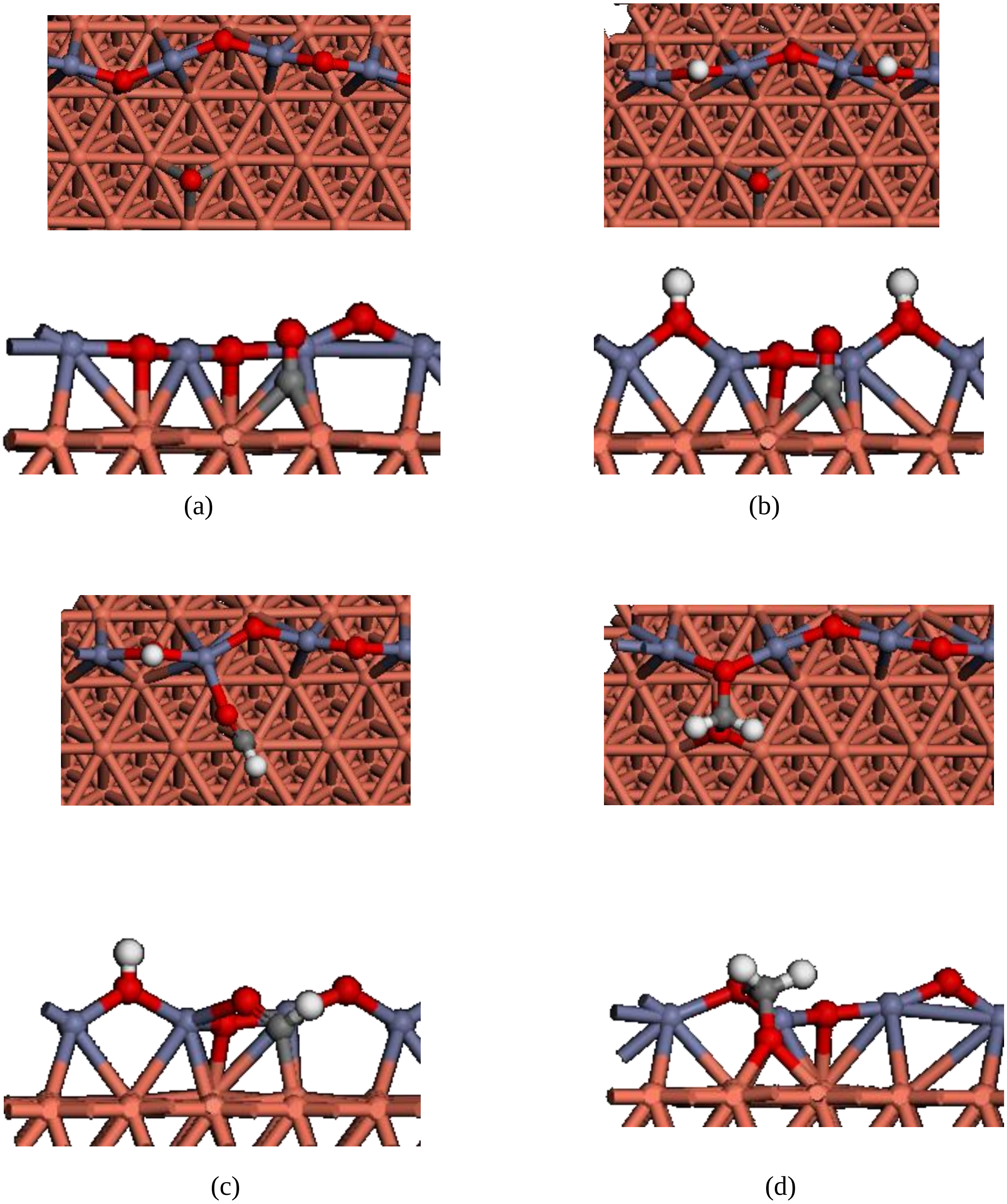

Figure 5.15. Top view and side view of optimized geometries of adsorbates on ZnO/Cu(111): CO (a); 2H+CO(b); H+HCO(c); H_2CO (d). (Brown: Cu; blue: Zn; red: O; white: H)

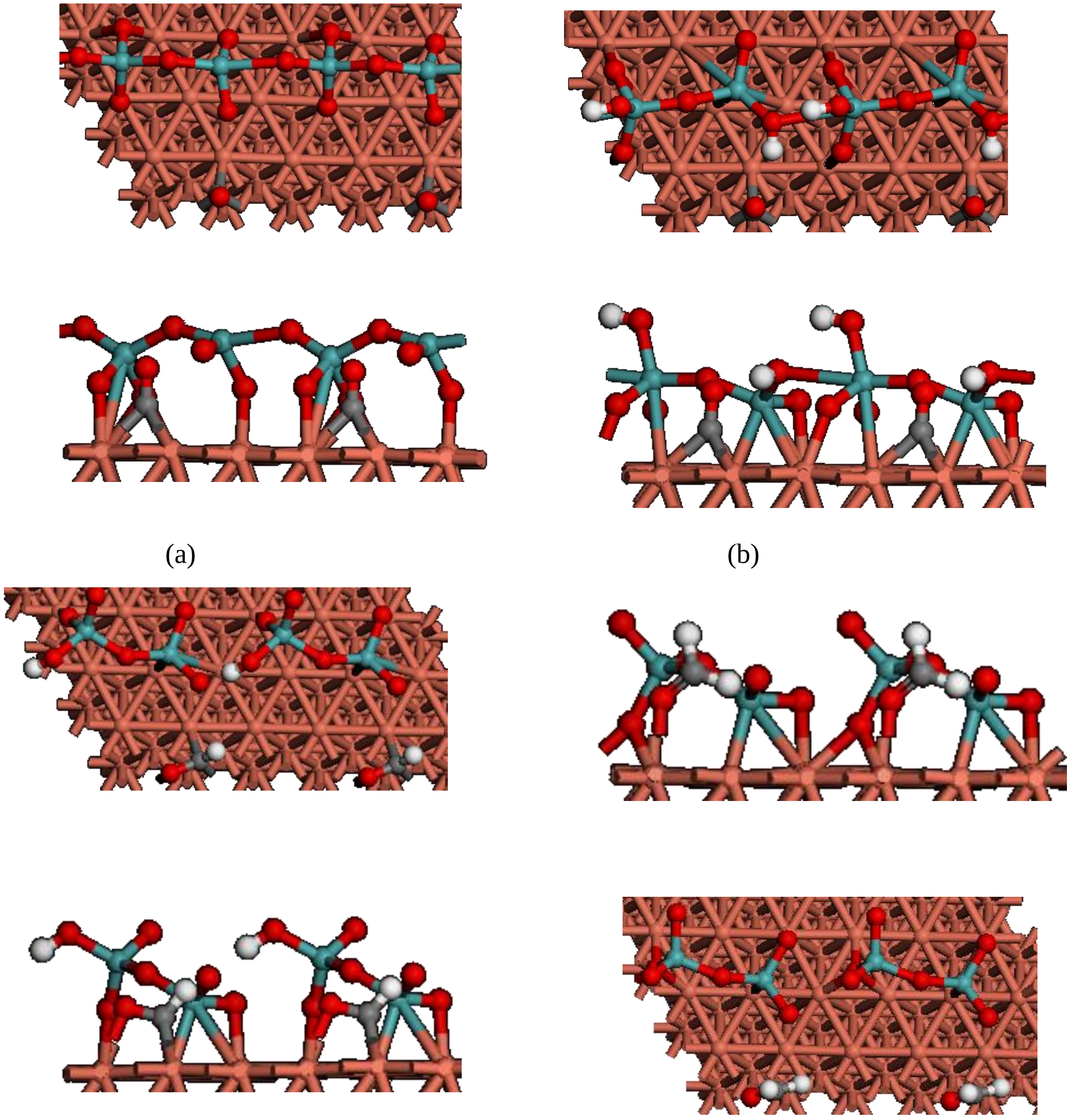

(a) (b)

(c) (d)

Figure 5.16. Top view and side view of optimized geometries of adsorbates on MoO$_3$/Cu(111): CO (a); 2H+CO(b); H+HCO(c); H$_2$CO (d). (Brown: Cu; green: Mo; red: O; white: H)

Chapter 6. Surface dipole and charge transfer at an oxide-metal interface: a 2PPE study of size-selected metal oxide clusters supported on Cu(111)

6.1. Introduction

Metal oxide supported Cu catalysts have attracted considerable attention because they are active towards several industrially important reactions, e.g. water-gas-shift (WGS)[117,118], methanol synthesis[2,8] and methanol steam reforming[116,119]. A synergetic effect has been widely reported between Cu and metal oxide supports because the supports can significantly affect the overall catalyst activity[2,117]. Besides dispersing the Cu nanoparticles, the support can also participate in the reaction directly or affect the activity indirectly by modifying the Cu oxidation state[2]. Therefore, a fundamental understanding of interactions at the Cu-metal oxide interface is desired in order to tune the catalyst activity as needed. In this work, inverse catalysts were employed to model the Cu-metal oxide interface. Metal oxide nanoclusters were deposited onto Cu(111), which is different from the conventional model catalyst, where Cu nanoparticles are supported on a metal oxide. The use of such inverse catalysts makes electronic spectroscopy measurements possible due to the high conductivity of Cu(111), whereas most of the bulk metal oxide single crystals are insulators[120]. Moreover, inverse catalysts can even exhibit superior activity compared with its conventional counterpart due to the stabilization of defect sites on the oxide nanoparticles[105].

In this study, we investigated the interfacial electronic structures of a number of metal oxide clusters, Mo_3O_6, Mo_3O_9, W_3O_6, W_3O_9, Ti_3O_6 and Ti_5O_{10}, deposited on a Cu(111) surface using a combination of two-photon photoemission (2PPE) spectroscopy and density functional theory (DFT) calculations. Previous DFT calculations on the stoichiometric clusters Mo_3O_9, W_3O_9, and Ti_3O_6 showed that activity towards WGS reaction was strongly correlated to `the detailed electronic structures at the Cu-metal oxide interface as a result of charge transfer between Cu and metal oxide clusters[106]. The size-selected cluster beam deposition apparatus[121,122] employed in this work allows us to investigate the same model system as in the theoretical study. The charge transfer at the Cu-metal oxide interface was probed by surface work function (Φ) measurements using 2PPE, because the work function is very sensitive to the surface dipole resulting from oriented adsorbate dipoles and adsorbate-surface charge transfer[123]. As shown in our previous study, the density of deposited clusters varies smoothly across the surface of the substrate and can be described by a Gaussian distribution[121,122]. By scanning the small focused UV laser spot (~250µm) used for 2PPE across the surface, it is possible to measure the coverage-dependent local work function from a single deposition. The surface dipole moment due to the Cu-cluster interactions can be easily derived from the relationship between work function cluster coverage using the Topping model[124]. Both stoichiometric (Mo_3O_9 and W_3O_9) and "reduced" (Mo_3O_6 and W_3O_6) clusters were investigated in this study in order to understand the role of metal oxidation state in the interaction between the oxide cluster and Cu substrate. Cluster size effects were also addressed by comparing the results for the two the stoichiometric clusters, Ti_3O_6 and Ti_5O_{10}.

6.2. Experimental and theoretical methods

6.2.1. Experimental setup

The experiments were carried out using a size-selected cluster beam deposition apparatus, as described in our previous studies[121,122]. The Cu(111) crystal (Princeton Scientific; 11mm diameter x 2 mm thick) was mounted on a Mo plate (0.01" thick) by Mo clips and screws to ensure optimal thermal and electrical contact. The crystal could be resistively heated by two Ta rods (1mm diameter) welded onto the Mo plate. Gold foil was placed between the crystal and the mounting plate to optimize thermal conductivity. The crystal temperature was measured with a K-type thermocouple, which was held in a small hole on the edge of the crystal using high temperature ceramic cement (Omegabond 600). The Cu(111) crystal surface was routinely cleaned by two cycles of Ar^+ sputtering (30min at 1keV), followed by annealing (20 min at 700K) before each measurement. No impurities could be detected on Cu(111) by Auger electron spectroscopy (AES) using this cleaning procedure.

The metal oxide clusters were produced in a magnetron sputtering source. The metal targets were sputtered in a gas mixture of ~2% O_2 in Ar. The exact O_2 ratio was optimized for the best yield of each cluster of interest. The produced gas-phase cluster cations were mass-selected by a quadrupole filter and deposited onto the cleaned Cu(111) surface. For all the clusters studied here, the deposition kinetic energy was measured to be close to 0 eV, assuring soft-landing conditions. The total number of clusters deposited onto the surface was obtained by integrating the cluster ion current on the crystal during cation deposition.

The detailed setup for 2PPE experiments was described in our previous studies[123]. Work functions were obtained by one-color 2PPE measurements using the third-harmonic radiation (~277 nm, hν = 4.48eV) from an ultrafast Ti: Sapphire laser system (Spectra-Physics Tsunami; 750-900 nm, 100-fs pulse width). The laser pulse was p-polarized at an incident angle of 47.5° with regard to the surface normal. The beam was focused onto the surface to a spot with an estimated diameter of ~250μm. Photoelectrons were detected along the surface normal by a hemispherical electron energy analyzer (Specs Phoibos 100). A bias voltage of −4.0eV was applied to the crystal to enhance the detection efficiency of secondary electrons with low kinetic energy. The same electron energy analyzer was also used for the AES measurement. An electron beam of 5keV was used to excite the AES transitions. The crystal was translated along both horizontal (x-axis) and vertical directions (z-axis) during AES and 2PPE measurements in order to obtain cluster coverage-dependent density and work function measurements, respectively.

6.2.2. Theoretical methods

Spin-polarized DFT calculations were carried out using the Vienna *ab initio* simulation package (VASP)[108-110] to elucidate the cluster adsorption configurations on Cu(111). The generalized gradient approximation proposed by Perdew and Wang[9] was employed for the exchange and correlation functional. The plane-wave-pseudopotential with a cutoff energy of 400eV within the projector augmented wave (PAW)[111] method was used. Mo(4p, 4d, 5s), W(4f, 5d, 6s), Ti(3s,3p,3d, 4s), O(2s, 2p) were treated explicitly as valence states, while the remaining electrons were kept frozen as core states. The DFT+U[10] method was applied in order to correct the tendency to over delocalize electrons in standard DFT methods. A value of U = 4.5eV was applied to Ti, which gave a reasonable description of the electronic structures of rutile $TiO_2(110)$ surface[113,114]. A Gaussian smearing method with an electronic temperature of $k_BT = 0.05eV$ was applied to obtain faster convergence. The Cu(111) surface was modeled by a four-layer slab with a (5×5) unit cell, separated by a 20-Å-thick vacuum layer. The bottom two layers of atoms were fixed in their optimized bulk positions while the top two layers were allowed to relax. Brillouin-zone integrations were performed on a grid of 3×3×1 Monkhorst-Pack[11] special **k**-points. The initial structures of Mo_3O_9, W_3O_9 and Ti_3O_6 deposited on Cu(111) were taken from our previous calculations[106]. To calculate the configurations of Mo_3O_6, W_3O_6 and Ti_5O_{10} after deposition, the reported gas-phase Mo_3O_6[125], W_3O_6[125] and Ti_5O_{10}[126] structures were placed on Cu(111) and the structures were relaxed along with Cu(111) during self-consistent calculations. The charge transfer between the clusters and Cu(111) was calculated using Bader analysis program[127], based on Bader's theory[128].

6.3. Results and Discussion

6.3.1. Cluster distributions and 2PPE spectra

To measure the cluster density across the Cu(111) crystal surface, Auger spectra were taken at 0.5mm steps along the horizontal (x-axis) and vertical (z-axis) directions. The step size is reasonable considering the diameter of the incident electron beam is even smaller (less than 0.2mm). The area of the O (KLL) peak at ~512 eV was used to quantify the metal oxide cluster distribution due to the relatively low Auger sensitivity of the metal elements. Figure 6.1 shows the O (KLL) peak area of Mo_3O_9/Cu(111) as a function of crystal position along the x-axis as an example. As seen in the figure, the cluster distribution can be well described by a Gaussian function and the center of deposition can be easily determined by a least-squares Gaussian fit. A similar Gaussian distribution is obtained along the z-axis. As a result, the metal oxide cluster distribution on Cu(111) can be well described using a two-dimensional Gaussian function. Using the measured total number of deposited clusters (N) by integrating the cluster ion current on the crystal during cation deposition, the number of clusters (n) within a specific area (S) can be easily calculated. If we define the cluster density n_a as:

$$n_a = \frac{n}{S}. \tag{6.1}$$

The local cluster coverage θ (ML) can be calculated by:

$$\theta = n_a \times A \tag{6.2}$$

where A is the cross sectional area of the cluster. The cluster area A was estimated assuming a circular cross section (elliptical cross section for Ti_5O_{10} due to its asymmetrical structure) and a cluster radius derived from our DFT calculations. Figure 6.2 shows the adsorption configurations of the metal oxide clusters on Cu(111). Taking the Van der Waals radius of O (1.52Å[129]) into account, the metal oxide cluster radii and the corresponding coverage on Cu(111) were estimated and listed in Table 6.1. Using the known laser beam size (~250μm diameter) to estimate *S*, the local coverage of metal oxide clusters can then be calculated using Eq(6.2).

2PPE spectra were taken at 0.25mm steps along the horizontal (x-axis) and vertical (z-axis) directions. Figure 6.3 shows the 2PPE spectra for the Mo_3O_9/Cu(111) surface acquired at several different positions of the crystal. The spectra were plotted in terms of final state energy, in which the low-energy cutoff position corresponds to the work function. On clean Cu(111), the measured work function is ~4.85eV, consistent with previous reported values[130,131]. For the photon energy used here (hν = 4.48 eV), the Cu(111) surface state (SS), lying 0.4eV below Fermi level (E_F)[130,131], and the first image state (IS_1), lying 0.8eV below E_F[130], correspond to final state energies of 8.56eV and 8.53eV, respectively. These two features are not completely resolved in our experiment and correspond to the sharp asymmetric peak at ~8.48eV in our 2PPE spectrum of Cu(111). After the deposition of Mo_3O_9 on Cu(111), photoemission from IS_1 and SS are quenched. Meanwhile, the low-energy cutoff shifts to a higher final state energy, i.e., a higher work function. Work function shift used in this study is defined as:

$$\Delta\Phi = \Phi[\text{cluster/Cu(111)}] - \Phi[\text{Cu(111)}]. \qquad (6.3)$$

Figure 6.4 shows the work function shift on Mo_3O_9/Cu(111) as a function of crystal position along the x-axis. The work function shift can also be described by a Gaussian function as seen in the figure. The peak position corresponds to the center of deposition. The center of deposition from 2PPE and AES should be the same point if we assume the more clusters there are, the bigger the work function shift is. Using the center deposition position as a reference point, the local coverage of each data point in 2PPE experiment can be calculated.

Similar 2PPE experiments were carried out for the W_3O_9, Ti_3O_6, Mo_3O_6, W_3O_6 and Ti_5O_{10} clusters deposited on Cu(111). Similar to the data in Figure 6.3, all of the clusters studied in this work resulted in an increase in work function when deposited on the Cu(111) surface.

6.3.2. Work function shift and surface dipole

Figure 6.5 shows the work function shifts as a function of local coverage for all the clusters included in this study. The observed increases in work function with increasing cluster coverage can be attributed to the introduction of interface dipole moments by the deposition of the metal oxide clusters. Because the work function shifts to higher values, the resultant surface dipole moment is negative, i.e., pointing towards the surface. Even though the directions of the surface dipole moments are the same for all the clusters, the magnitude is strongly dependent on the specific cluster. In order to understand such cluster-dependent behavior more quantitatively, the Topping model[124] was employed to analyze the data. The work function shift can be described as:

$$\Delta\Phi = \frac{e n_a \mu}{\varepsilon_0}\left(1 + \frac{9\alpha\delta n_a^{\frac{3}{2}}}{4\pi}\right)^{-1} \tag{6.4}$$

where e is the charge of an electron, n_a is the cluster density, ε_0 is the vacuum permittivity, μ is the normalized interface dipole moment per cluster, α is the cluster polarizability and δ is a cluster mobility parameter. The second term in the bracket represents depolarization caused by dipole-dipole interaction and effectively reduces the magnitude of the surface dipole at higher cluster density. For randomly distributed dipoles on the surface, appropriate to our deposition conditions, the value of δ is given by the lattice gas model, [132]

$$\delta = \theta^{-0.5}. \tag{6.5}$$

Taking Eq (6.2) and (6.5) into consideration, equation (6.4) can be rewritten in terms of the cluster coverage and cluster area as:

$$\Delta\Phi = \frac{e\mu\theta}{A\varepsilon_0}\left(1 + \frac{9\alpha\theta}{4\pi A^{\frac{3}{2}}}\right)^{-1} . \tag{6.6}$$

The solid lines in Figure 6.5 are the fits of the cluster work function data to Eq(6.6). The surface dipole moments μ extracted from the fits are summarized in Table 6.1. Note that the derived dipole moments represent the dipole directed along the surface normal since this is the only component that affects the surface work function.

For Mo_3O_9/Cu(111), the derived surface dipole moment is –4.52 D. The negative sign indicates a dipole pointing towards the surface. The behavior of W_3O_9/Cu(111) is similar as Mo_3O_9/Cu(111), with a slightly smaller surface dipole moment (μ =–3.96D). In order to further understand the effect of oxidation state on Cu-cluster charge transfer, experiments were also performed on Mo_3O_6/Cu(111) and W_3O_6/Cu(111), which have formal oxidation states of +4 compared to +6 for the M_3O_9 (M = Mo, W) clusters. The surface dipole moments from these reduced clusters are significantly smaller (μ =-1.71D for Mo_3O_6/Cu(111) and μ =-2.30D for W_3O_6/Cu(111)) compared with their stoichiometric counterparts. The behavior of the Ti_3O_6/Cu(111) surface is quite distinct, with small work function shifts that are essentially linear with cluster coverage. This suggests that the effects of depolarization on the Ti_3O_6/Cu(111) surface are not evident over the coverage range studied in this work (≤ 1 ML). The small work function shifts lead to a correspondingly small surface dipole moment (μ = –0.48 D). The depolarization effect is not obvious on the Ti_5O_{10}/Cu(111) surface either and the derived surface dipole is slightly bigger than that on Ti_3O_6/Cu(111) (μ = –0.87 D).

6.3.3. Origins of the observed surface dipole

The observed surface dipole can be attributed to different origins: the intrinsic dipole of the adsorbates and the dipole associated with the charge transfer between the adsorbate and the substrate[133,134]. DFT calculations were employed in this study so that we can identify the dominating origin of our observed surface dipole. Electrostatic potential energy along the surface normal from DFT calculation can provide a direct measurement of the system work function and interfacial dipole moment[134,135] because it is the potential an electron experiences when it moves in the average field of all the nuclei and other electrons. The overall electrostatic potential of the clusters deposited on Cu(111) ($V_{cluster/Cu(111)}$) can be divided into three components as:

$$V_{cluster/Cu(111)} = V_{Cu(111)} + V_{cluster} + V_{charge} \,, \tag{6.7}$$

where $V_{Cu(111)}$ and $V_{cluster}$ are the electrostatic potentials of isolated Cu(111) and cluster. The difference between $V_{cluster/Cu(111)}$ and the sum of $V_{Cu(111)}$ and $V_{cluster}$ is attributed to the potential due to the charge transfer between the cluster and Cu(111) (V_{charge}). $V_{cluster}$ is calculated by fixing the geometries of the clusters to the same as those when adsorbed on the Cu(111) surface.

Figure 6.6 shows the calculated average electrostatic potential along the surface normal for Mo_3O_9/Cu(111). The data are plotted such that the vacuum level energy is zero. With the known Fermi level energy from calculation, the work function can be derived conveniently. By comparing the work functions of Mo_3O_9/Cu(111) and Cu(111), the work function shift due to the deposition of Mo_3O_9 can be calculated. The calculated work function of Cu(111) is 4.74eV, which is consistent with the experimental results. It shifts higher by 1.46eV as a result of the deposition of Mo_3O_9 (Table 6.1). The increase of work function after deposition agrees well with our experimental observations. The dominant factor controlling the work function shift on Mo_3O_9/Cu(111) is the charge transfer potential. It is not surprising considering the highly symmetric structure of Mo_3O_9 (Figure 6.2(a)) and the potential change along the surface normal due to Mo_3O_9 is as small as -0.02eV. By comparison, the charge transfer potential shows a shift up by 1.48eV along the surface normal, which indicates a charge transfer from Cu(111) to

Mo_3O_9. The charge transfer direction is also consistent with the Bader charge analysis result, which show a charge transfer of 1.40e from the Cu(111) surface to the Mo_3O_9 cluster (Table 6.1).

Similar calculations were also conducted on the W_3O_9, Ti_3O_6, Mo_3O_6, W_3O_6 and Ti_5O_{10} clusters deposited on Cu(111). The calculated work function shift ($\Delta\Phi$), potential change along surface normal due to cluster ($\Delta V_{cluster}$), potential change along surface normal due to charge transfer (ΔV_{charge}) and bader charge analysis results are listed in Table 6.1.

As observed experimentally, the behavior of W_3O_9/Cu(111) from calculation is also similar to that of Mo_3O_9/Cu(111). The calculated work function shift is +1.57eV, slightly higher than that of Mo_3O_9/Cu(111). The dominant origin of the work function shift is also the charge transfer from Cu(111) to $W_3O_{9.}$ The potential change along surface normal due to charge transfer is the same as that on Mo_3O_9/Cu(111) ($\Delta V_{charge=}$+1.48eV), which is consistent with the Bader charge analysis, showing that charge transfer is nearly the same for Mo_3O_9 and W_3O_9 (Table 6.1). It is also worth pointing out that the electron affinities (EA) of these two clusters are also very close to each other[136] (Table 6.1).

The calculated work function shift on Mo_3O_6/Cu(111) is +0.20eV, which is significantly smaller than that on Mo_3O_9/Cu(111). Such trend agrees well with our experimental observation of a significantly smaller overall dipole moment on Mo_3O_6/Cu(111). The electrostatic potential from Mo_3O_6 is small and the charge transfer potential is still the dominant factor here. The potential change along surface normal due to charge transfer ($\Delta V_{charge=}$+0.31eV) is smaller comparing with that on Mo_3O_9/Cu(111). It is not surprising considering a smaller Bader charge transfer from Cu(111) to Mo_3O_6 and a smaller electron affinity of Mo_3O_6 (Table 6.1). Qualitatively, the smaller charge transfer is due to the fact that the Mo atoms in Mo_3O_6 are already reduced (+4) and it is more difficult for the cluster to accommodate additional electrons from the Cu(111) surface.

By similar arguments, we would also expect the W_3O_6/Cu(111) surface to have a smaller charge transfer and work function shift than its more oxidized counterpart. Indeed, the experimentally observed surface dipole moment and calculated work function shift for W_3O_6/Cu(111) are significantly smaller and in the same direction as that for the W_3O_9/Cu(111). A careful look at Table 6.1, however, shows that work function shift is mainly due to the electrostatic potential from W_3O_6, rather than from the charge transfer potential as seen in the other systems. The relatively large cluster contribution to the work function shift can be traced to the DFT optimized geometry of the W_3O_6 cluster on the Cu(111) surface (Figure 6.2(e)), where the W_3O_6 structure is not symmetric anymore and the oxygen atoms are seen to bend away from the surface. This surface bonding is quite different from that of the W_3O_9 cluster, which makes three O-Cu bonds (Figure 6.2b), or any of the other clusters studied here. Bader charge analysis result shows a small charge transfer (0.28e) from W_3O_6 to Cu(111), even though the potential difference along surface normal is almost zero. These results suggest that the reduced W_3O_6 cluster cannot accommodate more electrons from Cu(111). Note that this behavior would not be predicted from the electron affinity alone since the electro affinity of W_3O_6 is similar to that of Mo_3O_6[125].

Similar analysis were also conducted on Ti_3O_6/Cu(111) and Ti_5O_{10}/Cu(111). However, the direction of calculated work function shift is opposite of our experimental observation. The theoretical results show that the work function decreases as a result of Ti_xO_y cluster deposition. Such discrepancy can be accounted for by different reasons: i) the structures of Ti_xO_y/Cu(111) from DFT calculations are different from those in the experiments. It could be because the optimized structures are only the local minimum and more efforts need to be devoted to searching the most stable configurations of Ti_xO_y clusters on Cu(111). It could also be because that the structures of Ti_xO_y clusters change significantly upon deposition during experiments, e.g. new structures are formed as a result of cluster agglomeration. ii) The employed DFT+U method cannot describe the electronic structures of Ti_xO_y/Cu(111) correctly. A closer look at the calculated Density of State (DOS) structure is necessary to make sure the employed U value is appropriate. The calculation is still under the way. As mentioned above, an increase in the overall surface dipole for the Ti_5O_{10}/Cu(111) surface compared to the Ti_3O_6/Cu(111) surface ($\mu = -0.48$ D) is observed experimentally. Our Bader charge analysis also show the an increase in charge transfer from the Cu(111) surface to Ti_5O_{10} than to Ti_3O_6, even though we understand we need to be careful about these results considering the incorrect direction of work function shift that DFT calculations predict. However, these results agree with chemistry intuition because one would argue that the larger Ti_5O_{10} cluster can accommodate more charge due to the larger number of Ti^{4+} cations. This trend is also consistent the greater electron affinity of Ti_5O_{10} (4.13 eV) than that of Ti_3O_6 (3.15 eV)[137]. Chances are that a larger charge transfer from Cu(111) to Ti_5O_{10} contributes to the experimentally observed larger dipole moment on Ti_5O_{10}/Cu(111) than that on Ti_3O_6/Cu(111).

6.4. Conclusions

In this work, experiments and DFT calculations were combined to investigate the electronic interactions at the interface of size-selected metal oxide clusters (Mo_3O_9, W_3O_9, Ti_3O_6, Mo_3O_6, W_3O_6 and Ti_5O_{10}) on a Cu(111) surface. The Cu-cluster interactions were probed by 2PPE measurements which allowed us to obtain local work function data over a large range of cluster coverage. For all the clusters included in this study, the work function shifts to higher value as a result of interactions with the Cu(111) surface. An increasing work function with cluster coverage is consistent with a resultant surface dipole moment pointing towards the surface (negative). To quantitatively compare the results between different clusters, the Topping model was used to derive the surface dipole moment (μ) resulting from cluster deposition. We assume the overall dipole moment can be resolved into two components, i.e, the dipole associated with the cluster itself and a dipole induced by the charge transfer between the cluster and the Cu(111) surface. Electrostatic potential energies along surface normal from DFT calculations were used to identify the origin of the observed surface dipole.

For the stoichiometric Mo_3O_9 and W_3O_9 clusters, the measured dipole moments are close to each other. The dominant origin of the measured work function shift and dipole moment is the charge transfer from Cu(111) to the clusters. The results agree well with the Bader charge analysis which gives the similar magnitude of charge transfer from Cu(111) to Mo_3O_9 and W_3O_9. These results are also consistent with the known gas-phase electron affinities for Mo_3O_9 and W_3O_9, which are comparable. As expected, the charge transfer from Cu(111) to the "reduced" Mo_3O_6 cluster is smaller than the stoichiometric Mo_3O_9 cluster which can accommodate more charge. In the case of the "reduced" W_3O_6 cluster, the electrostatic potential energies from DFT calculations predict the charge transfer between Cu(111) and W_3O_6 is almost zero and Bader charge analysis even shows a small charge transfer at a reverse direction compared with other cases, i.e, from cluster to Cu(111). The observed negative dipole moment is due to the intrinsic dipole moment of the W_3O_6 structure after deposition. The measured surface dipoles on both Ti_3O_6/Cu(111) and Ti_5O_{10}/Cu(111) are negative, but the magnitude is larger on Ti_5O_{10}/Cu(111). However, DFT calculations predict a positive dipole. More investigations are required to find the reason for such discrepancy. It is possible that the relatively greater charge transfer from Cu(111) to Ti_5O_{10} contributes to the observed larger dipole on Ti_5O_{10}/Cu(111) considering the bigger electron affinity of Ti_5O_{10} compared with Ti_3O_6. The larger Ti_5O_{10} cluster can accommodate more charge due to the greater number of Ti^{4+} cations. Overall, the results presented in this study show that a combination of detailed work function measurements and DFT calculations can be a powerful tool to investigate the electronic interactions at the metal oxide-metal interface.

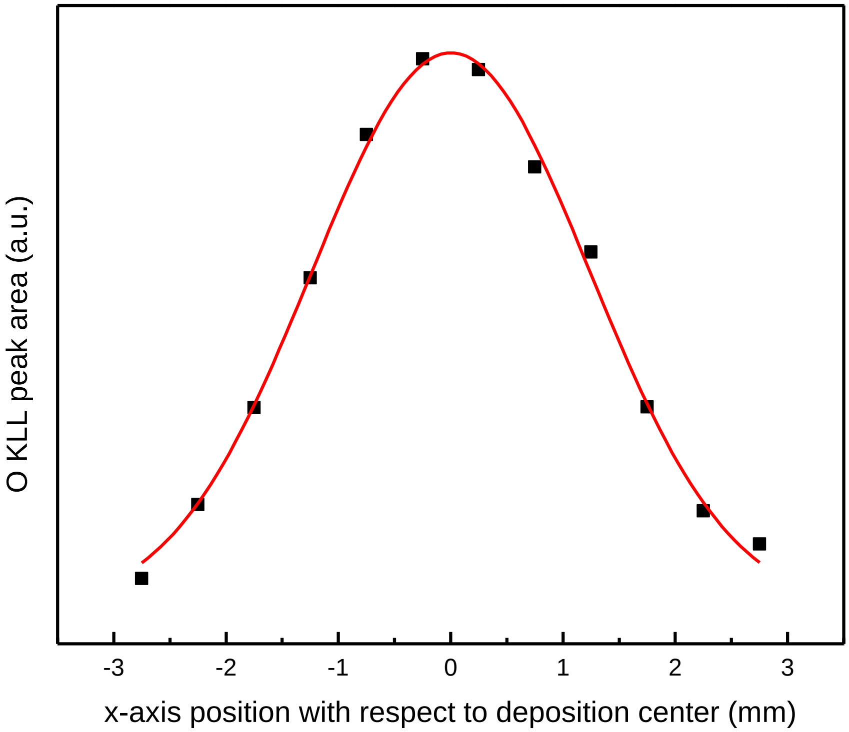

Figure 6.1. The O KLL peak area as a function of position on the surface along the horizontal direction. The solid line is a Gaussian fit to the data.

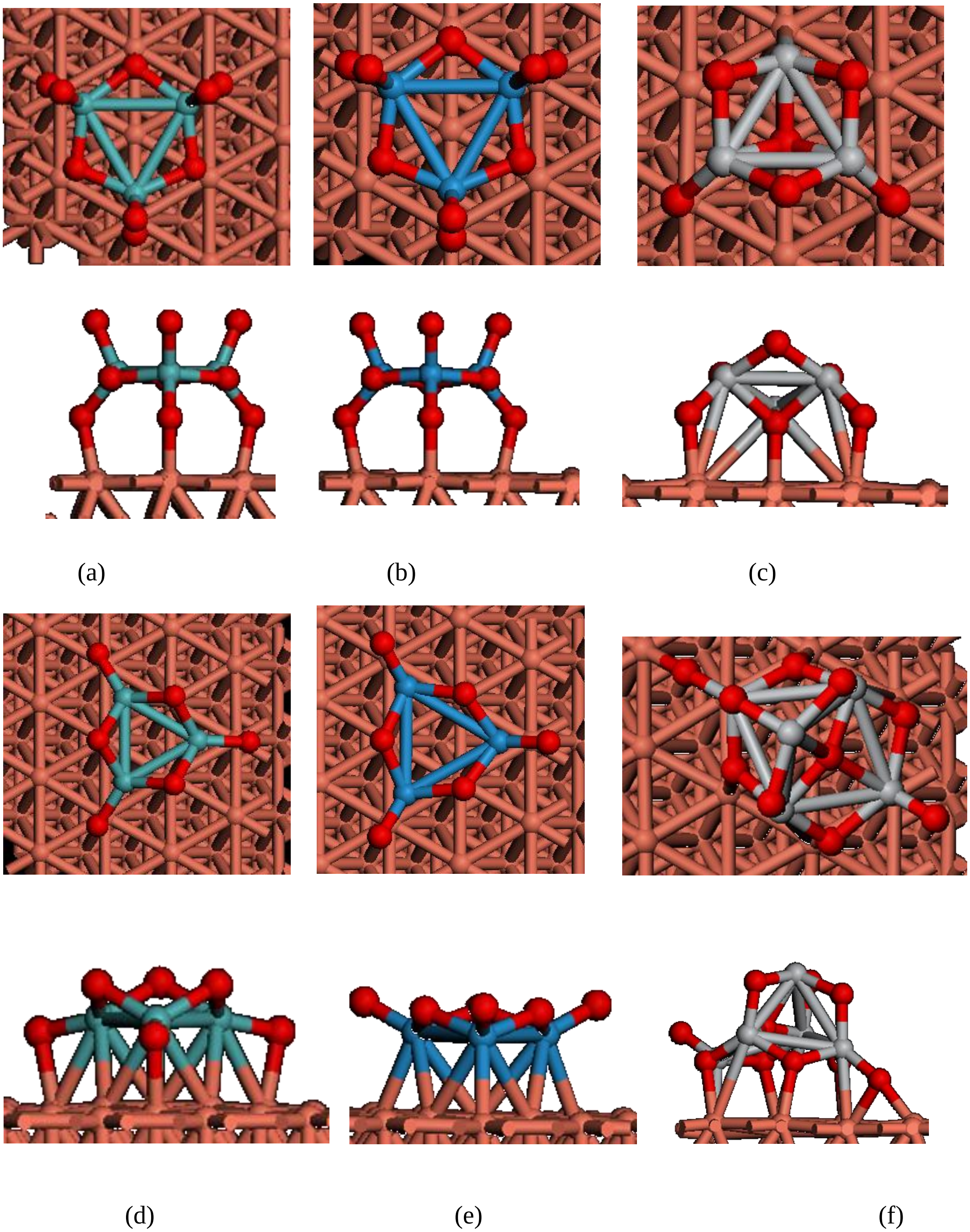

Figure 6.2. Top view and side view of the optimized geometry of clusters Mo_3O_9(a), W_3O_9(b), Ti_3O_6(c), Mo_3O_6(d), W_3O_6(e) and Ti_5O_{10}(f) on Cu(111). (Brown: Cu; green: Mo; blue:W; gray: Ti; red:O)

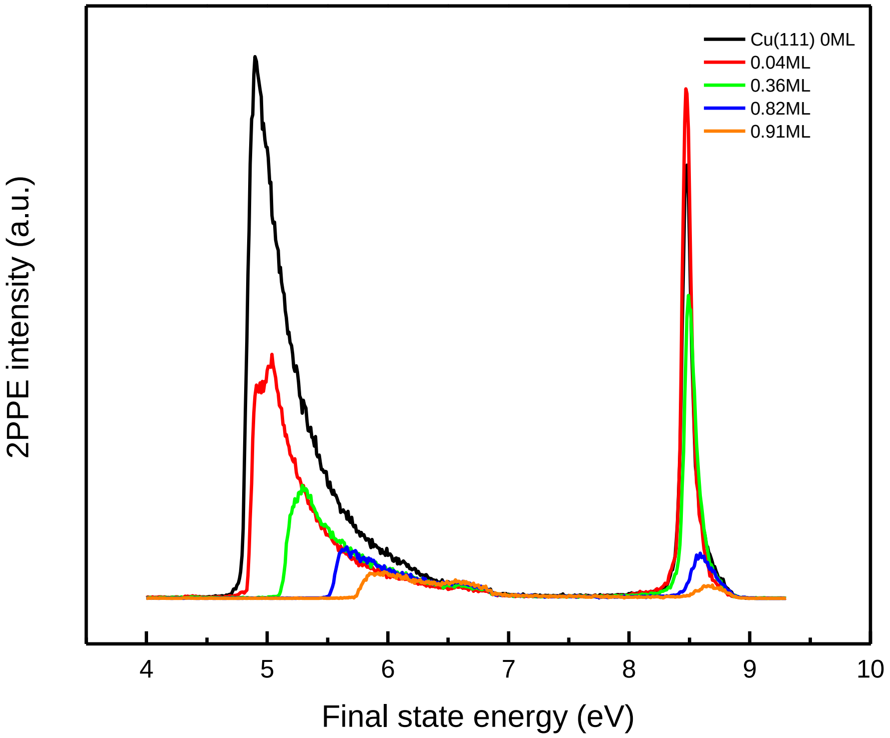

Figure 6.3. 2PPE spectra of Mo_3O_9/Cu(111) at different local coverage.

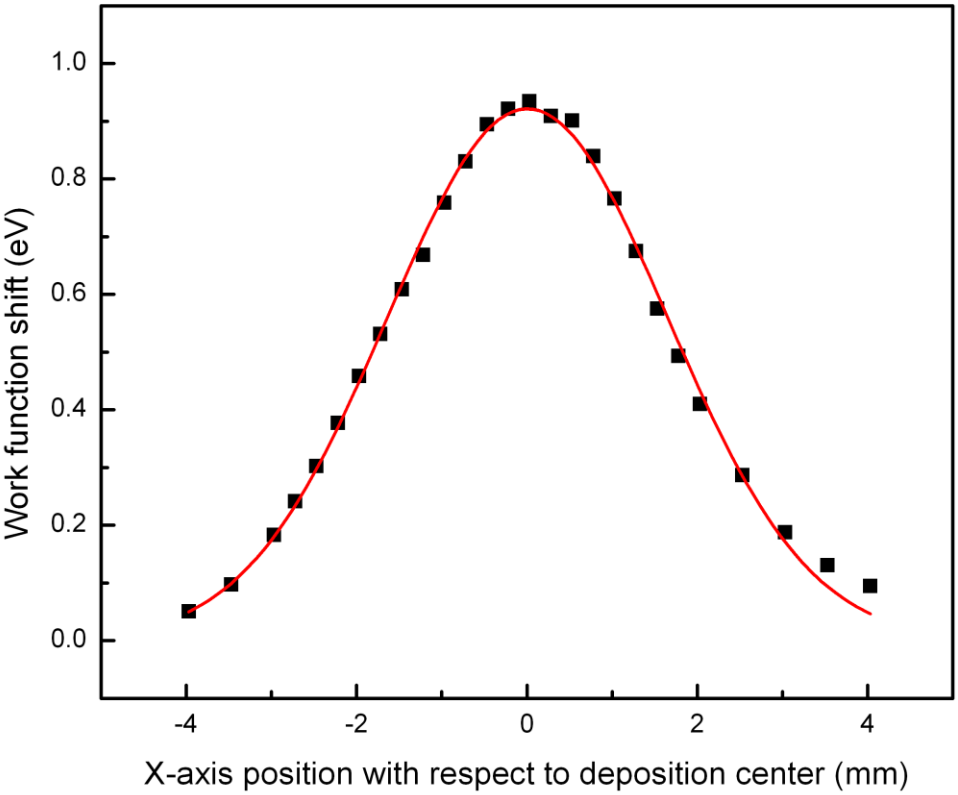

Figure 6.4. The work function shift on Mo_3O_9/Cu(111) as a function of position on the surface along the horizontal direction. The solid line is a Gaussian fit to the data.

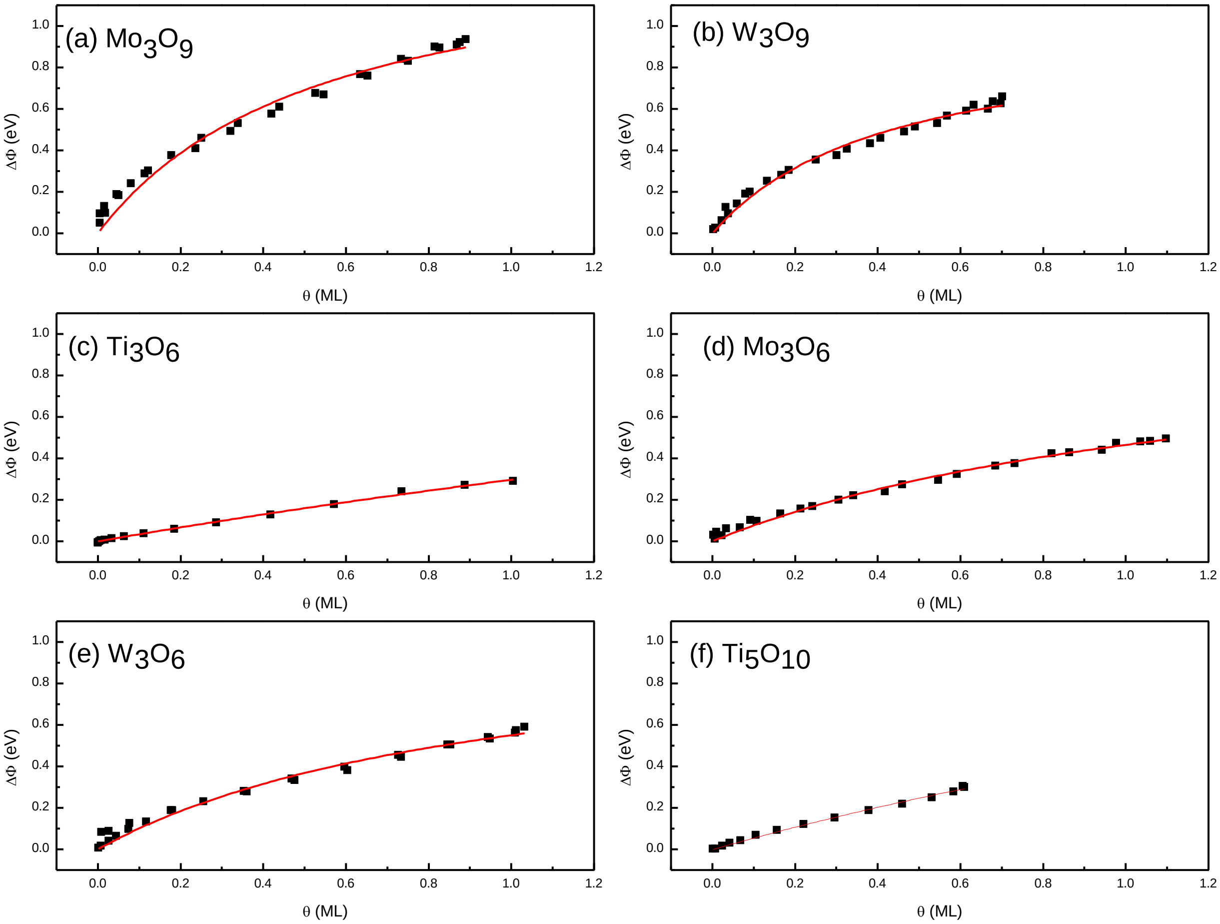

Figure 6.5. Work function shift with respect to local cluster coverage for Mo_3O_9(a), Mo_3O_9(a), W_3O_9(b), Ti_3O_6(c), Mo_3O_6(d), W_3O_6(e) and Ti_5O_{10}(f) on Cu(111). The solid lines are the fitting curves using Topping model.

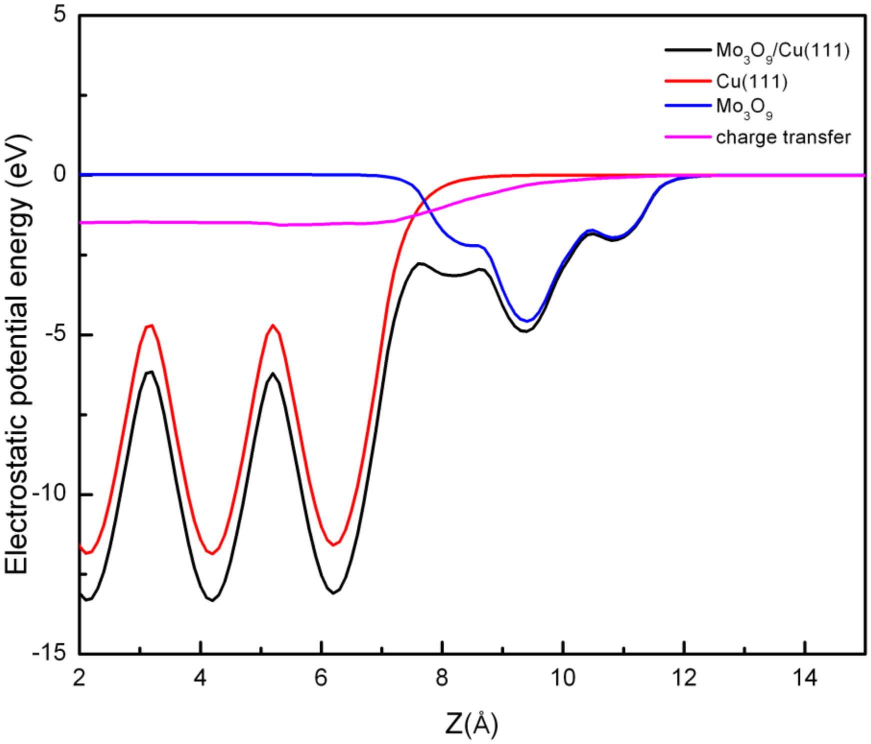

Figure 6.6. Electrostatic potential energy along surface normal for Mo_3O_9/Cu(111).

	Mo_3O_9	W_3O_9	Ti_3O_6	Mo_3O_6	W_3O_6	Ti_5O_{10}
radius (Å)	4.52	4.52	4.10	4.98	4.98	5.40/3.37
θ (ML)	0.45	0.45	0.35	0.55	0.55	0.40
μ(D)	-4.52	-3.96	-0.48	-1.71	-2.30	-0.87
ΔΦ(eV)	+1.46	+1.57	-0.51	+0.20	+0.51	-0.37
$\Delta V_{cluster}$ (eV)	-0.02	+0.09	N/A	-0.11	+0.50	N/A
ΔV_{charge} (eV)	+1.48	+1.48	N/A	+0.31	+0.01	N/A
Bader charge (e)	+1.40	+1.38	+0.33	+0.72	-0.28	+0.80
Electron affinity (eV)	4.0	4.2	3.15	2.90	2.95	4.13

Table 6.1. Properties of different clusters on Cu(111): calculated Radii and coverage θ; interfacial dipole moment (μ) derived from work function measurements using Topping model; calculated work function shift (ΔΦ); calculated electrostatic potential change along surface normal due to cluster ($\Delta V_{cluster}$) and charge transfer ($\Delta V_{cluster}$); charge on clusters after deposition on Cu(111) from bader charge analysis; electron affinity of gas-phase clusters from Ref. 137,138 and 139.

List of References

(1) Ma, J.; Sun, N.; Zhang, X.; Zhao, N.; Xiao, F.; Wei, W.; Sun, Y. *Catalysis Today* **2009**, *148*, 221.

(2) Liu, X. M.; Lu, G. Q.; Yan, Z. F.; Beltramini, J. *Industrial & Engineering Chemistry Research* **2003**, *42*, 6518.

(3) Song, C. *Catalysis Today* **2006**, *115*, 2.

(4) Olah, G. A.; Goeppert, A.; Prakash, G. K. S. *Beyond Oil and Gas: The Methanol Economy*; 2nd ed.; Wiley-VCH: Weinheim, 2009.

(5) Xu; Moulijn, J. A. *Energy & Fuels* **1996**, *10*, 305.

(6) Waugh, K. C. *Catalysis Today* **1992**, *15*, 51.

(7) Chinchen, G. C.; Denny, P. J.; Parker, D. G.; Spencer, M. S.; Whan, D. A. *Applied Catalysis* **1987**, *30*, 333.

(8) Yang, Y. X.; Evans, J.; Rodriguez, J. A.; White, M. G.; Liu, P. *Phys. Chem. Chem. Phys.* **2010**, *12*, 9909.

(9) Perdew, J. P.; Chevary, J. A.; Vosko, S. H.; Jackson, K. A.; Pederson, M. R.; Singh, D. J.; Fiolhais, C. *Physical Review B* **1992**, *46*, 6671.

(10) Dudarev, S. L.; Botton, G. A.; Savrasov, S. Y.; Humphreys, C. J.; Sutton, A. P. *Physical Review B* **1998**, *57*, 1505.

(11) Monkhorst, H. J.; Pack, J. D. *Physical Review B* **1976**, *13*, 5188.

(12) Haberland, H.; Karrais, M.; Mall, M.; Thurner, Y. *Journal of Vacuum Science & Technology A: Vacuum, Surfaces, and Films* **1992**, *10*, 3266.

(13) Haberland, H.; Mall, M.; Moseler, M.; Qiang, Y.; Reiners, T.; Thurner, Y. *Journal of Vacuum Science & Technology A: Vacuum, Surfaces, and Films* **1994**, *12*, 2925.

(14) Busolt, U.; Cottancin, E.; Röhr, H.; Socaciu, L.; Leisner, T.; Wöste, L. *Appl Phys B* **1999**, *68*, 453.

(15) Haberland, H.; Insepov, Z.; Moseler, M. *Physical Review B* **1995**, *51*, 11061.

(16) Vandoni, G.; Félix, C.; Goyhenex, C.; Monot, R.; Buttet, J.; Harbich, W. *Surface Science* **1995**, *331–333, Part A*, 838.

(17) Cheng, H.-P.; Landman, U. *The Journal of Physical Chemistry* **1994**, *98*, 3527.

(18) Rasmussen, P. B.; Holmblad, P. M.; Askgaard, T.; Ovesen, C. V.; Stoltze, P.; Nørskov, J. K.; Chorkendorff, I. *Catalysis Letters* **1994**, *26*, 373.

(19) Rasmussen, P. B.; Kazuta, M.; Chorkendorff, I. *Surface Science* **1994**, *318*, 267.

(20) Yoshihara, J.; Campbell, C. T. *Journal of Catalysis* **1996**, *161*, 776.

(21) Szanyi, J.; Goodman, D. W. *Catalysis Letters* **1991**, *10*, 383.

(22) Arena, F.; Italiano, G.; Barbera, K.; Bonura, G.; Spadaro, L.; Frusteri, F. *Basic evidences for methanol-synthesis catalyst design*; Elsevier Science Bv, 2009.

(23) Arena, F.; Barbera, K.; Italiano, G.; Bonura, G.; Spadaro, L.; Frusteri, F. *Journal of Catalysis* **2007**, *249*, 185.

(24) Kanai, Y.; Watanabe, T.; Fujitani, T.; Uchijima, T.; Nakamura, J. *Catalysis Letters* **1996**, *38*, 157.

(25) Yang, Y.; Mims, C. A.; Disselkamp, R. S.; Mei, D.; Kwak, J. H.; Szanyi, J.; Peden, C. H. F.; Campbell, C. T. *Catalysis Letters* **2008**, *125*, 201.

(26) Yoshihara, J.; Parker, S. C.; Schafer, A.; Campbell, C. T. *Catalysis Letters* **1995**, *31*, 313.

(27) Nakamura, I.; Fujitani, T.; Uchijima, T.; Nakamura, J. In *The 42nd national symposium of the American Vacuum Society*; 3 ed.; AVS: Mineapolis, Minnesota (USA), 1996; Vol. 14, p 1464.

(28) Fisher, I. A.; Bell, A. T. *Journal of Catalysis* **1997**, *172*, 222.

(29) Szanyi, J.; Goodman, D. W. *Catal. Lett.* **1991**, *10*, 383.

(30) Tang, Q.-L.; Hong, Q.-J.; Liu, Z.-P. *Journal of Catalysis* **2009**, *263*, 114.

(31) Hu, Z.-M.; Takahashi, K.; Nakatsuji, H. *Surface Science* **1999**, *442*, 90.

(32) Nakatsuji, H.; Hu, Z. *International Journal of Quantum Chemistry* **2000**, *77*, 341.

(33) Askgaard, T. S.; Norskov, J. K.; Ovesen, C. V.; Stoltze, P. *Journal of Catalysis* **1995**, *156*, 229.

(34) Grabow, L. C.; Mavrikakis, M. *ACS Catalysis* **2011**, *1*, 365.

(35) Zhao, Y.-F.; Yang, Y.; Mims, C.; Peden, C. H. F.; Li, J.; Mei, D. *Journal of Catalysis* **2011**, *281*, 199.

(36) Hiroshi Nakatsuji, Z.-M. H. *International Journal of Quantum Chemistry* **2000**, *77*, 341.

(37) Burch, R.; Golunski, S. E.; Spencer, M. S. *Catalysis Letters* **1990**, *5*, 55.

(38) Burch, R.; Golunski, S. E.; Spencer, M. S. *Catalysis Letters* **1990**, *5*, 55.

(39) Fujitani, T.; Nakamura, J. *Applied Catalysis A: General* **2000**, *191*, 111.

(40) Delley, B. *The Journal of Chemical Physics* **1990**, *92*, 508.

(41) Delley, B. *The Journal of Chemical Physics* **2000**, *113*, 7756.

(42) Halgren, T. A.; Lipscomb, W. N. *Chemical Physics Letters* **1977**, *49*, 225.

(43) Barrio, L.; Liu, P.; Rodriguez, J. A.; Campos-Martin, J. M.; Fierro, J. L. G. *The Journal of Chemical Physics* **2006**, *125*, 164715.

(44) Barrio, L.; Liu, P.; Rodriguez, J. A.; Campos-Martin, J. M.; Fierro, J. L. G. *Journal of Physical Chemistry C* **2007**, *111*, 19001.

(45) Liu, P.; Rodriguez, J. A. *The Journal of Chemical Physics* **2007**, *126*, 164705.

(46) Hammer, B.; Norskov, J. K. *Nature* **1995**, *376*, 238.

(47) Tang, Q.; Chen, Z.; He, X. *Surf. Sci.* **2009**, *603*, 2138.

(48) Schumacher, N.; Boisen, A.; Sahl, S.; Gokhale, A. A.; Kandoi, S.; Grabow, L. C.; Dumesic, J. A.; Mavrikakis, M.; Chorkendorff, I. *J. Catal.* **2005**, *229*, 265.

(49) Nakano, H.; Nakamura, I.; Fujitani, T.; Nakamura, J. *J. Phys. Chem. B* **2001**, *105*, 1355.

(50) Wang, G.; Morikawa, Y.; Matsumoto, T.; Nakamura, J. *J. Phys. Chem. B* **2006**, *110*, 9.

(51) Mei, D. H.; Xu, L.; Henkelman, G. *Journal of Catalysis* **2008**, *258*, 44.

(52) Gokhale, A. A.; Dumesic, J. A.; Mavrikakis, M. *Journal of the American Chemical Society* **2008**, *130*, 1402.

(53) Sakong, S.; Groß, A. *Surface Science* **2003**, *525*, 107.

(54) Pang, X. Y.; Xue, L. Q.; Wang, G. C. *Langmuir* **2007**, *23*, 4910.

(55) Hammer, B.; Scheffler, M.; Jacobsen, K. W.; Nørskov, J. K. *Physical Review Letters* **1994**, *73*, 1400.

(56) Greeley, J.; Mavrikakis, M. *Journal of Catalysis* **2002**, *208*, 291.

(57) Choi, Y.; Liu, P. *Journal of the American Chemical Society* **2009**, *131*, 13054.

(58) Choi, Y.; Liu, P. *Journal of the American Chemical Society* **2009**, *131*, 13054.

(59) Liu, P.; Rodriguez, J. A. *J. Phys. Chem. B* **2006**, *110*, 19418.

(60) Lynggaard, H.; Andreasen, A.; Stegelmann, C.; Stoltze, P. *Prog. Surf. Sci.* **2004**, *77*, 71.

(61) Fajín, J. L. C.; Cordeiro, M. N. D. S.; Illas, F.; Gomes, J. R. B. *Journal of Catalysis* **2009**, *268*, 131.

(62) Inderwildi, O. R.; Jenkins, S. J.; King, D. A. *Angew. Chem.-Int. Edit.* **2008**, *47*, 5253.

(63) Inderwildi, O. R.; Jenkins, S. J.; King, D. A. *Journal of Physical Chemistry C* **2008**, *112*, 1305.

(64) Remediakis, I. N.; Albild-Pederson, F.; Nørskov, J. K. *J. Phys. Chem. B* **2004**, *108*, 14535.

(65) Subramanian, N. D.; Balaji, G.; Kumar, C. S. S. R.; Spivey, J. J. *Catalysis Today* **2009**, *147*, 100.

(66) Schumacher, N.; Andersson, K.; Grabow, L. C.; Mavrikakis, M.; Nerlov, J.; Chorkendorff, I. *Surface Science* **2008**, *602*, 702.

(67) Schumacher, N.; Andersson, K. J.; Nerlov, J.; Chorkendorff, I. *Surface Science* **2008**, *602*, 2783.

(68) Nakatsuji, H.; Hu, Z.-M. *International Journal of Quantum Chemistry* **2000**, *77*, 341.

(69) Nerlov, J.; Chorkendorff, I. *Catalysis Letters* **1998**, *54*, 171.

(70) Nerlov, J.; Chorkendorff, I. *Journal of Catalysis* **1999**, *181*, 271.

(71) Nerlov, J.; Sckerl, S.; Wambach, J.; Chorkendorff, I. *Applied Catalysis A: General* **2000**, *191*, 97.

(72) Vesselli, E.; Rogatis, L. D.; Ding, X.; Baraldi, A.; Savio, L.; Vattuone, L.; Rocca, M.; Fornasiero, P.; Peressi, M.; Baldereschi, A.; Rosei, R.; Comelli, G. *Journal of the American Chemical Society* **2008**, *130*, 11417.

(73) Remediakis, I. N.; Abild-Pedersen, F.; NÃ¸rskov, J. K. *The Journal of Physical Chemistry B* **2004**, *108*, 14535.

(74) Christoffersen, E.; Stoltze, P.; Nørskov, J. K. *Surface Science* **2002**, *505*, 200.

(75) Gonzalez, S.; Illas, F. *Surface Science* **2005**, *598*, 144.

(76) Berlowitz, P. J.; Goodman, D. W. *Journal of Catalysis* **1987**, *108*, 364.

(77) Poutsma, M. L.; Elek, L. F.; Ibarbia, P. A.; Risch, A. P.; Rabo, J. A. *Journal of Catalysis* **1978**, *52*, 157.

(78) Ryndin, Y. A.; Hicks, R. F.; Bell, A. T.; Yermakov, Y. I. *Journal of Catalysis* **1981**, *70*, 287.

(79) Hicks, R. F.; Bell, A. T. *Journal of Catalysis* **1985**, *91*, 104.

(80) Fisher, I. A.; Bell, A. T. *Journal of Catalysis* **1996**, *162*, 54.

(81) Subramani, V.; Gangwal, S. K. *Energy & Fuels* **2008**, *22*, 814.

(82) Spivey, J. J.; Egbebi, A. *Chemical Society Reviews* **2007**, *36*, 1514.

(83) Zhao, Y.-H.; Sun, K.; Ma, X.; Liu, J.; Sun, D.; Su, H.-Y.; Li, W.-X. *Angew. Chem.-Int. Edit.* **2011**, *50*, 5335.

(84) Mei, D.; Rousseau, R.; Kathmann, S. M.; Glezakou, V.-A.; Engelhard, M. H.; Jiang, W.; Wang, C.; Gerber, M. A.; White, J. F.; Stevens, D. J. *Journal of Catalysis* **2010**, *271*, 325.

(85) Wambach, J.; Baiker, A.; Wokaun, A. *Phys. Chem. Chem. Phys.* **1999**, *1*, 5071.

(86) Kusama, H.; Bando, K. K.; Okabe, K.; Arakawa, H. *Applied Catalysis A: General* **2000**, *197*, 255.

(87) Kusama, H.; Okabe, K.; Sayama, K.; Arakawa, H. *Appl. Organomet. Chem.* **2000**, *14*, 836.

(88) Gotti, A.; Prins, R. *Catalysis Letters* **1996**, *37*, 143.

(89) Zhao, Y.-H.; Yang, M.-M.; Sun, D.; Su, H.-Y.; Sun, K.; Ma, X.; Bao, X.; Li, W.-X. *Journal of Physical Chemistry C* **2011**, *115*, 18247.

(90) González, S.; Sousa, C.; Illas, F. *The Journal of Physical Chemistry B* **2005**, *109*, 4654.

(91) Reuter, K. *Modeling Heterogeneous Catalytic Reactions: From the Molecular Process to the Technical System*; Wiley-VCH: Weinberg, 2009.

(92) Hammer, B.; Nørskov, J. K. In *Advances in Catalysis*; Bruce C. Gates, H. K., Ed.; Academic Press: 2000; Vol. Volume 45, p 71.

(93) Lukkien, J. J.; Segers, J. P. L.; Hilbers, P. A. J.; Gelten, R. J.; Jansen, A. P. J. *Physical Review E* **1998**, *58*, 2598.

(94) Liu, P.; Nørskov, J. K. *Phys.Chem. Chem. Phys.* **2001**, *3*, 3814.

(95) Chinchen, G. C.; Waugh, K. C.; Whan, D. A. *Applied Catalysis* **1986**, *25*, 101.

(96) Yang, Y.; Mims, C. A.; Disselkamp, R. S.; Kwak, J. H.; Peden, C. H. F.; Campbell, C. T. *Journal of Physical Chemistry C* **2010**, *114*, 17205.

(97) Yang, Y.; Mims, C.; Disselkamp, R.; Mei, D.; Kwak, J.-H.; Szanyi, J.; Peden, C.; Campbell, C. *Catalysis Letters* **2008**, *125*, 201.

(98) Yang, Y.; Mims, C.; Disselkamp, R.; Peden, C.; Campbell, C. *Topics in Catalysis* **2009**, *52*, 1440.

(99) Burch, R.; Chappell, R. J.; Golunski, S. E. *Journal of the Chemical Society, Faraday Transactions 1: Physical Chemistry in Condensed Phases* **1989**, *85*, 3569.

(100) Terumitsu, K. *Energy Conversion and Management* **1995**, *36*, 661.

(101) Kakumoto, T.; Watanabe, T. *Catalysis Today* **1997**, *36*, 39.

(102) Behrens, M.; Studt, F.; Kasatkin, I.; Kühl, S.; Hävecker, M.; Abild-Pedersen, F.; Zander, S.; Girgsdies, F.; Kurr, P.; Kniep, B.-L.; Tovar, M.; Fischer, R. W.; Nørskov, J. K.; Schlögl, R. *Science* **2012**.

(103) Hong, Q.-J.; Liu, Z.-P. *Surface Science* **2010**, *604*, 1869.

(104) Zhang, R. G.; Wang, B. J.; Liu, H. Y.; Ling, L. X. *Journal of Physical Chemistry C* **2011**, *115*, 19811.

(105) Rodriguez, J. A.; Graciani, J.; Evans, J.; Park, J. B.; Yang, F.; Stacchiola, D.; Senanayake, S. D.; Ma, S.; Pérez, M.; Liu, P.; Sanz, J. F.; Hrbek, J. *Angew. Chem.-Int. Edit.* **2009**, *48*, 8047.

(106) Vidal, A. B.; Liu, P. *Phys. Chem. Chem. Phys.* **2012**, *14*, 16626.

(107) Liu, P. *The Journal of Chemical Physics* **2010**, *133*, 204705.

(108) Kresse, G.; Hafner, J. *Physical Review B* **1993**, *47*, 558.

(109) Kresse, G.; Furthmüller, J. *Physical Review B* **1996**, *54*, 11169.

(110) Kresse, G.; Furthmüller, J. *Computational Materials Science* **1996**, *6*, 15.

(111) Kresse, G.; Joubert, D. *Physical Review B* **1999**, *59*, 1758.

(112) Blöchl, P. E. *Physical Review B* **1994**, *50*, 17953.

(113) Chrétien, S.; Metiu, H. *The Journal of Physical Chemistry C* **2011**, *115*, 4696.

(114) Nolan, M. *Chemical Communications* **2011**, *47*, 8617.

(115) Sanville, E.; BelBruno, J. J. *Physical Review B* **2007**, *76*, 085412.

(116) Liu, P.; Yang, Y.; White, M. G. *Surface Science Reports* **2013**, *68*, 233.

(117) Rodriguez, J. A.; Liu, P.; Hrbek, J.; Evans, J.; Pérez, M. *Angewandte Chemie International Edition* **2007**, *46*, 1329.

(118) Rodriguez, J. A.; Liu, P.; Wang, X.; Wen, W.; Hanson, J.; Hrbek, J.; Pérez, M.; Evans, J. *Catalysis Today* **2009**, *143*, 45.

(119) Sá, S.; Silva, H.; Brandão, L.; Sousa, J. M.; Mendes, A. *Applied Catalysis B: Environmental* **2010**, *99*, 43.

(120) Rodríguez, J. A.; Hrbek, J. *Surface Science* **2010**, *604*, 241.

(121) Zhou, J.; Zhou, J.; Camillone, N.; White, M. G. *Phys. Chem. Chem. Phys.* **2012**, *14*, 8105.

(122) Lightstone, J. M.; Patterson, M. J.; Liu, P.; Lofaro Jr, J. C.; White, M. G. *The Journal of Physical Chemistry C* **2008**, *112*, 11495.

(123) Zhou, J.; Yang, Y. X.; Liu, P.; Camillone, N.; White, M. G. *The Journal of Physical Chemistry C* **2010**, *114*, 13670.

(124) Topping, J. *Proceedings of the Royal Society of London. Series A* **1927**, *114*, 67.

(125) Rothgeb, D. W.; Mann, J. E.; Waller, S. E.; Jarrold, C. C. *The Journal of Chemical Physics* **2011**, *135*, 104312.

(126) Syzgantseva, O. A.; Gonzalez-Navarrete, P.; Calatayud, M.; Bromley, S.; Minot, C. *The Journal of Physical Chemistry C* **2011**, *115*, 15890.

(127) Henkelman, G.; Arnaldsson, A.; Jónsson, H. *Computational Materials Science* **2006**, *36*, 354.

(128) Bader, R. F. W.; Beddall, P. M. *The Journal of Chemical Physics* **1972**, *56*, 3320.

(129) Bondi, A. *The Journal of Physical Chemistry* **1964**, *68*, 441.

(130) Wang, H.; Dutton, G.; Zhu, X. Y. *The Journal of Physical Chemistry B* **2000**, *104*, 10332.

(131) Hertel, T.; Knoesel, E.; Hasselbrink, E.; Wolf, M.; Ertl, G. *Surface Science* **1994**, *317*, L1147.

(132) Pivetta, M.; Patthey, F.; Schneider, W. D.; Delley, B. *Physical Review B* **2002**, *65*, 045417.

(133) Rusu, P. C.; Brocks, G. *The Journal of Physical Chemistry B* **2006**, *110*, 22628.

(134) Rousseau, R.; De Renzi, V.; Mazzarello, R.; Marchetto, D.; Biagi, R.; Scandolo, S.; del Pennino, U. *The Journal of Physical Chemistry B* **2006**, *110*, 10862.

(135) Wang, Y.-G.; Yoon, Y.; Glezakou, V.-A.; Li, J.; Rousseau, R. *Journal of the American Chemical Society* **2013**, *135*, 10673.

(136) Huang, X.; Zhai, H.-J.; Kiran, B.; Wang, L.-S. *Angew. Chem.-Int. Edit.* **2005**, *44*, 7251.

(137) Zhai, H.-J.; Wang, L.-S. *Journal of the American Chemical Society* **2007**, *129*, 3022.